

MODELING OF PARTICLE MEDIA USING THE DISCRETE ELEMENT METHOD (DEM)

A Dissertation

by

TAM NGUYEN MINH DUONG

Submitted to the Office of Graduate and Professional Studies of  
Texas A&M University  
in partial fulfillment of the requirements for the degree of

DOCTOR OF PHILOSOPHY

Chair of Committee,	Zenon Medina-Cetina
Committee Members,	Ivan Damnjanovic
	Charles Aubeny
	Eduardo Gildin
Head of Department,	Robin Autenrieth

August 2019

Major Subject: Civil Engineering

Copyright 2019 Tam Duong

## ABSTRACT

Simulation of soil behaviors is always a challenge for engineers due to the non-homogeneous discontinuous nature of the materials. Unlike Finite Element Method (FEM) which follows the continuum approach, Discrete Element Method (DEM) was developed roughly 40 years ago attempted to model the nature behavior of particulate discontinuous media. Various studies have tried to simulate the mechanical soil behaviors under different controlled conditions by calibrating the DEM input micro-parameters. The calibration process plays essential role in reproducing the meso-mechanical response of granular materials subjected to laboratory tests. The goal of this study is to develop a methodology to calibrate the DEM input micro-parameters to accurately reproduce the meso-mechanical behaviors of granular materials subjected to controlled test conditions then apply to the in-situ conditions. This research consists of four studies. The first study investigates the effect of sample preparation conditions on material response using air pluviation method to prepare the sample. The DEM model is created to verify its ability to resemble the heterogeneity of the prepared granular sample via air pluviation. The second study presents a simple DEM model to replicate the triaxial compression test result for mono size steel spheres. The third study proposes a calibration process on model micro-parameters subjected to a compression test incorporating flexible membrane in the DEM model. The fourth study tries to apply DEM for solving large displacement problem like asteroid impact at Chicxulub.

To my dearest and beloved parents,  
Father and Mother, this is my gift to you.  
Thank you for everything you have done for me.  
I am grateful to be your daughter.  
I love you!

## ACKNOWLEDGEMENTS

My journey at Texas A&M would not be successful without the support, guidance and encouragement from my family, friends, professors and colleagues.

First of all, I would like to express my gratitude to my advisor, Dr. Zenon Medina-Cetina. Thank you for your dedication to my professional development. Thank you for your patient efforts in training me to become a better engineer/researcher as well as being understanding and supportive during my difficult times. Thank you for being an inspiration/role model for me. I have learned and grown up a lot during six years working under your guidance.

I would like to thank my committee members, Dr. Charles Aubeny, Dr. Ivan Damnjanovic and Dr. Eduardo Gildin for being a part of my committee and providing wise suggestions and feedbacks on my studies. I would like to thank my collaborators from Oregon State University, Dr. Matthew Evans and Dr. Ali Khoubani. Thank you for sharing your DEM code and providing me guidance and feedbacks on my DEM model.

I also want to acknowledge my former and current Stochastic Geomechanics Laboratory colleagues. Thank you for providing help and support for my research as well as sharing times together. Moreover, I want to thank the Civil Engineering department faculty and staff for making my time at Texas A&M University unforgettable.

Last but not least, I would like to thank my family for their endless love, encouragement and support throughout the journey regardless of long distances. Their love laid the foundation which makes me who I am today.

## CONTRIBUTORS AND FUNDING SOURCES

### **Contributors**

This work was supported by a dissertation committee consisting of Professor Zenon Medina-Cetina (advisor), Professor Charles Aubeny and Professor Ivan Damnjanovic of the Department of Civil Engineering and Professor Eduardo Gildin of the Department of Petroleum Engineering.

The DEM model with flexible boundary condition was provided by Professor Matthew Evans at Oregon State University and was published in 2005.

All other work conducted for the dissertation was completed by the student independently.

### **Funding Sources**

Graduate study was supported by a fellowship from Texas A&M University.

## TABLE OF CONTENTS

	Page
ABSTRACT.....	ii
DEDICATION .....	iii
ACKNOWLEDGEMENTS.....	iv
CONTRIBUTORS AND FUNDING SOURCES .....	v
TABLE OF CONTENTS.....	vi
LIST OF FIGURES .....	ix
LIST OF TABLES.....	xiv
CHAPTER I INTRODUCTION.....	1
1.1 Research purpose .....	1
1.2 Organization of the dissertation .....	2
CHAPTER II EXPERIMENTAL AND NUMERICAL ASSESSMENT OF SAMPLE HETEROGENEITY AND FAILURE MECHANISM OF SPECIMENS FORMED WITH GRANULAR MATERIALS .....	4
2.1 Background.....	4
2.2 Problem definition .....	5
2.3 Methodology.....	6
2.3.1 Material selection.....	6
2.3.2 Sample preparation .....	8
2.3.3 Triaxial compression test.....	10
2.3.4 DEM model.....	12
2.3.5 Void ratio analysis .....	14
2.4 Results .....	16
2.4.1 Specimen void ratio .....	16
2.4.2 Undrained shear strength .....	18
2.4.3 Comparison between numerical and experimental results.....	18
2.4.4 Computational effort.....	19
2.5 Discussion.....	19

CHAPTER III	2D DEM MODELING OF TRIAXIAL COMPRESSION WITH FLEXIBLE	
	MEMBRANE USING UNIFORM PARTICLE SIZE .....	28
3.1	Background.....	28
3.2	Experimental triaxial compression test.....	28
3.3	DEM model.....	29
3.3.1	Background on triaxial modeling in PFC .....	29
3.3.2	Calculation cycle-Quasi-static condition-Inertia number-Critical time step & Model scaling.....	30
3.3.3	Boundary condition.....	30
3.3.4	Contact model .....	31
3.3.5	Parametric study.....	32
3.4	Numerical result.....	33
3.5	Discussion.....	33
CHAPTER IV	CALIBRATION OF GRANULAR MATERIALS UNDER TRIAXIAL	
	COMPRESSION USING DEM .....	37
4.1	Background.....	37
4.2	Problem definition .....	39
4.3	Methodology.....	39
4.4	Experimental data .....	40
4.5	DEM model.....	41
4.5.1	DEM model of triaxial compression test .....	41
4.5.2	Model scaling.....	42
4.5.3	Contact model .....	43
4.5.4	Flexible boundary .....	43
4.5.5	Parameter study.....	44
4.6	Preliminary result.....	45
4.6.1	First simulation .....	45
4.6.2	Contact stiffness.....	45
4.6.3	Normal to shear stiffness ratio .....	46
4.6.4	Friction coefficient.....	47
4.6.5	Rolling resistance friction coefficient.....	47
4.6.6	Validation with experimental response.....	48
4.7	Discussion.....	50
CHAPTER V	PARAMETRIC STUDY OF THE ASTEROID IMPACT AT CHICXULUB:	
	INTEGRATING GEOLOGICAL FIELD OBSERVATIONS AND DEM	
	MODELING .....	51

5.1 Introduction.....	51
5.2 Background on the Chicxulub crater .....	52
5.3 Problem definition .....	56
5.4 Methodology.....	59
5.5 DEM model of asteroid impact.....	61
5.5.1 Contact model .....	61
5.5.2 Boundary condition.....	62
5.5.3 Measurement spheres.....	62
5.6 Simulation results.....	65
5.6.1 Final crater and surface topography.....	66
5.6.2 Velocity fields .....	67
5.6.3 Horizontal and vertical stresses .....	67
5.6.4 Contact force chains.....	68
5.7 Discussion.....	68
CHAPTER VI CONCLUSIONS AND FUTURE WORKS.....	93
6.1 Conclusions.....	93
6.2 Future works .....	94
REFERENCES .....	95

## LIST OF FIGURES

	Page
Figure 1. Chrome steel spheres: 6 mm diameter (left) and 3 mm diameter (right). .....	7
Figure 2. Sample preparation equipment setup.....	9
Figure 3. Experimental design for sample preparation conditions. ....	10
Figure 4. Prepared sample subjected to 55 kPa vacuum pressure. ....	10
Figure 5. Prepared Specimen Subjected to Triaxial Compression. ....	11
Figure 6. DEM Sample Generated by Air Pluviation Method.....	13
Figure 7. Sample preparation using radius expansion method in PFC3D. ....	14
Figure 8. Cross section radius (r) of a sphere. ....	15
Figure 9. Example cross section area of a sample. ....	15
Figure 10. Box plot void ratio of 6mm diameter sphere samples. ....	17
Figure 11. Box plot void ratio of 3mm diameter sphere samples.....	17
Figure 12. Stress-strain curves of random 6mm diameter sphere samples subjected to triaxial compression. ....	21
Figure 13. Stress-strain curve of random 3mm diameter sphere samples subjected to triaxial compression. ....	22
Figure 14. Ultimate stress of 6mm diameter sphere sample versus void ratio. ....	23
Figure 15. Ultimate stress of 3mm diameter sphere sample versus void ratio. ....	23
Figure 16. Comparison of void ratio variation of samples prepared from 0.305m drop height using air pluviation method and radius expansion method.....	24
Figure 17. Comparison of void ratio variation of samples prepared from 0.610m drop height using air pluviation method and radius expansion method.....	25
Figure 18. Comparison of void ratio variation of samples prepared from 0.915m drop height using air pluviation method and radius expansion method.....	26

Figure 19. Void ratio of experimental samples and numerical samples (left) and percentage error (right).....	27
Figure 20. Stress-strain responses of 3 mm and 6 mm diameter samples at the same preparation condition. ....	29
Figure 21. Model response to varying modulus of elasticity.....	34
Figure 22. Model response to varying friction coefficient. ....	34
Figure 23. DEM model versus experimental response for 3 mm particles.....	35
Figure 24. DEM model versus experimental response for 6 mm particles.....	35
Figure 25. Sample deformation (a), velocity field (b), and accumulative contact force map (c) obtained from DEM simulation for 3 mm particles.....	36
Figure 26. Sample deformation (a), velocity field (b), and accumulative contact force map (c) obtained from DEM simulation for 6 mm particles.....	36
Figure 27. Schematic procedure of the probabilistic calibration process. ....	40
Figure 28. The triaxial system and the selected stress-strain response. Reprint from [57]. ....	41
Figure 29. DEM model of consolidated sand specimen with flexible membrane.....	42
Figure 30. Initial model response comparing to the experimental data.....	45
Figure 31. Model responses to varying parameter $\theta_1$ .....	46
Figure 32. Model responses to varying parameter $\theta_2$ .....	47
Figure 33. Model responses to varying parameter $\theta_3$ .....	48
Figure 34. Model responses to varying parameter $\theta_4$ .....	49
Figure 35. Model responses after calibration process.....	49
Figure 36. Sample deformation (a), velocity field (b), and accumulative contact force map (c) obtained from DEM simulation. ....	50
Figure 37. Schematic drawing of the Chicxulub crater. Reprint from [61].....	53
Figure 38. Complex crater formation process. Reprint from [62]. ....	54
Figure 39. Locations of geophysical and drilling explorations performed at the site. Reprint.....	54

Figure 40. Lithostratigraphic correlation of boreholes from previous drilling programs. Reprint from [61].	55
Figure 41. Schematic of Chicxulub crater with corresponding drilling locations. Reprint	55
Figure 42. Numerical simulation of Chicxulub impact at different time instants with recorded of induced peak-shock pressure. Reprint from [81].	57
Figure 43. Final crater configuration for impact angle of 60 and 30 with impactor initial position on the top right. Reprint from [76].	58
Figure 44. Surface topography produced by 3D iSALE hydrocode for impact direction from right to left. Reprint from [76].	59
Figure 45. Schematic graph of the model experimental design.	60
Figure 46. Asteroid impact model configuration.	63
Figure 47. Components of linear parallel contact bond model. Reprint from [80].	64
Figure 48. Verification of infinite boundary condition.	65
Figure 49. Measurement spheres locations.	65
Figure 50. Final craters corresponding to different asteroid velocity with 90 <sup>0</sup> impact angle.	70
Figure 51. Final craters corresponding to different asteroid velocity with 60 <sup>0</sup> impact angle.	71
Figure 52. Final craters corresponding to different asteroid velocity with 45 <sup>0</sup> impact angle.	72
Figure 53. Final craters corresponding to different asteroid velocity with 30 <sup>0</sup> impact angle.	73
Figure 54. Crater topographies for 90 <sup>0</sup> impact angle.	74
Figure 55. Crater topographies for 60 <sup>0</sup> impact angle.	74
Figure 56. Crater topographies for 45 <sup>0</sup> impact angle.	74
Figure 57. Crater topographies for 30 <sup>0</sup> impact angle.	74
Figure 58. Velocity field variation right after impact at 90 <sup>0</sup> and asteroid velocity of 15 km/s. ...	75
Figure 59. Velocity field variation right after impact at 60 <sup>0</sup> and asteroid velocity of 15 km/s. ...	76
Figure 60. Velocity field variation right after impact at 45 <sup>0</sup> and asteroid velocity of 15 km/s. ...	77

Figure 61. Velocity field variation right after impact at $30^0$ and asteroid velocity of 15 km/s. ...	78
Figure 62. Velocity field variation right after impact at $90^0$ and asteroid velocity of 22.5 km/s.	79
Figure 63. Velocity field variation right after impact at $60^0$ and asteroid velocity of 22.5 km/s.	80
Figure 64. Velocity field variation right after impact at $45^0$ and asteroid velocity of 22.5 km/s.	81
Figure 65. Velocity field variation right after impact at $30^0$ and asteroid velocity of 22.5 km/s.	82
Figure 66. Vertical stress histories for asteroid impact of 15 km/s at $90^0$ .	83
Figure 67. Horizontal stress histories for asteroid impact of 15 km/s at $90^0$ .	83
Figure 68. Maximum vertical stresses for asteroid impacts at $90^0$ .	84
Figure 69. Maximum horizontal stresses for asteroid impacts at $90^0$ .	84
Figure 70. Maximum vertical stresses for asteroid impacts at $60^0$ .	85
Figure 71. Maximum horizontal stresses for asteroid impacts at $60^0$ .	85
Figure 72. Maximum vertical stresses for asteroid impacts at $45^0$ .	86
Figure 73. Maximum horizontal stresses for asteroid impacts at $45^0$ .	86
Figure 74. Maximum vertical stresses for asteroid impacts at $30^0$ .	87
Figure 75. Maximum horizontal stresses for asteroid impacts at $30^0$ .	87
Figure 76. Maximum vertical stresses for asteroid impacts at velocity of 15 km/s.	88
Figure 77. Maximum horizontal stresses for asteroid impacts at velocity of 15 km/s.	88
Figure 78. Maximum vertical stresses for asteroid impacts at velocity of 17.5 km/s.	89
Figure 79. Maximum horizontal stresses for asteroid impacts at velocity of 17.5 km/s.	89
Figure 80. Maximum vertical stresses for asteroid impacts at velocity of 20 km/s.	90
Figure 81. Maximum horizontal stresses for asteroid impacts at velocity of 20 km/s.	90
Figure 82. Maximum vertical stresses for asteroid impacts at velocity of 22.5 km/s.	91
Figure 83. Maximum horizontal stresses for asteroid impacts at velocity of 22.5 km/s.	91

Figure 84. Maps of contact force chains (linear contacts (a) and linear parallel bond contacts (b)) before and after asteroid impact of 15 km/s at  $90^{\circ}$ . ..... 92

## LIST OF TABLES

	Page
Table 1. Mechanical properties of considered materials. Reprinted from [21]. .....	7
Table 2. Ball input parameters in DEM model. ....	12
Table 3. Triaxial model parameters in PFC2D for steel spheres. ....	32
Table 4. Micro parameters as variables in Zhang’s probabilistic calibration. Reprint from [56].	39
Table 5. Model dimensions before and after scaling. ....	43
Table 6. Triaxial model parameters in PFC2D for sand. ....	44
Table 7. Micro parameters for sensitivity analysis of sand. ....	44
Table 8. Micro parameters of sand after calibration. ....	48
Table 9. Layer configuration and its particles dimension used in the impact model.....	63
Table 10. Contact model properties used in DEM impact simulations. ....	64

# CHAPTER I

## INTRODUCTION

### 1.1 Research purpose

The study on the behaviors of granular materials has always been an important topic in geotechnical engineering field, focusing on how the materials flow, deform and their corresponding failure mechanisms [1]. Accurately modelling the behaviors of granular materials will allow engineers to predict or assess possible landslides, slope stability, settlement of foundations on granular media, and so on. Proper risk assessment on geomaterial responses helps prevent and minimize tragic structural consequences but still remain cost-effective. Unlike the traditional finite-element method (FEM) used to predict behavior of geomaterials by discretizing the media into a mesh that the displacement and rotation of each component are dependent to each other, the discrete-element method (DEM) allows its components (disks, spheres, or clumps) to displace and rotate independently to each other [2]. DEM is promising to solve large deformation problems which require intensive computational effort using FEM. There have been numerous studies on geo-material behaviors using distinct element method (DEM) in Particle Flow Code (PFC3D) since the program was first established by Itasca in 1996. The results of the numerical simulations aim to provide an appropriate macroscopic mechanical behavior as comparison to the laboratory experiments in order to predict the failure mechanism of the materials. Zhu et al. presents a review in DEM theory developments over the past decades which focuses on particle models for the calculation of the particle–particle and particle–fluid interaction, coupling to describe particle–fluid flow, and available techniques for incorporating DEM to continuum modeling. A detailed list of DEM studies and applications is provided by Zhu et al. [3-4]. Zhu’s

paper categorizes DEM studies in to three areas, which are particle packing (cohesionless and cohesive particles), particle flow (confined and unconfined flow) and particle-fluid flow (cohesionless and cohesive particles). O’Sullivan’s review of the use of DEM in geomechanics presents a general overview for people whom are unfamiliar with using DEM in research practice including a brief summary of DEM evolution, types of particles, calculation algorithms, post-processing and general approach to validate and calibrate a DEM model [5]. According to O’Sullivan, DEM simulations of geo-materials include cohesionless soil, cemented sand, rock, and clay.

This research study orientates toward assessing the effect of micro properties to mechanical response of granular materials not only from sample preparation stage to shearing stage in laboratory tests but also in large deformation problems. This method would provide better understandings on micro parameter influence solely and in combination to the global behavior of the material subject to loading condition. Initially, a sensitivity analysis is perform to obtain the response closest to the laboratory test which those parameters serve as primary guess in the probabilistic calibration process. A probabilistic framework is followed to capture the variation of model parameter in space. It is interested to verify the ability of DEM program, PFC2D, in simulating large impact problem, i.e. asteroid impact to learn more about crater formation process for future event risk assessment.

## 1.2 Organization of the dissertation

This dissertation is prepared in journal article style. Each chapter contains material for one journal paper. Three studies on the use of DEM on solving particulate problems will be presented in

Chapter II to Chapter IV. Chapter II is the first study investigates the effect of sample preparation conditions on material response using air pluviation method to prepare the sample. The DEM model is created to verify its ability to resemble the heterogeneity of the prepared granular sample via air pluviation. Chapter III provides a simple DEM model for triaxial compression test with flexible boundary in PFC2D. Chapter IV presents the study proposing a probabilistic calibration process on model micro-parameters subjected to a triaxial test that incorporating flexible membrane in the DEM model. Chapter V is the study on applying DEM for solving large displacement problem like asteroid impact at Chicxulub. The geophysical information obtained from the crater site will be used as input parameters for the DEM model. Chapter VI provides overall discussion of three case studies and guideline for future research.

CHAPTER II  
EXPERIMENTAL AND NUMERICAL ASSESSMENT OF SAMPLE HETEROGENEITY  
AND FAILURE MECHANISM OF SPECIMENS FORMED WITH GRANULAR  
MATERIALS<sup>1</sup>

2.1 Background

Understanding the behavior of granular materials has drawn attention from various fields such as pharmaceutical manufacturing, geoscience, civil engineering, mining, and agriculture. Numerous studies have shown engineering behaviors of granular materials are significantly affected by sample preparation methods in the laboratories [6, 11, 13, 14, 16, 18, 20, 22, 25, 26, 27]. For example, Oda [13] and Arthur and Menzies [6] found that the stress-strain relationship of sand depends strongly on the sample preparation techniques. Researcher Ladd [11] observed that preparation methods significantly affect the cyclic shear strength of sand. Studies of Mulisli et al. [13] reported the effects of sample preparation techniques on the liquefaction characteristics of sand subjected to cyclic loadings. Additionally, Sadrekarimi and Olson [22] investigated the effect of a specimen preparation method on critical state behavior of sand. Moreover, Viad et al. [25] recommended water pluviation method over moist tamping method since samples prepared by the water pluviation method showed dilative behavior while samples prepared by the moist tamping method showed liquefaction behavior when subjected to triaxial compression and extension tests. Yamamuro et al. [27] pointed out that samples prepared by pluviated methods tend to have more stable grain-to-grain contacts, which resulted in a stable behavior compared to dry funnel

---

<sup>1</sup> Data reported in this chapter is reprinted with permission from “Experimental and Numerical Assessment of Sample Heterogeneity on Triaxial Failure Mechanism Using Chrome Steel Spherical Particles” by Tam N. Duong, 2015. Mater’s thesis. Texas A&M University. Copyright 2019 by Tam Duong.

deposition and slurry deposition methods. Lastly, a study conducted by Thomson and Wong [24] showed that both water pluviation and moist tamping methods resulted in non-homogenous samples noting that even though the void ratio of a water pluviated sample was lower only at the top quarter of the sample height, the void ratio of moist tamped sample varied along the sample height.

Based on previous studies [6, 11, 8,14, 16, 18, 20, 22, 25, 26, 27], there are a variety of factors that affect macroscopic behavior of granular materials within samples such as preparation methods, confining stress, sample density, grain size distribution, and material fabric. Common sample preparation techniques replicating in-situ conditions are moist tamping, dry funnel deposition, air pluviation and water pluviation [6, 11, 13, 14, 16, 18, 20, 22, 25, 26, 27]. Different sample preparation techniques can form samples with the same void ratio but dissimilar material fabrics, thus resulting potentially in different engineering behaviors [22]. This variation in sample heterogeneity can affect the engineering response of the sample. For instance, Morgenstern provided several geotechnical failures due to underestimating the effects of heterogeneity in soils. For example, the presence of clay seams in the site significantly reduced soil strength and its stability [12].

## 2.2 Problem definition

This study focuses on examining the behavior of granular samples constituted by the air pluviation method at differing heights and dispersion levels and subjected to triaxial compression conditions. In order to examine the variance in the granular samples' behaviors, the discrete element model of different sample preparation methods are generated and compared with the experimental sample

preparation results. The numerical modeling performed in this study provides additional evidences to support the hypothesis, as described in previous studies, of the influences sample preparation technique has the material behavior. The proposed hypothesis of this study is that samples composed of granular materials prepared following standard procedure of the air pluviation method, which are used to achieve a homogeneous structure, in fact prepare heterogeneous structures. By conducting a study verifying if the sample's preparation conditions affect the sample's mechanical response, important insight can be attained. Similar to the studies [6-17] the objective of this papers is to determine the impact of sample preparation on the heterogeneity granular material within samples; however this study will examine the ability of Particle-Flow-Code in three dimensions program (PFC3D) to accurately replicate the sample heterogeneity as obtained in sample preparation process which if capable of accurately replicating sample heterogeneity, could provide a reliable sample preparation alternative. The outcomes of this study's objectives will help to improve the understanding of the micro-mechanical behavior of granular materials with respect to meso- and macro-mechanical applications. Lastly, the DEM sample preparation simulation results generated in this study will be used in a later study to compare the difference in material response subjected to triaxial compression simulations.

## 2.3 Methodology

### 2.3.1 Material selection

As mention previously, the undrained behavior of granular materials are affected by grain size distribution, particle shape, surface friction, void ratio, and preparation methods [6, 11, 13, 14, 16, 18, 20, 22, 25, 26, 27]. To concentrate solely on the effect of the sample preparation method, other factors are minimized by choosing a material that has the same size, spherical shape, and low

friction coefficient. Several materials are taken into consideration: chrome steel, titanium, silicon nitride, and polycarbonate plastic. According to the manufacturer, Thomson Precision Balls, properties of those materials are listed in Table 1. [21]. Chrome steel is selected for this study due to the fact that the material is stiff with low friction coefficient and is cost-effective. Two particle sizes of 3 mm and 6 mm in diameter are used in the study to obtain the effect of particle size as well (Figure 1).

Table 1. Mechanical properties of considered materials. Reprinted from [21].

Properties	Material			
	Chrome Steel	Titanium	Silicon Nitride	Polycarbonate Plastic
Density (kg/m <sup>3</sup> )	7,833	4,510	3,190	1,200
Tensile strength (MPa)	2,240	434	830	62
Shear modulus (MPa)	80,000	44,000	130,000	786
Young's Modulus (MPa)	205,000	116,000	310,000	2,760
Friction coefficient	0.228	0.3	0.7	0.24

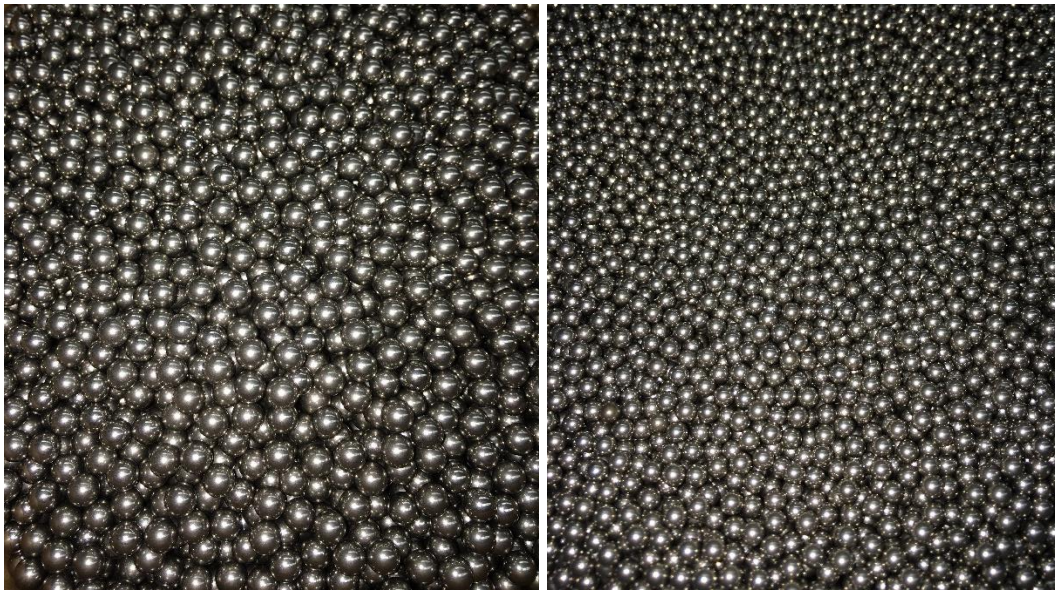


Figure 1. Chrome steel spheres: 6 mm diameter (left) and 3 mm diameter (right).

### 2.3.2 Sample preparation

It is hypothesized that the sample preparation could condition the failure mechanism of the granular samples in triaxial compression tests. The goal of the sample preparation technique is to constitute uniformly distributed cylindrical samples so the sample is closest to the homogenous state. Among listed methods, air pluviation is considered based on the previous study by Noble [17]. The air pluviation method reconstitutes samples by drizzling particles through a set of diffuser meshes placed on top of a fall tube into a mold. Pressure is applied on the mold using a vacuum pump to keep the membrane in contact with the mold. The tube has a similar diameter of the mold to obtain a uniform concentration of rain across the mold. Sieves are placed on top of the tube to adjust the dispersion level of particle flow. Steel spheres are poured into a plastic funnel whose bottom end is about 2.54 cm (1 inch) above the sieve to settle. A classic 1 inch diameter ball valve is installed at the bottom end of the funnel to control the flow. The funnel is support by a PVC frame. As the valve opens, spheres affected by only gravitational force fall out of the funnel, through the sieves, then through the acrylic tube, and into the triaxial mold. Figure 2 presents the experimental set-up of the air pluviation sample preparation method. The density of the samples can be increased by increasing the length of the fall tube or changing number of sieves placed on top of the tube. It is predicted that the sample will achieve a denser state as the spheres are dropped from higher distances due to higher potential energy of the spheres. Also, the density of samples prepared at the same drop height will decrease as the number of sieves placed on top of the tube increases because of energy loss due to contact with the sieves. The tube length varies from 30.48 cm (1 ft) to 91.44 cm (3 ft) with 30.48 cm increment. The number of sieve also changes from having no sieve to 3 sieves on the top of the tube. Five samples are made for each condition. Figure 3 shows the chart of variances of sample preparation conditions. Prepared sample of 3 mm

diameter spheres is showed in Figure 4. The dimensions of each sample (height and diameter) and the sample weight are recorded to obtain the global void ratio of the sample. Sample void ratio is calculated using the formula:

$$e = \frac{V_V}{V_S} = \frac{V_V}{V_T - V_V} \quad (1)$$

where  $e$  is void ratio;  $V_T$  is total sample volume with  $V_T = \pi H \frac{D^2}{4}$  where H and D are measured sample height and diameter;  $V_S$  is solid volume with  $V_S = \frac{W_s}{\rho}$  where  $W_s$  is sample weight and  $\rho$  is sphere density;  $V_V$  is volume of void.

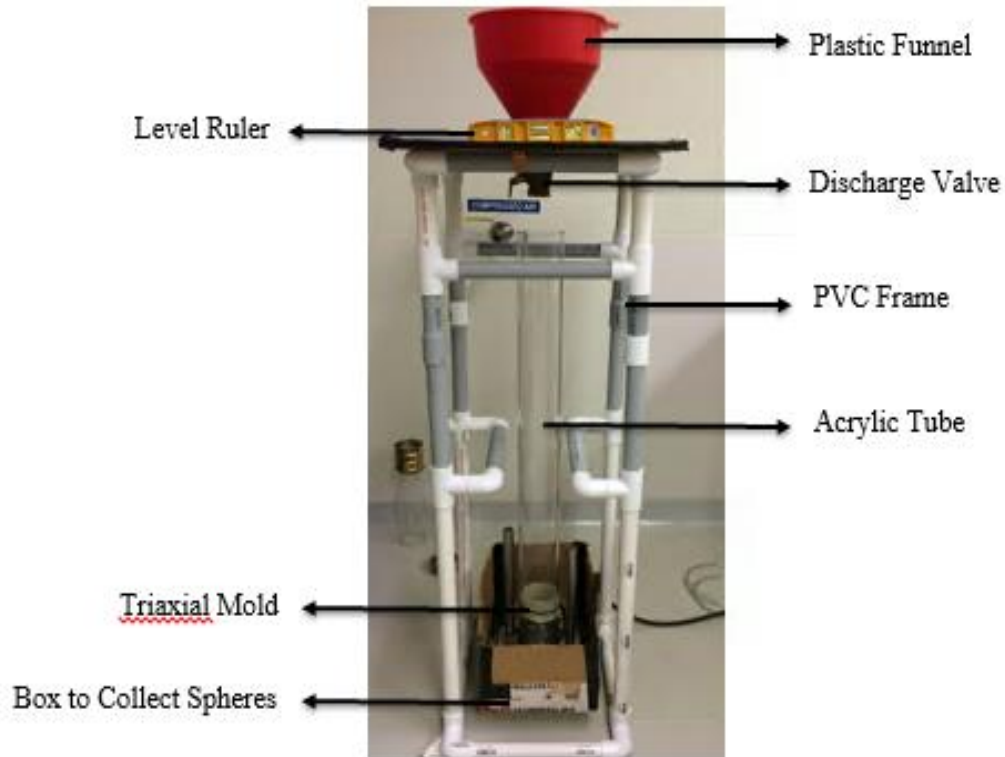


Figure 2. Sample preparation equipment setup.

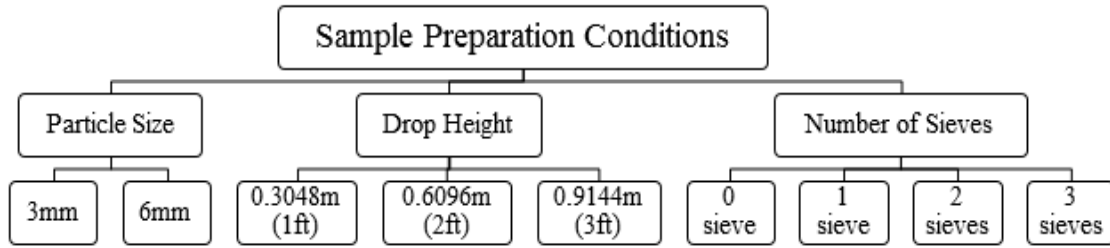


Figure 3. Experimental design for sample preparation conditions.



Figure 4. Prepared sample subjected to 55 kPa vacuum pressure.

### 2.3.3 Triaxial compression test

A triaxial compression test is performed based on samples made out of steel spheres, as a way to obtain shear strength parameters of particles measuring the axial stress and axial strain of the specimen [20]. ASTM standard procedure for the triaxial compression test is followed. The specimen is prepared as stated above and placed into the triaxial cell. A confining pressure of about 55 kPa has been applied to the specimen using vacuum pump since the specimen is prepared. A force transducer attached to a piston resting on the sample is used to capture the resistance of the

specimen during shearing. The cell is then placed in the loading frame that connected to a displacement transducer. Both transducers are connected to the computer through a data acquisition device. Figure 5 shows the triaxial test frame before compression. The test starts as the loading frame is raised up at a rate of 1.6 millimeter per minute, while the confining pressure is still applied to the specimen. In other words, the strain rate of the triaxial test is 1.6 millimeter per minute. The transducers transfer the recorded data to the computer and by the use of LabView program [21], which uses measured voltages from the transducers to get the displacement and force applied to the specimen. The end result provides adequate data to determine the strength and deformation properties of a sample composed of steel particles. One triaxial compression test is performed for each condition the sample is prepared.

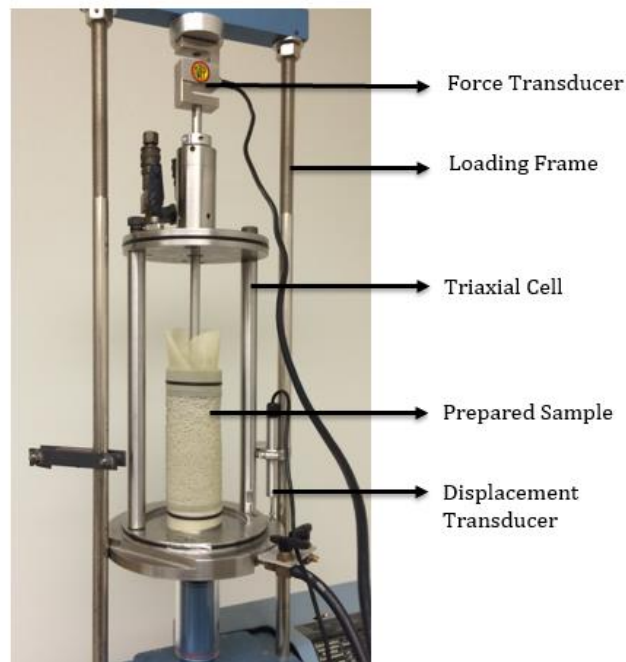


Figure 5. Prepared Specimen Subjected to Triaxial Compression.

### 2.3.4 DEM model

#### 2.3.4.a Sample preparation – Air pluviation method

A numerical model using DEM is constructed to replicate the whole experimental process from sample preparation and triaxial compression test. The goal is to achieve similar specimen densities for the same experimental sample preparation method as well as using such model from sample preparation to simulate compression test. This method for simulating compression test is different from ITASCA's proposed method in the manual where sample is prepared using radius expansion method to achieve desired sample porosity [22]. Generally, multiple walls are created and welded together to form the shape of a mold, a tube and a funnel. The sieve is replicated as meshes. A linear contact model is used in the air pluviation model. Macro-parameters for PFC-3D model are similar to material dimensions and material properties used in the experiment, including wall dimensions, ball diameter, ball density; friction coefficient of ball and ball, wall and ball. Micro-parameters for PFC-3D model, normal and shear stiffness of balls and of walls, are chosen based on previous studies [23-26]. Table 2 presents a list of parameters used in DEM model. Pictures of DEM model for air pluviation method are shown in Figure 6.

Table 2. Ball input parameters in DEM model.

DEM parameters	Unit	
Ball diameter	mm	3; 6
Ball density	kg/m <sup>3</sup>	7.8x10 <sup>3</sup>
Ball shear modulus	Pa	7.9x10 <sup>10</sup>
Ball-ball friction coefficient	-	0.096
Ball-wall friction coefficient	-	0.28
Ball normal stiffness	Pa	2.01x10 <sup>11</sup>
Ball shear stiffness	Pa	7.9x10 <sup>10</sup>



Figure 6. DEM Sample Generated by Air Pluviation Method.

#### 2.3.4.b Sample preparation – Radius expansion method

PFC support document supplied by Itasca provides a method to generate homogeneous specimen with specific non-zero material pressure [19]. This procedure includes a packing phase, which creates a grain assembly, and a finalization phase, which assigns contact properties and additional material properties that will be assigned to future contacts. At first, random particles are based on specified porosity. Then, the friction coefficient between particles is set to zero in order for the particles to rearrange until the mean stress nears zero or achieves a static-equilibrium condition. During this step, most of the overlaps are eliminated to prepare for the next step. Particle size is modified until the mean stress is within the pressure tolerance of the defined sample pressure and until the static-equilibrium condition has been achieved. In the finalized phase, final material properties are assigned to contacts, and additional material properties are specified for future material contacts shown in Figure 7. In this sample preparation procedure, the specimen pressure is set equal to the confining pressure of 55 kPa in the experiment, which is similar to the actual

triaxial test confining pressure. The initial porosity is equal to the global porosity value obtained from the sample preparation. The pressure tolerance ratio is set equal to 0.1.



Figure 8. Sample preparation using radius expansion method in PFC3D.

### 2.3.5 Void ratio analysis

With the purpose of this study being exploring the heterogeneity of the reconstituted samples, obtaining the spatial void ratio variation is a way to investigate the heterogeneity condition of the samples. The planar void ratio variation of the DEM model is obtained to determine if the model has capture the spatial heterogeneity of the sample. The end results provide a configuration of series of the mean planar void ratios along the sample height to compare with the global void ratio obtained from the experiment and with other methods. Centroid location of each ball is retrieved and imported into MATLAB to analyze the distance between the center of the each ball above the sample base, and a certain slice height is calculated if the ball is within its radius distance above and below the slice height (see Figure 8-9). Since the ball is perfectly spherical, the cross section of the ball is the same if the slice is above or below the ball centroid. The radius of the cross section of the ball is then calculated using the Pythagorean Theorem:

$$r = \sqrt{R^2 - z^2} \quad (2)$$

where  $r$  is the cross sectional radius,  $R$  is the radius of the ball, and  $z$  is the distance between the ball centroid location and the slice height.

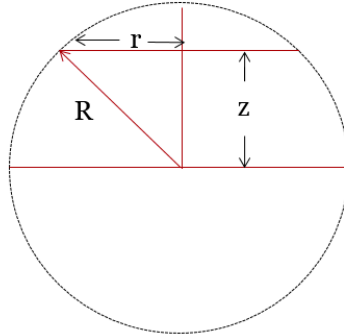


Figure 8. Cross section radius ( $r$ ) of a sphere.

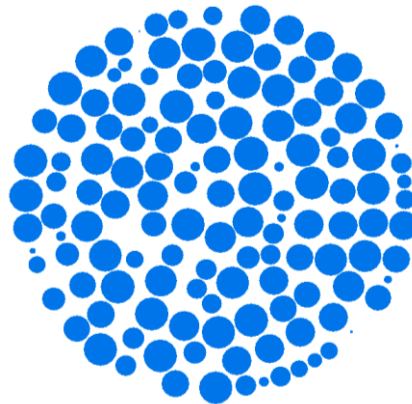


Figure 9. Example cross section area of a sample.

## 2.4 Results

### 2.4.1 Specimen void ratio

For each sample reconstituted, void ratio of the sample is calculated accordingly. Box plots of void ratio for each sample preparation condition are presented in Figure 10 and 11. The median (red line), the first and third quartiles (blue box), as well as the maximum and minimum void ratio (black skewers) for each sample preparation condition are illustrated by the box plots. In general, the sample void ratio tends to decrease as the drop height increases which means the sample is denser due to higher potential energy. The void ratio of the samples prepared at the same drop height increases as more sieves are placed which indicates the sphere's potential energy is reduced due to contact with the sieves leading to a lessened density state of the sample. Plots of the sample void ratio show the trend as predicted before.

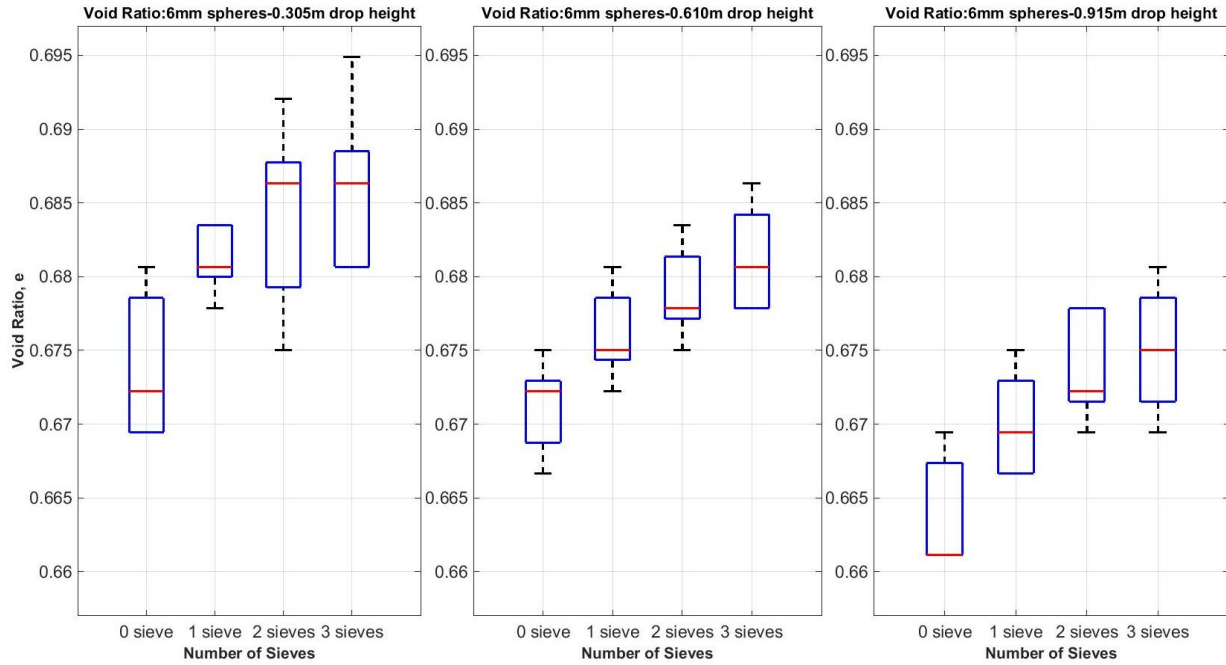


Figure 10. Box plot void ratio of 6mm diameter sphere samples.

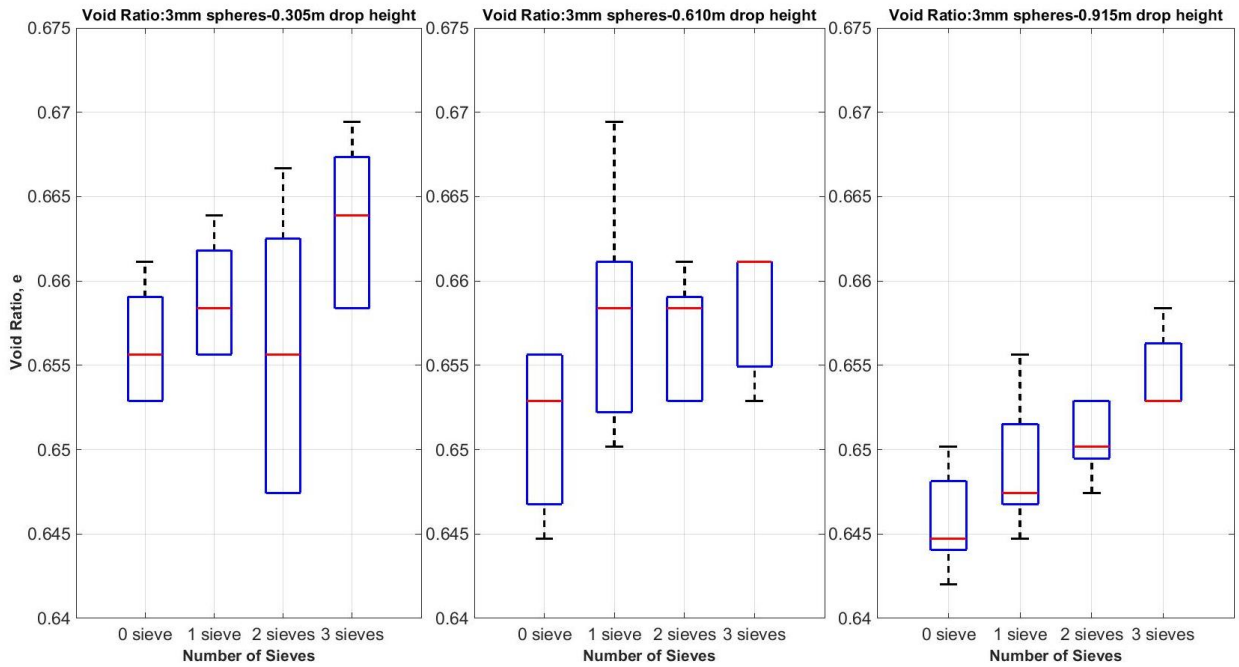


Figure 11. Box plot void ratio of 3mm diameter sphere samples

#### 2.4.2 Undrained shear strength

One sample for each condition-constituted samples is subjected to a triaxial compression test. Plots of deviatoric stress versus axial strain corresponding to sample void ratio for both sphere sizes are shown in Figure 12 and 13. The ultimate stress of each sample is recorded and plotted versus sample void ratio in Figure 14 and 15. It is observed that the stress strain curves indicates dense samples by having peak stresses. The ultimate stresses vary from 67 to 85 kPa for 6 mm diameter sphere samples and from 72 to 82 kPa for 3 mm diameter sphere samples. Despite the fact that the void ratios of samples made of 6 mm diameter spheres are higher than the void ratios of samples made of 3 mm diameter spheres, the variation of the ultimate stress is almost similar.

#### 2.4.3 Comparison between numerical and experimental results

Plots of the void ratio variation of PFC simulated samples using planar void ratio analysis method are presented below in Figure 16-18. The blue lines represent the planar void ratio variation and its corresponding mean of the samples prepared by the air pluviation method while the pink lines represent the planar void ratio variation and its corresponding mean of samples prepared by the radius expansion method in PFC. The green dotted line represents the global void ratio of the sample from experiment. The distribution of the void ratio greatly varies near the sample's base due to a tight packing of the balls at the base. Moving up the height of the sample, the variation of the void ratio deceases. At the top, the void ratio dramatically increases since there are fewer balls to fill the void. It is observed that the radius expansion method overestimated the sample void ratio while the air pluviation method underestimated the void ratio. However, the air pluviation method yields a smaller percentage error than the radius expansion method, shown in Figure 19. Therefore,

the DEM model using air pluviation method is expected to provide more accurate sample responses when simulating compression test.

#### 2.4.4 Computational effort

All of the PFC simulations are run in a Window server built on a super computer whose processor is the Intel Xeon E5-2695 v3 2.3 GHz chipset that has 14 cores and 28 threads. The installed memory (RAM) is 128 GB. PFC3D version 5.0 license allows running 2 instant simulations at the same time. The configuration of the Window server is recommended by ITASCA personnel for running complex PFC models. It is known that computational time is an important criteria to justify if the numerical models are efficient in replicating material behaviors. For sample formation in PFC, samples prepared by the radius expansion method take a couple hundred thousand cycles, approximately 1 hour, to complete while samples prepared by the air pluviation method take 30 million cycles, approximately 3 days, to complete. The difference is due to the fact that the air pluviation method simulates the actual physical stage of each sphere over time thus consuming more calculation cycles. The calculation time of the radius expansion method can be increased or decreased by changing the pressure tolerance.

#### 2.5 Discussion

In general, it is proven that the sample preparation method can affect material responses in this study. By changing the drop height and number of sieves, the sample void ratio changes accordingly during the sample preparation process. Void ratio changes also affect the material response when subjected to triaxial compression. Trend lines of the sample's ultimate stress versus the sample's void ratio are obtained to show their linear correlation. The ultimate stress increases

as the sample void ratio decreases or the sample becomes denser. Numerical models of the sample preparation process (air pluviation) are built and run on PFC3D to verify the replicability of experimental material response. This method of preparing a sample is also compared with the other method called radius expansion. A void ratio analysis of the two numerical models are performed to obtain the lateral void ratio variation along the sample height. It is showed that the numerical model of the air pluviation method provides the average void ratio closer to the experimental void ratio comparing to the void ratio of the sample prepared by radius expansion method. Due to the difference in the average sample void ratio, it is predicted that the numerical sample prepared by air pluviation method will produce a triaxial compression material response that is closer to the experimental result. One limitation experienced in this this study was the inability to obtain the experimental void ratio variation along the sample height for better comparison with the DEM results.

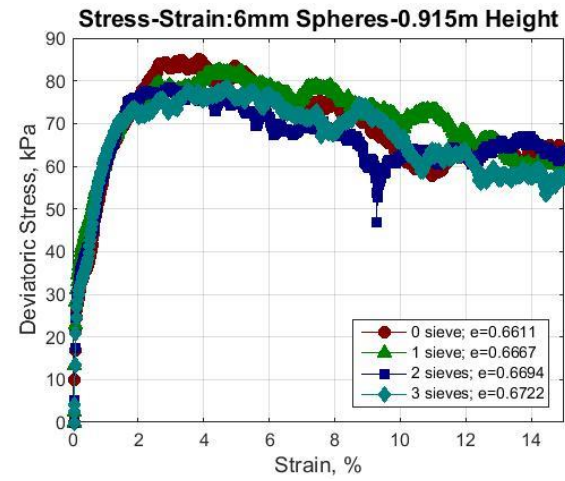
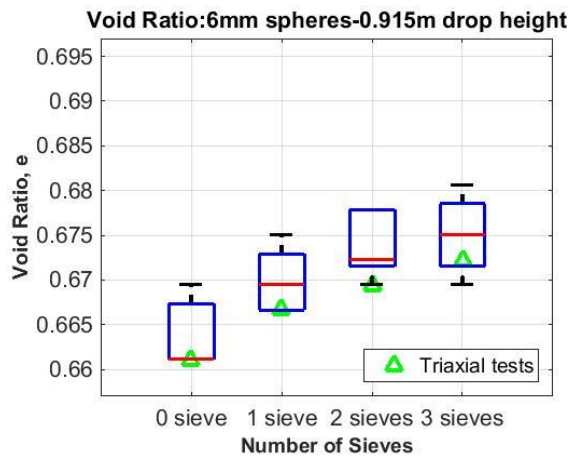
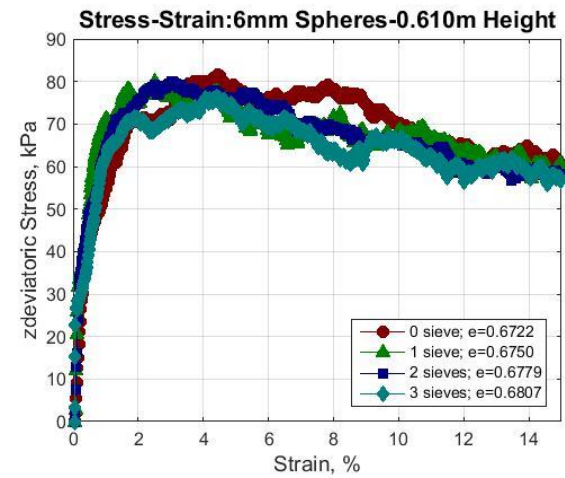
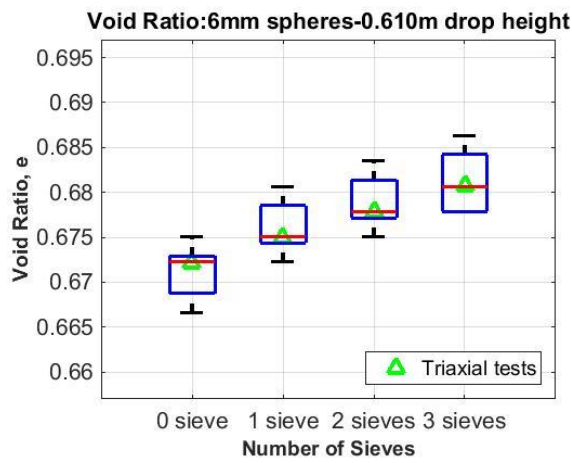
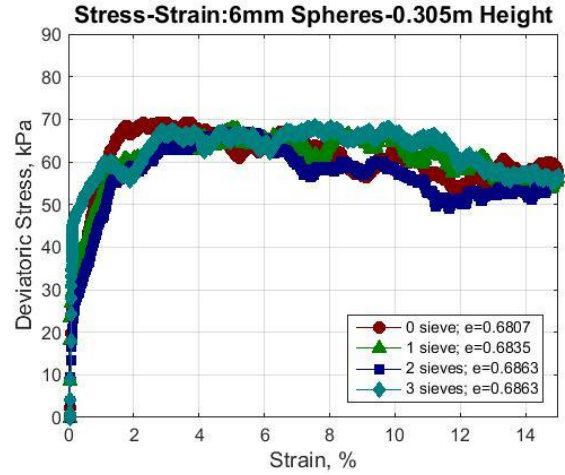
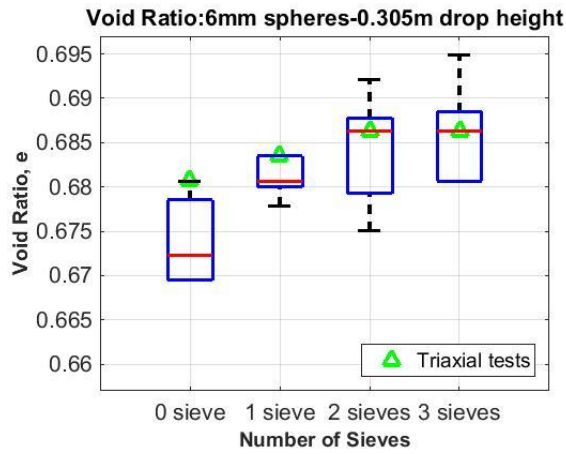


Figure 12. Stress-strain curves of random 6mm diameter sphere samples subjected to triaxial compression.

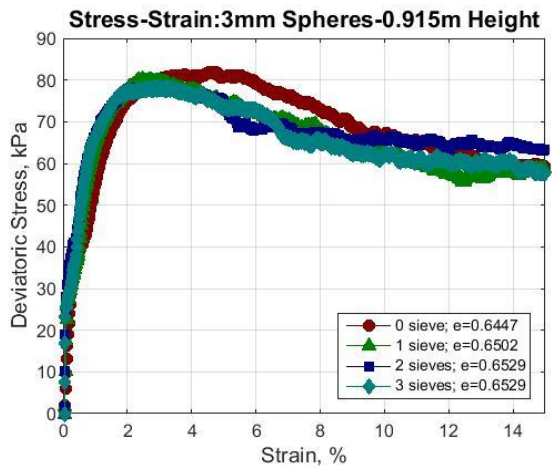
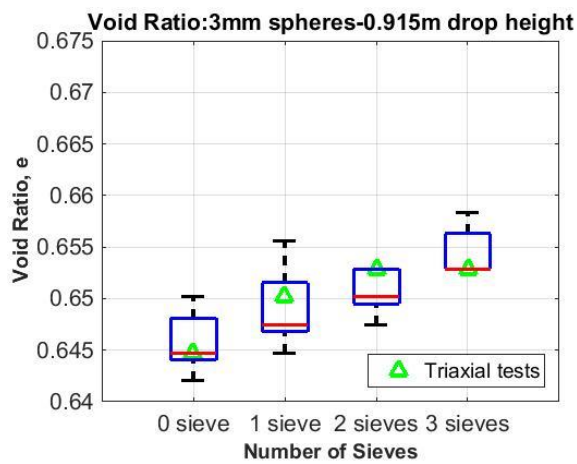
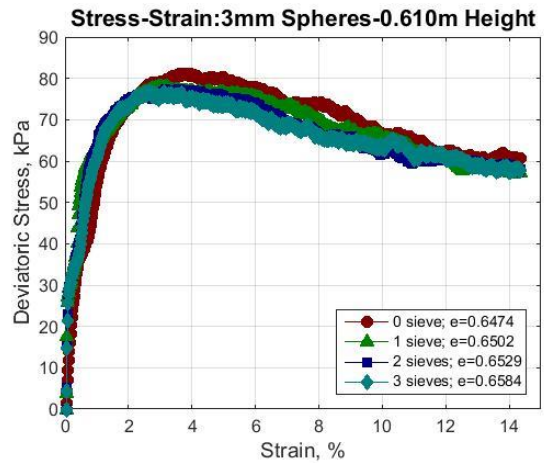
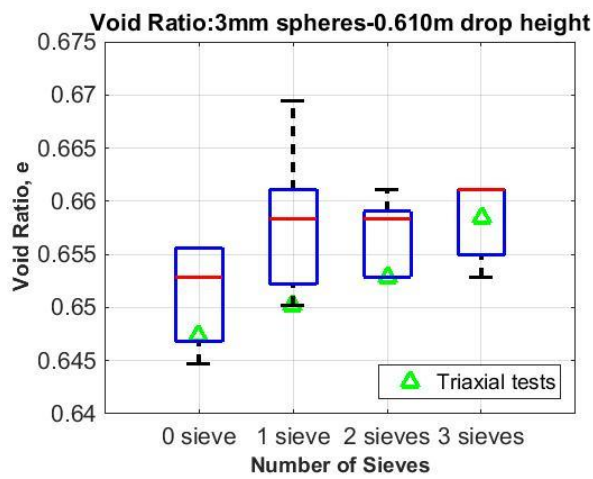
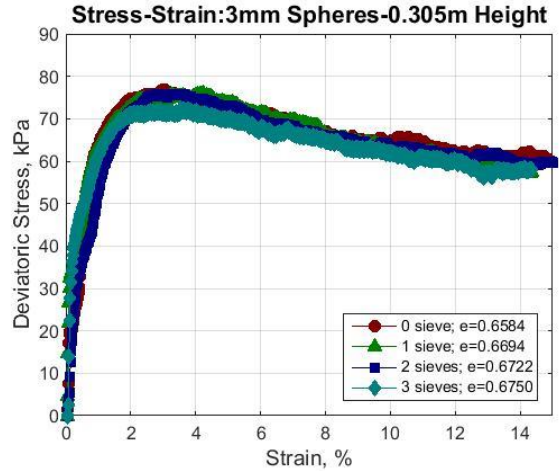
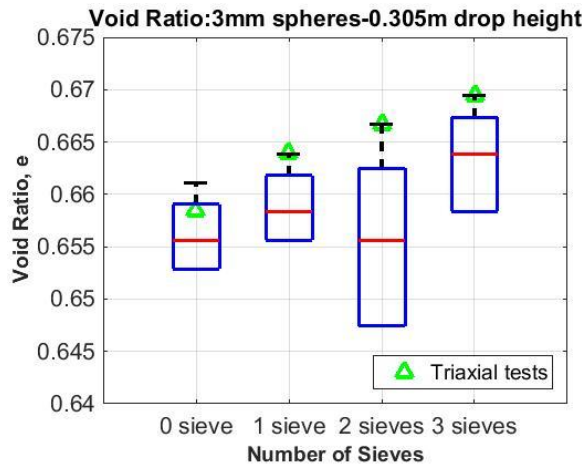


Figure 13. Stress-strain curve of random 3mm diameter sphere samples subjected to triaxial compression.

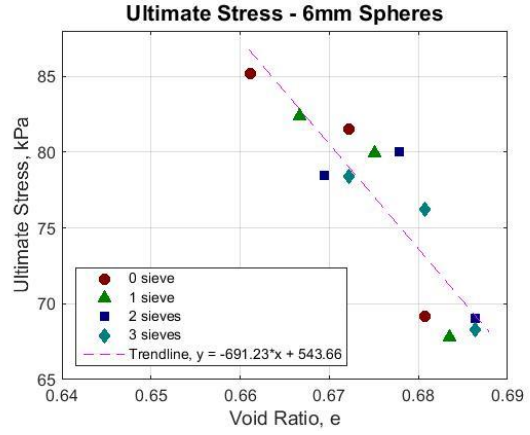
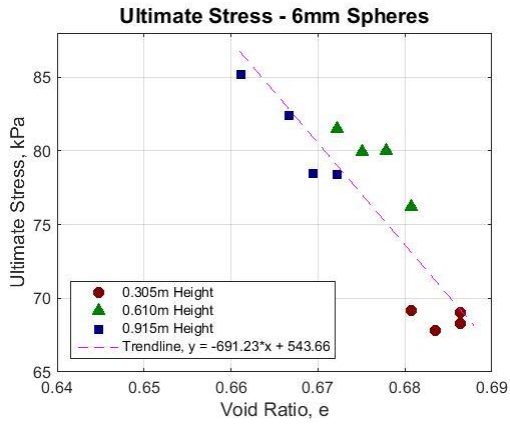


Figure 14. Ultimate stress of 6mm diameter sphere sample versus void ratio.

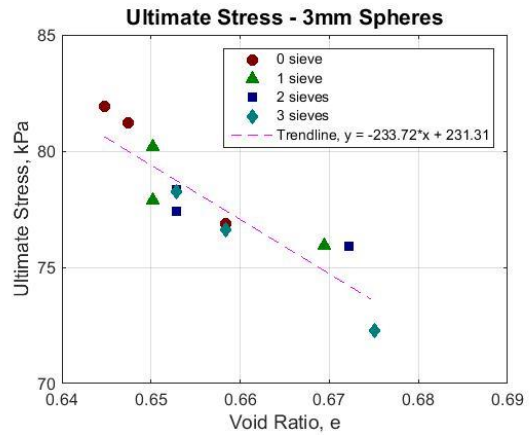
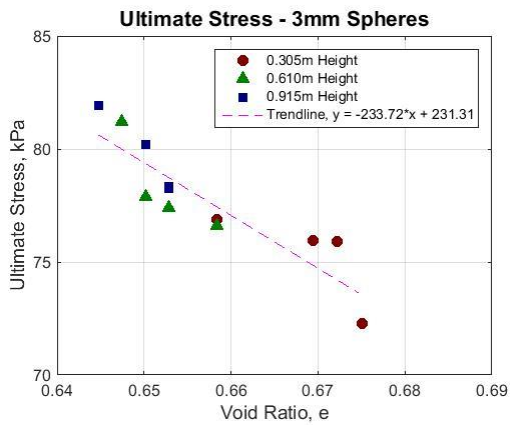


Figure 15. Ultimate stress of 3mm diameter sphere sample versus void ratio.

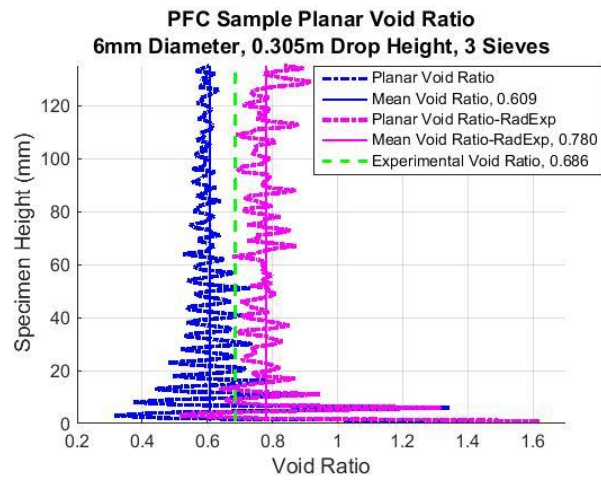
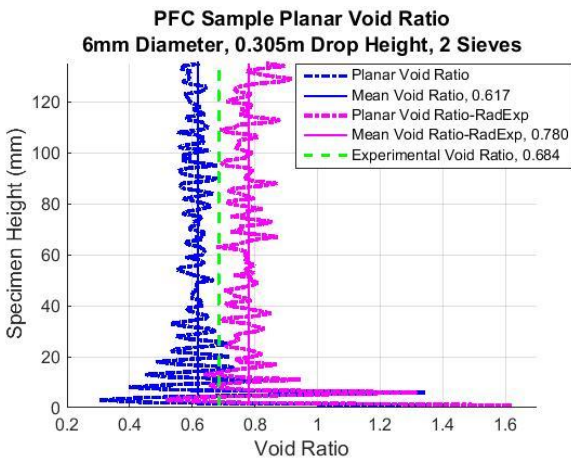
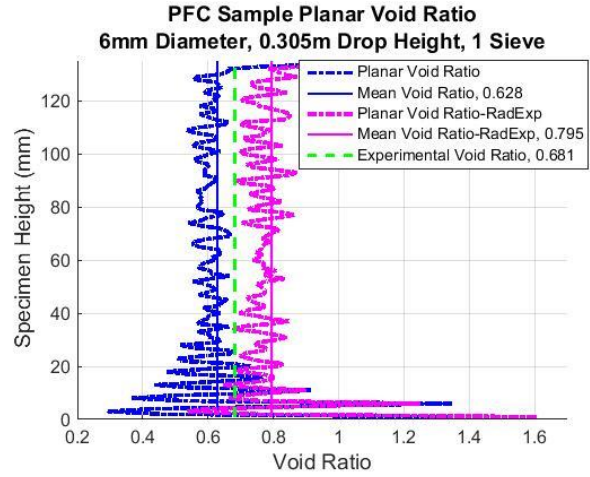
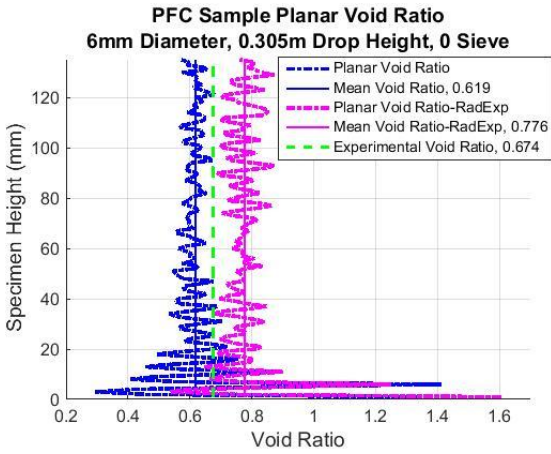


Figure 16. Comparison of void ratio variation of samples prepared from 0.305m drop height using air pluviation method and radius expansion method.

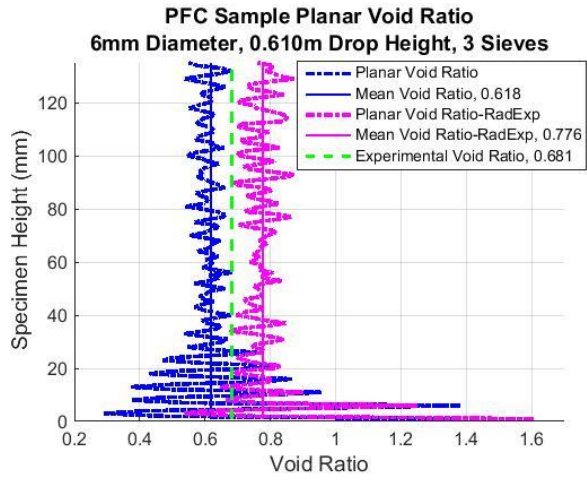
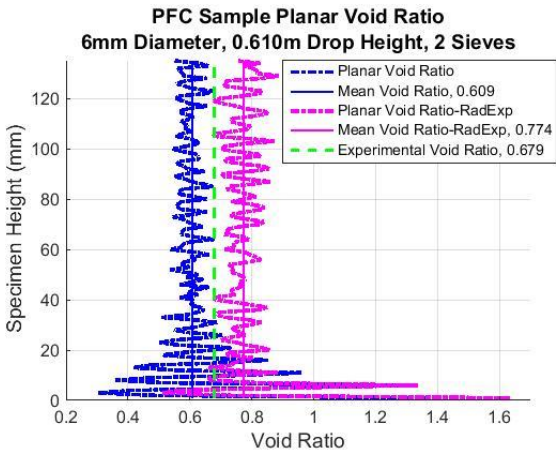
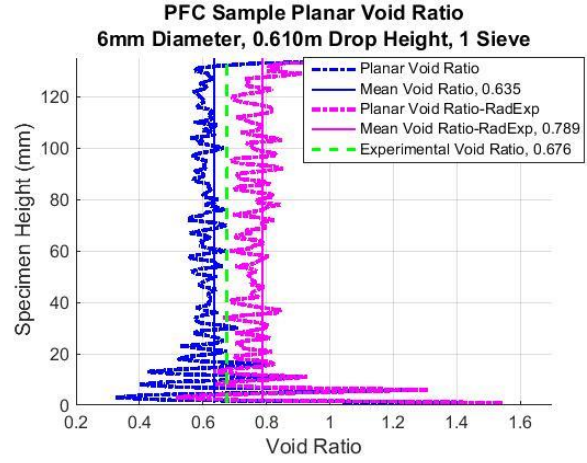
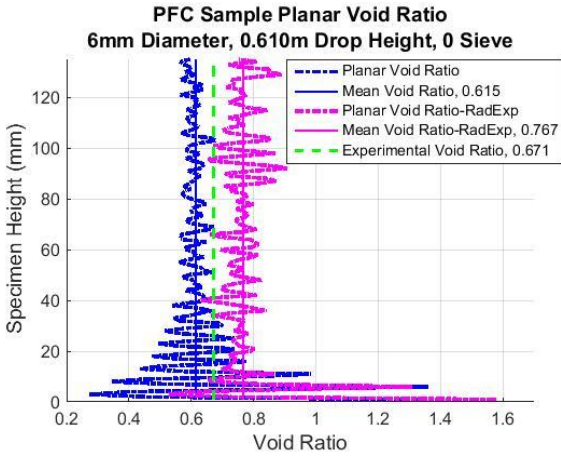


Figure 17. Comparison of void ratio variation of samples prepared from 0.610m drop height using air pluviation method and radius expansion method.

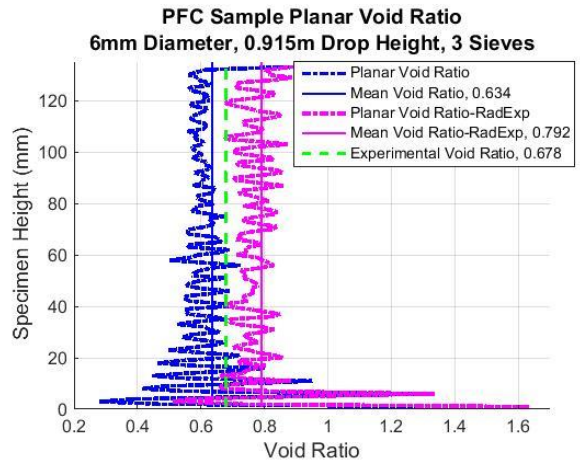
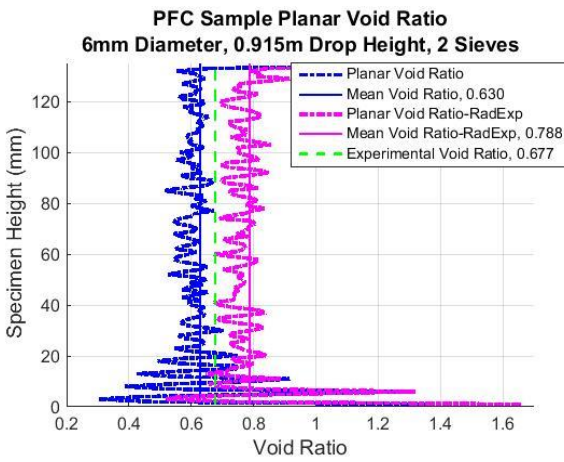
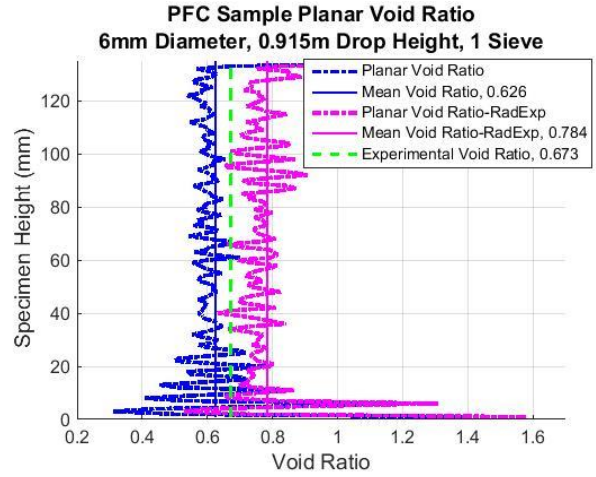
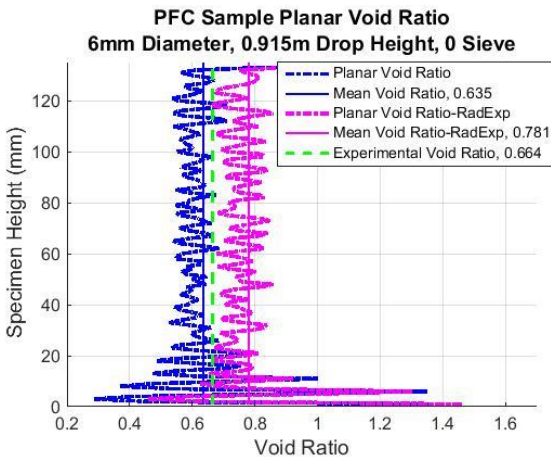


Figure 18. Comparison of void ratio variation of samples prepared from 0.915m drop height using air pluviation method and radius expansion method.

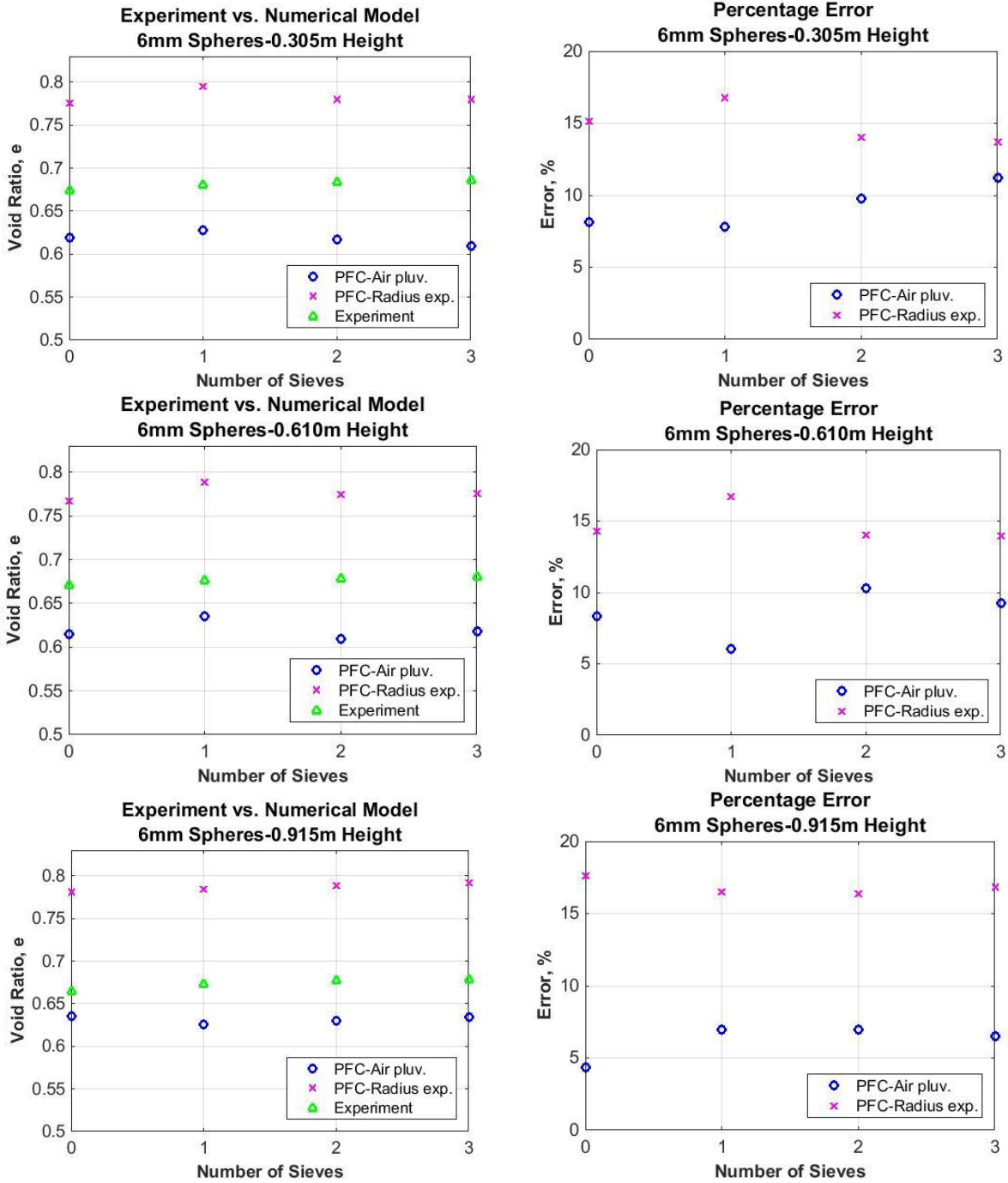


Figure 19. Void ratio of experimental samples and numerical samples (left) and percentage error (right).

## CHAPTER III

### 2D DEM MODELING OF TRIAXIAL COMPRESSION WITH FLEXIBLE MEMBRANE USING UNIFORM PARTICLE SIZE

#### 3.1 Background

In previous study, the effect of sample preparation condition is examined both experimentally and numerically. Air pluviation method is used to prepare the samples of uniform steel spheres at varying heights and distribution levels and a numerical model is built replicating the same experimental condition in PFC3D. It is concluded that the variation in void ratio contributes to the mechanical response of the specimen. This study interests in understanding the micro-properties of DEM model and how they affect the macro-response of the materials under shearing to produce more accurate numerical model. This study aims to reproduce experimental triaxial response of sample made of uniform size steel spheres using PFC2D. Flexible boundary condition is incorporated in the model to obtain the local deformation of the sample as well as the shear band formation.

#### 3.2 Experimental triaxial compression test

A total of 16 triaxial compression tests is performed on uniform size steel spheres of 3 mm and 6 mm diameter. The confining pressure is applied using vacuum and kept constant at 55 kPa throughout the test. The sample is compressed at a loading rate of 0.2% axial strain/min. The stress-strain responses of all triaxial tests performed are presented in previous study. Stress-strain response of the 3 mm and 6 mm diameter sphere samples prepared at 3 ft height using 3 sieves are used to fit the model response. The initial void ratio of the sample is 0.653 for 3 mm sample and 0.672 for 6 mm sample. Figure 20 shows the stress-strain response of the 2 particle size samples.

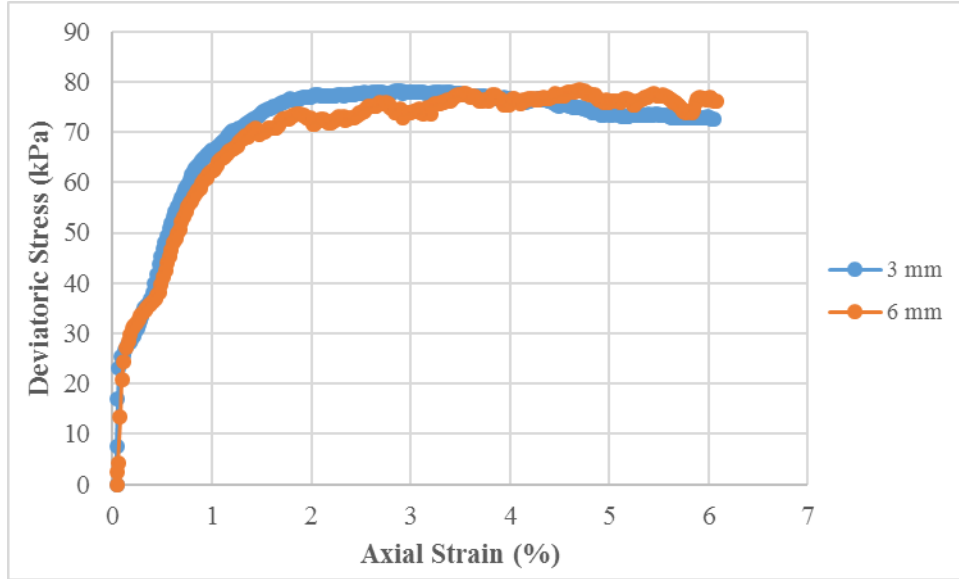


Figure 20. Stress-strain responses of 3 mm and 6 mm diameter samples at the same preparation condition.

### 3.3 DEM model

#### 3.3.1 Background on triaxial modeling in PFC

There have been numerous studies on modeling of triaxial compression test using PFC in the past ten years in both 2D and 3D. The initial models were developed in 2D by Jiang et al. [28], Evans [29-30], Cho et. al. [31], Li and Yu [32], and so on. 3D models are developed shortly after by Kuhn [33], Cui et. al. [34], Chueng and O’Sullivan [35], Wang and Tonon [36], de Bono et. al. [37-38], and ect.. In the DEM, the macroscopic parameters of the material like deformation, strength, strain, stress etc. are reproduced by the micro parameters of the material such as normal and shear particle stiffness, local friction, damping coefficient etc. There are attempts to develop laboratory test as a way to quantify the micro parameters of the model. However, the most common method is to tune the parameter using trial-error method.

### 3.3.2 Calculation cycle-Quasi-static condition-Inertia number-Critical time step & Model scaling

Calculation sequence of PFC adopts a time-stepping algorithm which alternates between the force-displacement law to each contact and the Newton's Second Law (Law of Motion) to each particle and constantly updates particles positions during every calculation cycle [40]. It is important to maintain quasi-static condition during the simulation to obtain stability result. Inertial number,  $I = \frac{\dot{\epsilon} d_{50}}{\sqrt{p'/\rho}}$ , where  $\dot{\epsilon}$  is strain rate,  $d_{50}$  is mean particle diameter,  $p'$  is mean effective stress and  $\rho$  is material density; is used as a limit for maintaining quasi-static deformation in all simulations. Inertial number quantifies the inertia effects by calculating ratio between the inertial forces and imposed forces for identifying quasi-static regime, dense flow regime and collision dynamic regime. Inertial number should always remain smaller than  $10^{-3}$  for quasi-static state [41]. Critical time step is known to be linear proportional to a square root of material mass to material stiffness ratio, ( $\Delta t_{cri} \propto \sqrt{m/k}$ ). Small time step will cost computational efficiency so one method to reduce computational time is called density scaling the experimental model by deactivate gravity and increase sample and particle sizes by a constant factor without changing the material stiffness [42-43]. Thakur et. al. investigated on the scaling laws for cohesionless and cohesive solid. He found an agreement in the macroscopic and microscopic behaviors for different particle sizes when the contact stiffness was scaled linearly with the size [44].

### 3.3.3 Boundary condition

Rigid boundary condition is the most common boundary type used in DEM model. The stresses on the rigid walls are calculated by summing all the ball-wall contact forces and dividing by the

wall area. The desired confining pressure is obtained by applying a velocity to the wall using a numerical servo-control mechanism. Another boundary type is periodic boundary wall which consists of recurring copies of periodic cell capturing the material response. This boundary type is useful for asymmetric problems. However, the local deformation of the sample cannot be captured similarly to rigid boundary. The flexible boundary is adopted to replicate the deformability of latex membrane in laboratory tests. The confining stress is either applied directly to the peripheral particles of the sample or applied to the boundary made of particles [29]. This study adopts the flexible boundary developed by Evans and Frost that is composed of chains of particles that connect using simple linear contact bond model. The contact tensile strength is set with high value to accommodate for the stretching/elongation of the membrane. During deformation, membrane particles are added/removed to maintain sufficient coverage of the specimen and prevent bunching behavior of the membrane to the top and bottom walls [30].

#### 3.3.4 Contact model

A simple linear contact model consists of a spring and dashpot acting in parallel with one another is used in this study. Components of the contact parameter for steel spheres include the effective modulus, normal to shear stiffness ratio and friction coefficient. For the membrane, linear contact bonding model is used to prevent particle separation but does not transmit moment. Detailed description of the linear contact model and linear contact bond model can be found in the PFC user manual [40]. The stiffness of the membrane is set 1/10 less stiff than the material stiffness while the contact bond strength is set significantly larger than the testing material stiffness to prevent bond breakage. Properties of the steel spheres and the membrane are adopted from Bernhardt's study [45]. Table 3 provides list of model parameters used in this study.

Table 3. Triaxial model parameters in PFC2D for steel spheres.

Components	Parameters	Value
Steel spheres	Effective modulus, E*(Pa)	2e11
	Normal-shear stiffness ratio, krat	1.5
	Friction coefficient	0.096
Membrane	Effective modulus, E*(Pa)	2e10
	Normal-shear stiffness ratio, krat	1.0
	Friction coefficient	0.31
	Bond strength, (Pa)	1e20
Wall	Effective modulus, E*(Pa)	2e11
	Normal-shear stiffness ratio, krat	1.0
	Friction coefficient	0.45
Loading condition	Confinement pressure (Pa)	55e3
	Loading rate (%/min)	0.2

### 3.3.5 Parametric study

The sample initial created contains desired number of particles randomly generated over an enlarge sample size using rigid walls. Then the sample is equilibrated and consolidated to desired consolidation stress using the numerical servo algorithm controlling the wall velocity. After that, the two vertical rigid walls are replaced with flexible walls made of chains of particles. The sample is recalibrated again before starting compression. The bottom wall is accelerated at a rate similar to the experiment loading rate (0.2% axial strain/min) while maintaining confining stress at the membrane. The sample and particle sizes are scaled up 100 times to reduce computational time while maintaining quasi-static condition. Gravitational effect is disable in the simulation. Parametric study is performed by varying one parameter at a time to capture the influence of each parameter to the overall response of the model. Parameters that subjected to the sensitivity analysis are the effective modulus and the friction coefficient.

### 3.4 Numerical result

Simulations of triaxial compression test are performed in PFC2D with inertial number within the order of  $10^{-4}$ . Sensitivity analysis is performed for 6 mm sample to save computational effort. Starting with the effective modulus, the material yields unreasonable high strength response when using the input value of  $2.0 \times 10^{11}$  Pa. Therefore, the modulus is reduced until matching with the experimental response. Figure 21 shows the changes in stress-strain curve of the sample with corresponding to the changes in effective modulus. Then, the friction coefficient is also varied to learn more about the sample responses (Figure 22). It is observed that increasing the modulus changes the peak stress in the stress-strain curve. However, the change in the slope is not clear and consistent. The sample response to the friction coefficient changes seems more reasonable as friction increases the material strength increases. After the calibration, model responses are checked with the experimental triaxial results for 6 mm and 3 mm particles sizes (Figure 23-24). Large fluctuation in the model stress-strain curves can be caused by the crystallize effect for using uniform particle size in the model. Deformed shape, velocity field and accumulative contact forces map of the DEM model are shown in Figure 25-26.

### 3.5 Discussion

The 2D DEM model with flexible membrane is developed attempted to replicate the triaxial sample response for steel particles. There are a few concerns about the model behavior: the model stress-strain curves experience a lot of fluctuation during the simulation; the sample seems to have crystalline condition during consolidation which can affect the stress-strain behavior; the formation of the shear band heavily depends on the particle arrangement. Some improvement can

be made by including small range of particle size  $\pm 10\%$  of particle size to better accommodate particle arrangement or developing a 3D triaxial model with flexible membrane.

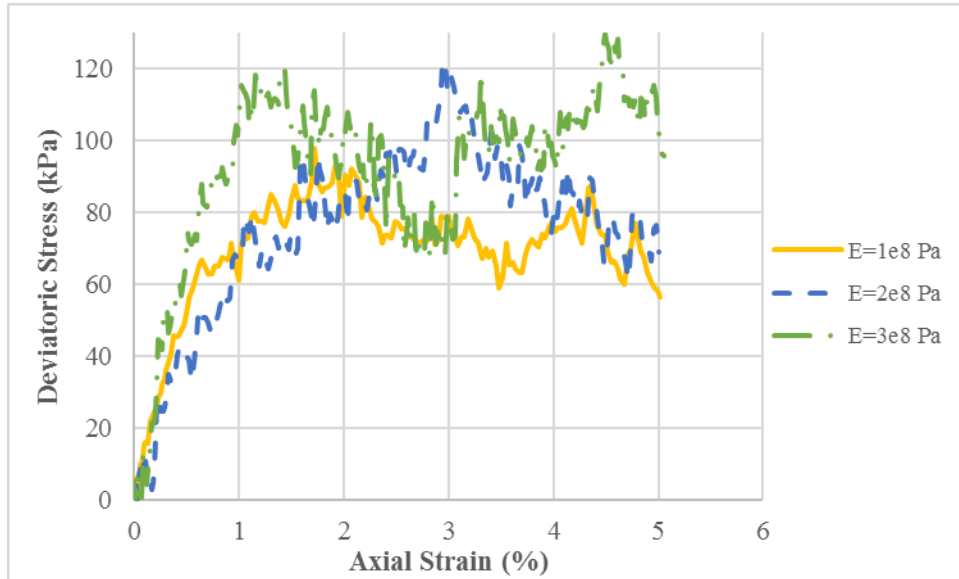


Figure 21. Model response to varying modulus of elasticity.

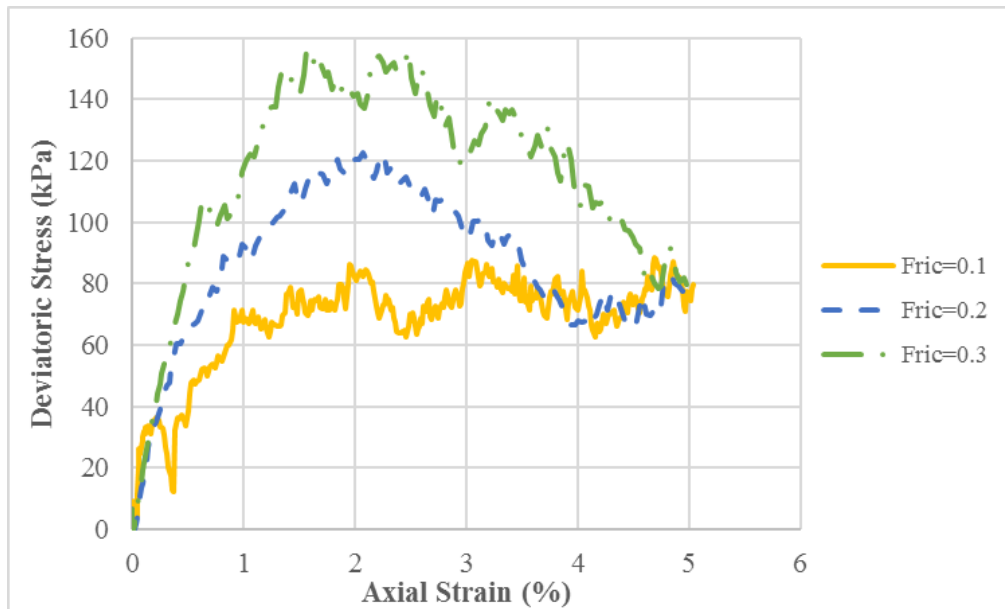


Figure 22. Model response to varying friction coefficient.

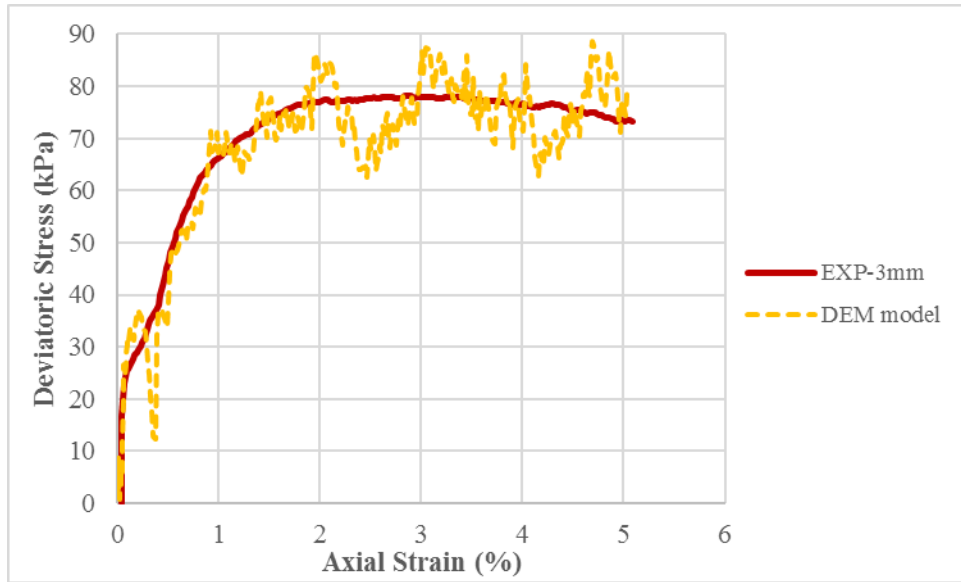


Figure 23. DEM model versus experimental response for 3 mm particles.

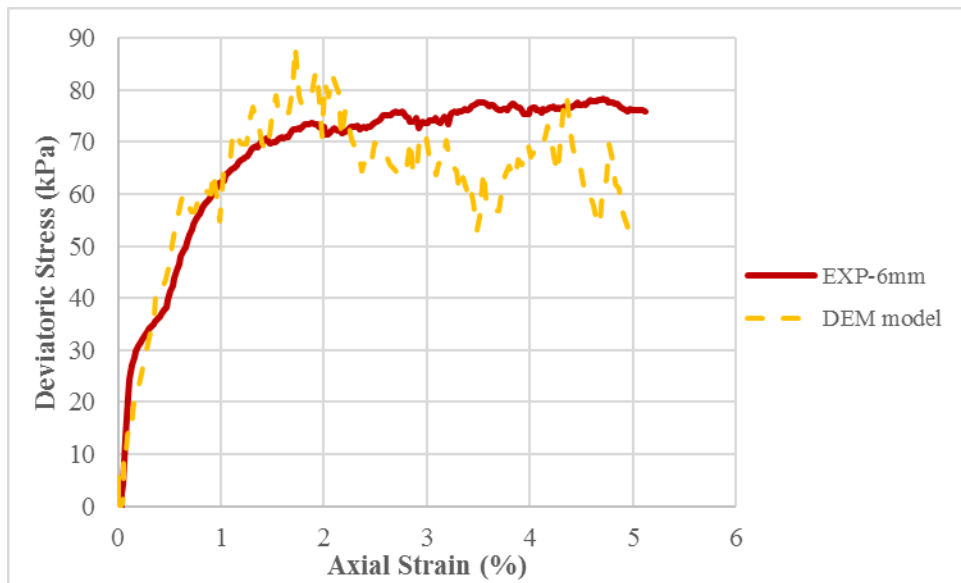


Figure 24. DEM model versus experimental response for 6 mm particles.

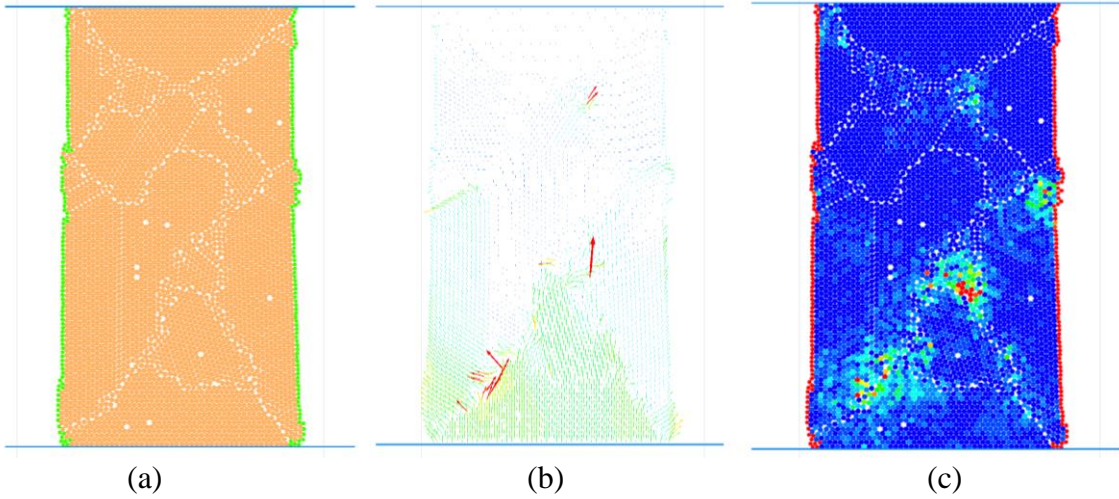


Figure 25. Sample deformation (a), velocity field (b), and accumulative contact force map (c) obtained from DEM simulation for 3 mm particles.

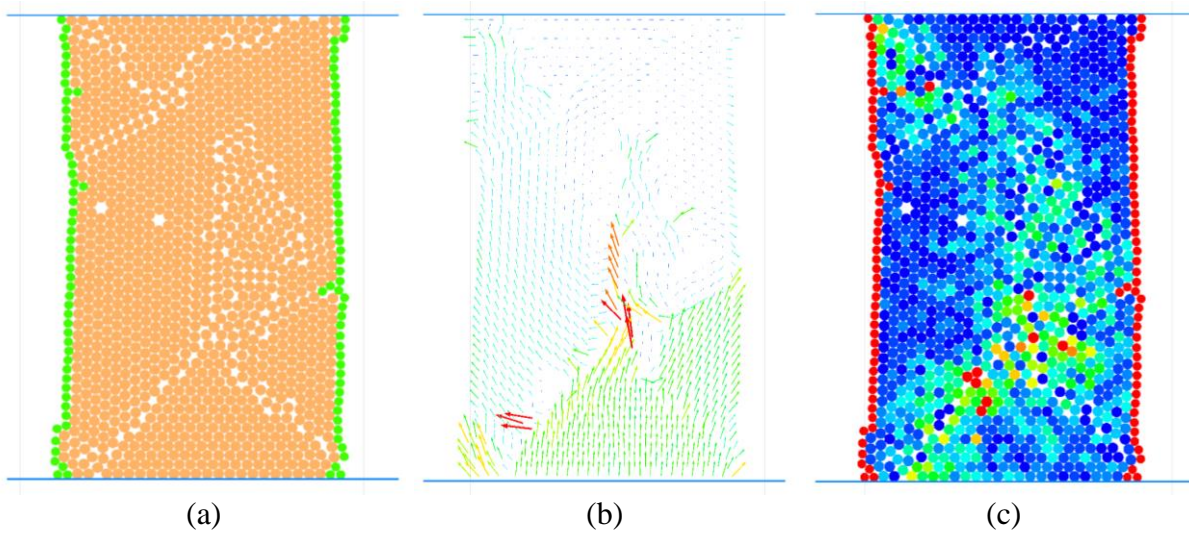


Figure 26. Sample deformation (a), velocity field (b), and accumulative contact force map (c) obtained from DEM simulation for 6 mm particles.

CHAPTER IV  
CALIBRATION OF GRANULAR MATERIALS UNDER TRIAXIAL COMPRESSION  
USING DEM

4.1 Background

One of the main challenges using the discrete element method is to specify accurate model micro parameters to produce quality simulation results. Calibration of micro parameters to meet laboratory results is often done by trial-error tuning the parameters manually [46-54]. This process is time consuming and might not cover the full description of the parameter behavior in space. Thus, it is important to establish a better and efficient method to calibrate DEM micro-parameters. The use of probabilistic approach is first introduced by Medina-Cetina and Khoa to quantify the uncertainty associated to the area selection of the DEM parameters using Bayesian paradigm to obtain the complete solution to the inverse problem [55]. Zhang followed the approach to calibrate micro-parameters of sandstone [56]. A set of nine micro parameters are selected to conduct a sensitivity analysis for better understanding the correlations between parameters with respect to the global behavior of the sample (Table 4). Then the Bayesian paradigm is used to solve the inverse problem for model calibration. The Bayesian theorem is defined as below:

$$\pi(\theta|d_{\text{obs}}) = \frac{f(d_{\text{obs}}|\theta)\pi(\theta)}{\int f(d_{\text{obs}}|\theta)\pi(\theta)d\theta} = \frac{f(d_{\text{obs}}|\theta, g(\theta))\pi(\theta)}{\int f(d_{\text{obs}}|\theta, g(\theta))\pi(\theta)d\theta} \quad (3)$$

where  $\pi(\theta)$  is the prior,  $f(d_{\text{obs}}|\theta)$  is the likelihood, and  $\pi(\theta|d_{\text{obs}})$  is the posterior of the process. The prior is obtained from previous knowledge of the parameters and the likelihood measures the predictive parameter behavior. The posterior is defined by the integration of the combine effect of the prior and the likelihood, which is also the solution of the inverse problem. It is assumed that

each observation is independent and the error at each data point follows Gaussian distribution. The likelihood can be calculated from each data point within the strain range:

$$f(d_{\text{obs}}|\theta) \propto \sum_{i=2}^{n-1} \left( \frac{d_{\text{obs}}(\varepsilon_{a_i}) - d_{\text{prep}}(\varepsilon_{a_i})}{\sigma(\varepsilon_{a_i})} \right)^2 \quad (4)$$

where  $d_{\text{obs}}$  is the value of the current observation and  $\sigma_{\text{obs}}$  is the value of the standard deviation. The Markov Chain Monte Carlo method (MCMC) is used to perform sampling of the posterior. The calibration process will converge to the target joint density as the sample grows. In addition, the Metropolis-Hastings (MH) algorithm is used to determine which sample is accepted or rejected during sampling. The MH criteria provides the probability of accepting or rejecting a candidate point whose values are used to run the simulation ( $\alpha$ ). The decision parameter,  $\alpha$ , can be obtained as:

$$\alpha(\hat{\theta}_s, d_{\text{obs}}) = \min \left\{ 1, \frac{\pi_{\text{Proposed}}}{\pi_{\text{Previous}}} \right\} = \min \left\{ 1, \frac{\pi(Y|d_{\text{obs}})q(\hat{\theta}_s|Y)}{\pi(\hat{\theta}_s|d_{\text{obs}})q(Y|\hat{\theta}_s)} \right\} \quad (5)$$

After completing the calibration process, first order statistic of the model response is plotted to compare with the experimental result. The numerical and experimental stress-strain behaviors show good agreement which proves the efficiency of the probabilistic calibration in DEM simulation [56].

Table 4. Micro parameters as variables in Zhang’s probabilistic calibration. Reprint from [56].

Micro-parameter	Symbol	Unit	Sample
Contact Young’s modulus	$\theta_1 = E_c$	GPa	12.1
Ratio of contact normal to shear stiffness	$\theta_2 = k_n/k_s$	-	6
Inter-particle friction coefficient	$\theta_3 = \mu$	-	3.0
Parallel bond Young’s modulus	$\theta_4 = E_{cp}$	GPa	12.1
Ratio of bond normal to shear stiffness	$\theta_5 = k_{np}/k_{sp}$	-	8
Average bond tensile strength	$\theta_6 = \sigma_c$	MPa	60
Standard deviation in bond tensile strengths	$\theta_7 = \sigma_d$	MPa	6.0
Average bond shear strength	$\theta_8 = \tau_c$	MPa	60
Standard deviation in bond shear strength	$\theta_9 = \tau_d$	MPa	6.0

#### 4.2. Problem definition

It is hypothesized that the uncertainty of micro-parameters used in DEM models can be quantified by applying the Bayesian paradigm to solve the inverse problem. This study aims to calibrate micromechanical parameters laboratory sand subjected to triaxial compression using Bayesian paradigm to solve the inverse problem.

#### 4.3 Methodology

Since the Bayesian paradigm requires running thousands of simulation to fully capture the probabilistic distribution of the model parameters, it is proposed to build a DEM model in two dimensions initially to simplify the problem as well as reduce the computational time to run the simulations. The 2D model is required initial calibrations by trial-error to replicate the material response of true triaxial compression test and to understand the sensitivity of each model parameter before starting the probabilistic calibration process. Figure 27 presents the flow chart of the calibration process.

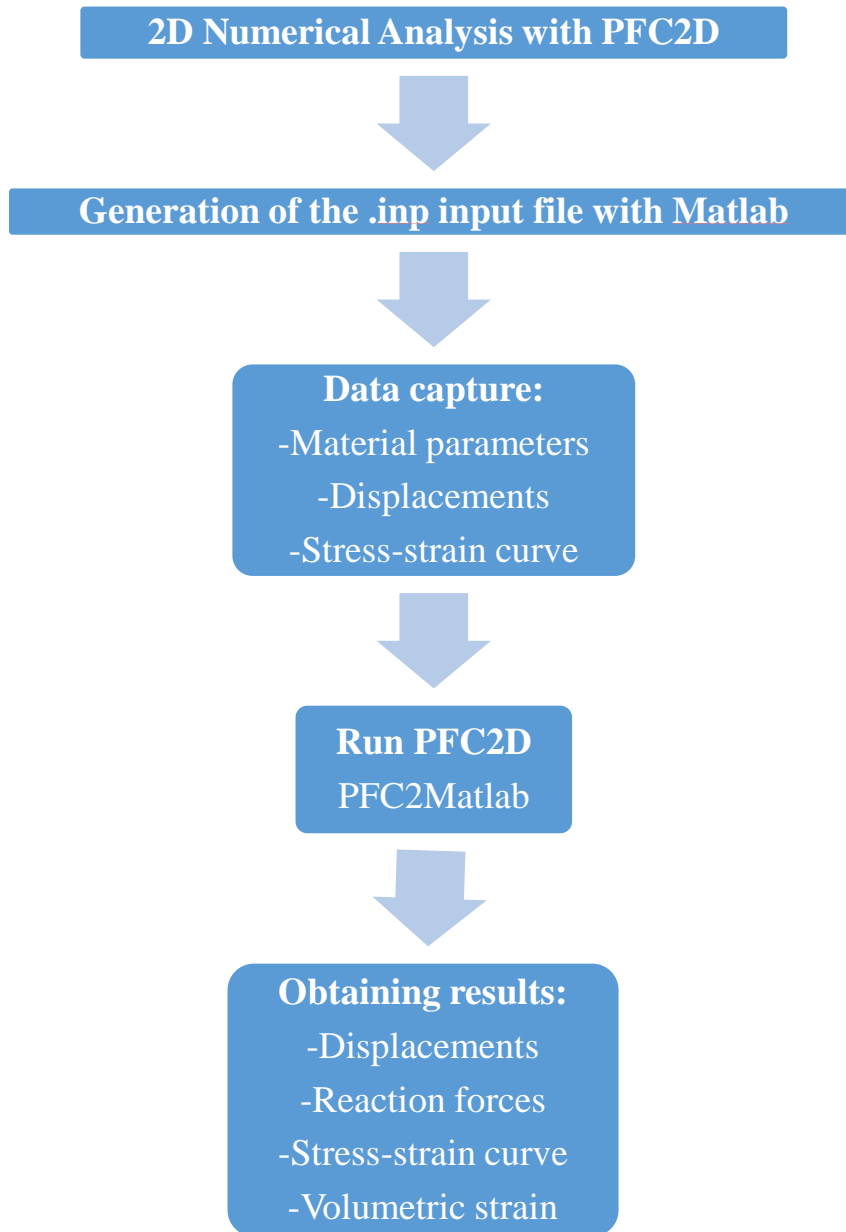


Figure 27. Schematic procedure of the probabilistic calibration process.

#### 4.4 Experimental data

The triaxial experimental data is based on a comprehensive experimental database containing a series of triaxial compression tests on sand performed by Medina-Cetina [57]. The sand specimens,

classified as SP, having  $C_u=2.34$  and  $C_c=1.11$ ,  $d_{50}=0.5\text{mm}$ , average relative density about 91.72% with initial density of  $1,720\text{ kg/m}^3$ . The sample chosen for this study was prepared in a standard size mold ( $D=71\text{ mm}$  and  $H=155\text{mm}$ ) by vibratory compaction and vacuum consolidated and confined at 40 kPa. The sample was then compressed at a constant loading rate of 0.2%. Figure 28 shows the stress-strain response of the sand specimen. From the curve, the estimate Young's modulus of the sample is approximately 25 MPa and the friction angle is approximately  $48.5^\circ$ . The experimental data will be used as input parameters for the initial simulation.

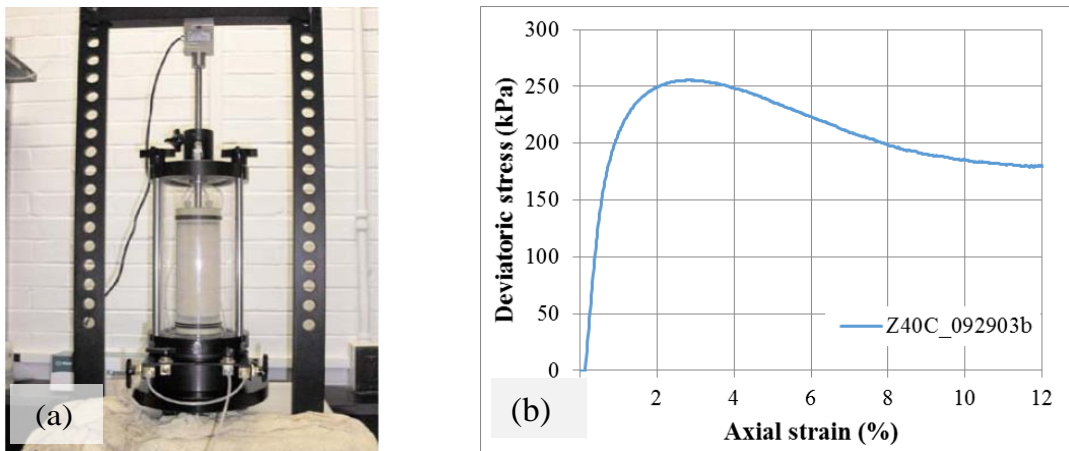


Figure 28. The triaxial system and the selected stress-strain response. Reprint from [57].

## 4.5 DEM model

### 4.5.1 DEM model of triaxial compression test

A simplified 2D model of the triaxial compression test is built in PFC2D to replicate the experimental result. The reason for choosing 2D instead of 3D model is that 2D model can provide initial response of the samples without costing too much computational effort. However, there is a difference in stress-strain responses between 2D and 3D tests. Ahmed performed an experimental study on the difference between plane strain and triaxial test response at various confining

pressures and found that at the same confinement, plane strain sample experienced higher particle crushing than the triaxial sample which led to larger degree of softening after reaching the peak stress [58]. Due to that reason, the 2D model aims to replicate the triaxial response up to 4% axial strain or right after the peak stress. The loading conditions, confining pressure and loading rate, remains similarly to the experimental conditions since they can contribute to the changes in material response. Figure 29 presents the DEM model of sand specimen with flexible membrane boundary.

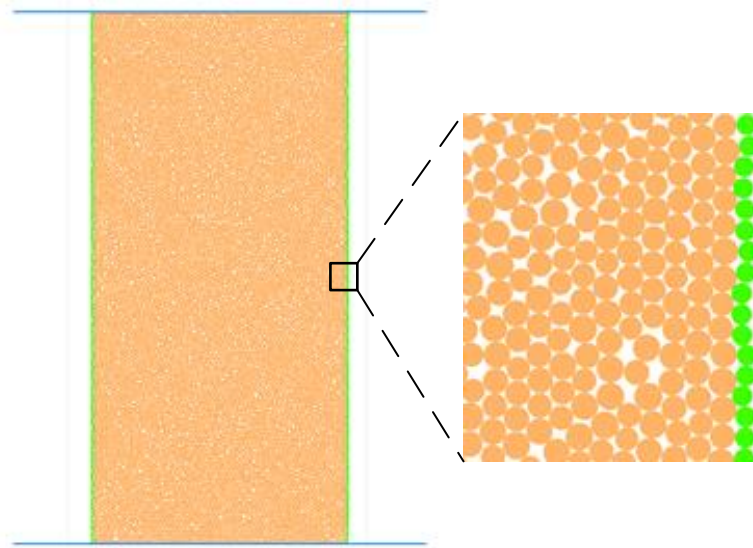


Figure 9. DEM model of consolidated sand specimen with flexible membrane.

#### 4.5.2 Model scaling

The model is scaled up to reduce computational time step while turning of gravitational effect and keeping the material properties the same. The inertial number is also calculated to make sure if the simulation is within the quasi-static regime. The inertial number for the 2D triaxial model in this study is in the range of  $10^{-4}$ . Table 5 presents the dimensions of the model before and after scaling.

Table 5. Model dimensions before and after scaling.

Components	Dimensions	Experiment	Scaled up
Specimen	Diameter (m)	71.5e-3	7.5
	Height (m)	150e-3	15.0
Sand particles	D <sub>50</sub> (m)	0.5e-3	0.5

#### 4.5.3 Contact model

Linear contact model is used for replicating sand behavior. The linear contact model, consists of a linear spring and dashpot acting parallel to each other, whose parameters include the effective modulus, normal to shear stiffness ratio and friction coefficient. For the membrane, linear contact bonding model is used to prevent particle separation but does not transmit moment. Rolling resistance is added to the model to provide an additional torque acting on the contacts to reduce rolling motion. The rolling resistance feature enhances the strength of the material at the contact points which is crucial to replicate the inter-particle friction between irregular shaped particles when using uniform spherical shape in the model. Detailed description of the linear rolling resistance contact model and linear contact bond model can be found in the PFC user manual [59]. Table 6 presents list of micro parameters used in the triaxial model.

#### 4.5.4 Flexible boundary

Flexible boundary condition is established in the model. The membrane model follows Evans and Frost's study that composes of chains of particles connected by using simple linear contact bond model. The contact tensile strength is set with high value to accommodate for the stretching/elongation of the membrane. During deformation, membrane particles are added/removed to maintain sufficient coverage of the specimen and prevent bunching behavior of the membrane to the top and bottom walls [60].

Table 6. Triaxial model parameters in PFC2D for sand.

Components	Parameters	Value
Sand	Radius (m)	0.45-0.55
	Density (kg/m <sup>3</sup> )	1,720
	Effective modulus, E*(kPa)	2.5e4
	Normal-shear stiffness ratio, krat	1.5
	Friction coefficient	1.11
	Rolling friction coefficient	0.2
Membrane	Radius (m)	0.4
	Density (kg/m <sup>3</sup> )	1,500
	Effective modulus, E*(kPa)	2.5e3
	Normal-shear stiffness ratio, krat	1.0
	Friction coefficient	0.31
	Bond strength, (kPa)	1.0e20
Wall	Effective modulus, E*(kPa)	2.5e4
	Normal-shear stiffness ratio, krat	1.0
	Friction coefficient	0.35

#### 4.5.5 Parameter study

Initially, the numerical model is run using the actual material properties measured from the stress-strain response (Young's modulus and friction coefficient). Normal to shear stiffness ratio and rolling friction coefficient are assumed based on previous studies. Then, one parameter among the four parameters is changed each time to obtain the difference in sample response. Wall and membrane parameters are kept constant throughout the sensitivity analysis. Table 7 presents a list of micro parameters used in sensitivity analysis.

Table 7. Micro parameters for sensitivity analysis of sand.

Parameter	Symbol	From experiment
Effective modulus, E*(kPa)	$\theta_1 = E^*$	25,000
Normal-shear stiffness ratio, krat	$\theta_2 = k_n/k_s$	-
Friction coefficient	$\theta_3 = \mu$	1.11
Rolling friction coefficient	$\theta_4 = \mu_r$	-

## 4.6 Preliminary result

### 4.6.1 First simulation

First simulation is run using the  $\theta_1$  and  $\theta_3$  obtained from the experiment and assuming  $\theta_2=1.5$  and  $\theta_4=0.2$ . The stress-strain response is shown in Figure 30. It is observed that the model response behaves much softer than the experimental response. Thus, the model effective modulus,  $\theta_1$ , is adjusted next.

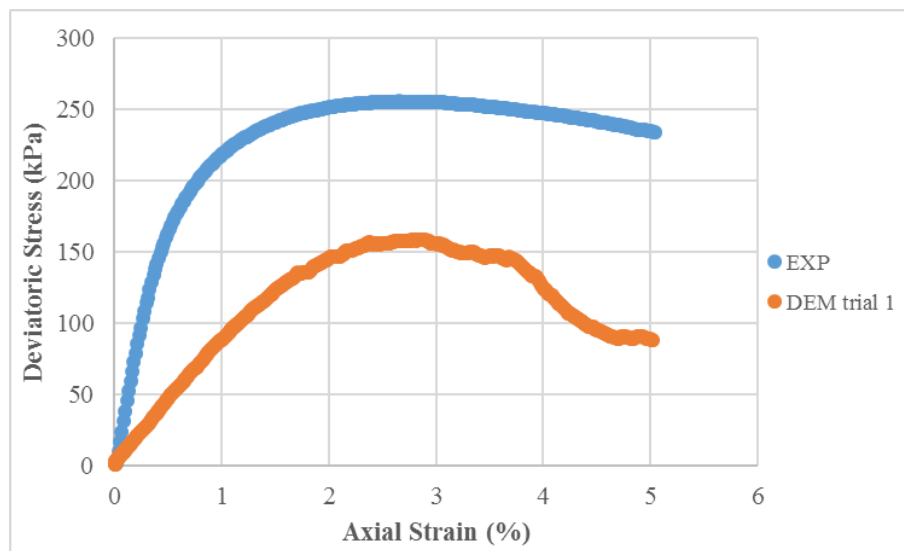


Figure 30. Initial model response comparing to the experimental data.

### 4.6.2 Contact stiffness

A series of simulations with different model effective modulus values are carried on to match with the experimental slope of stress-strain curve. The result of varying  $\theta_1$  parameter is shown in Figure 31. It is observed that the slope increases as the effective modulus increases. The overall strength rises up a little but still does not meet the experimental response.

#### 4.6.3 Normal to shear stiffness ratio

Calibration of the parameter  $\theta_2$ , normal to shear stiffness ratio, is performed and showed in Figure 32. There is no clear effects on changing the sample response so this parameter would remain the original value.

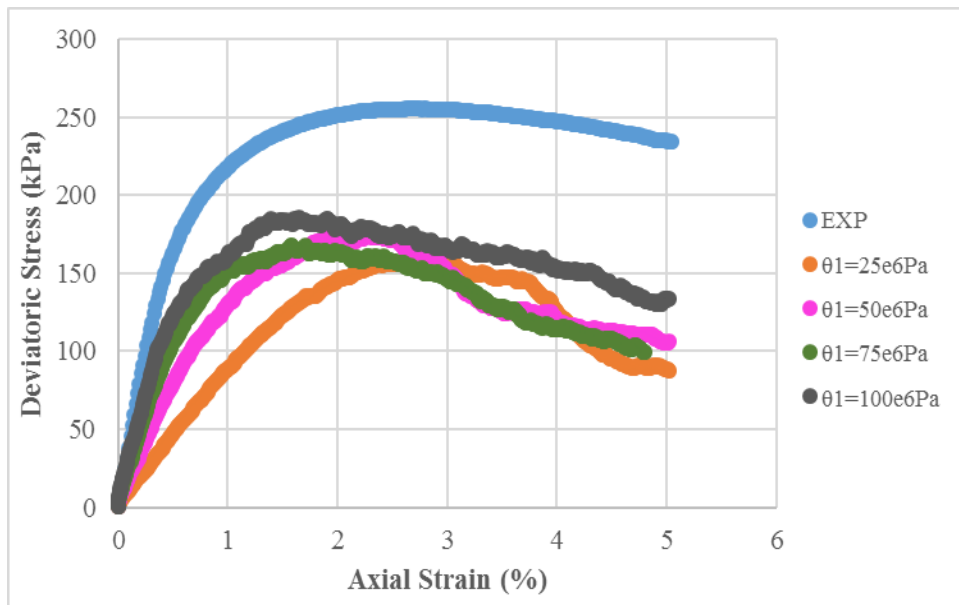


Figure 31. Model responses to varying parameter  $\theta_1$ .

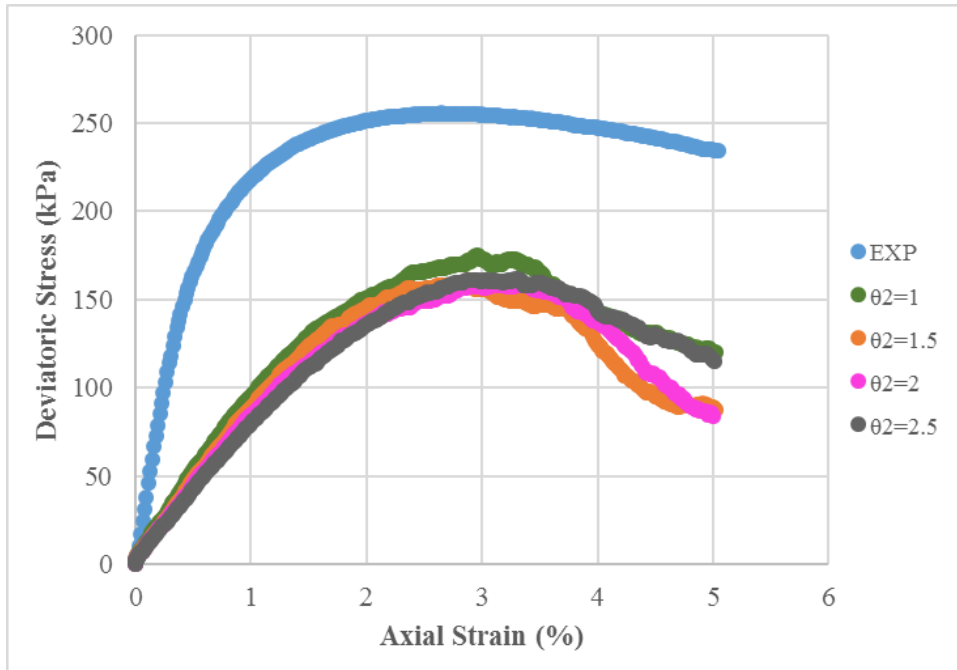


Figure 32. Model responses to varying parameter  $\theta_2$ .

#### 4.6.4 Friction coefficient

The result of varying friction coefficient is shown in Figure 33. It is seen that by increasing friction coefficient, the overall peak strength of the material increases even though the rate of change is not significant. Friction coefficient is related to the friction angle of material ( $\mu = \tan \varphi$ ).

#### 4.6.5 Rolling resistance friction coefficient

Rolling friction is used to add additional strength to the material that accounts for the effect of particle shape. Figure 34 shows the effect of changing rolling friction coefficient to the material response. Clearly, the rolling friction plays a major role in strengthening the material behavior. The material strength increases about 20 kPa by increasing the rolling friction coefficient by 0.1.

#### 4.6.6 Validation with experimental response

Using the results from the sensitivity analysis, the true micro parameters that yield the response closet to the experimental result is obtained (Table 8). Figure 35 compares the DEM response with the experiment. The slope and the peak stress match up pretty well with the experimental result until the softening behavior starts around 3.5% axial strain. The softening phase in the DEM model is as expected since it is in 2D plane strain and the experimental data is 3D triaxial compression which shows agreement with Ahmed’s study [58]. Deformed shape, velocity field and accumulative contact forces map of the DEM model are shown in Figure 36.

Table 8. Micro parameters of sand after calibration.

Parameter	Symbol	Before calibration	After calibration
Effective modulus, $E^*$ (kPa)	$\theta_1 = E^*$	25,000	100,000
Normal-shear stiffness ratio, $krat$	$\theta_2 = k_n/k_s$	1.5	1.5
Friction coefficient	$\theta_3 = \mu$	1.11	1.11
Rolling friction coefficient	$\theta_4 = \mu_r$	0.2	0.42

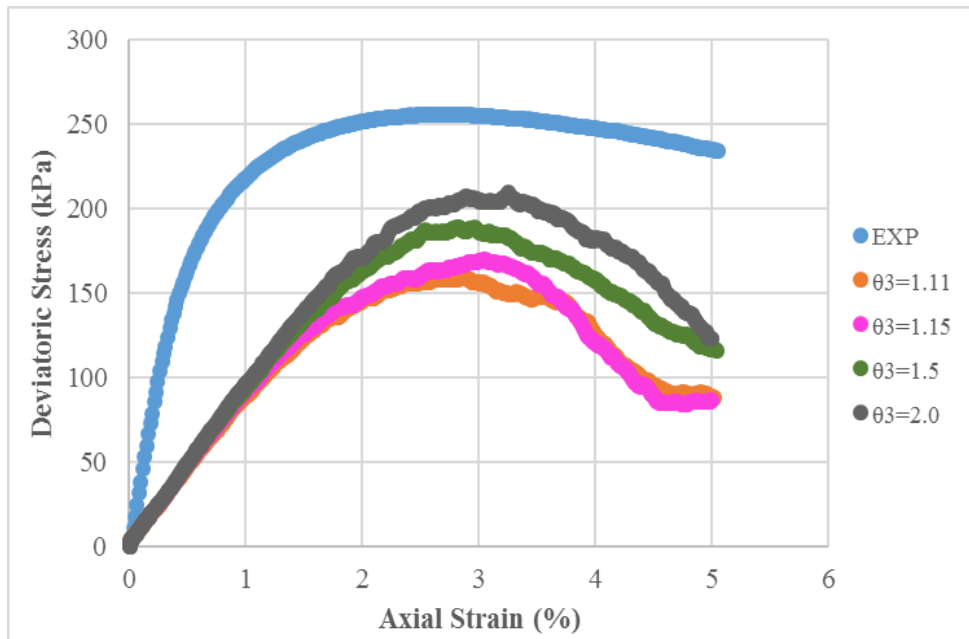


Figure 33. Model responses to varying parameter  $\theta_3$ .

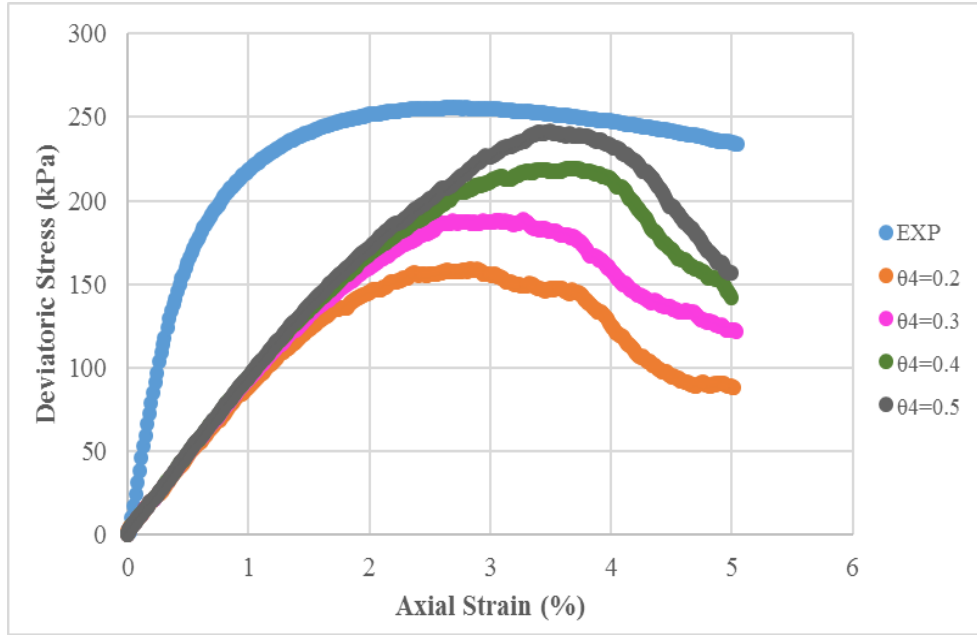


Figure 34. Model responses to varying parameter  $\theta_4$ .

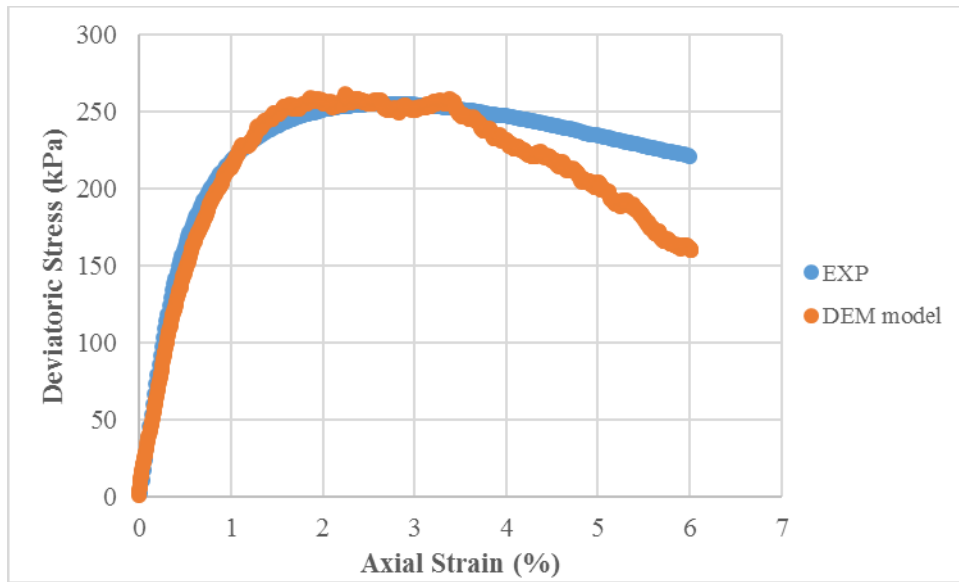


Figure 10. Model responses after calibration process.

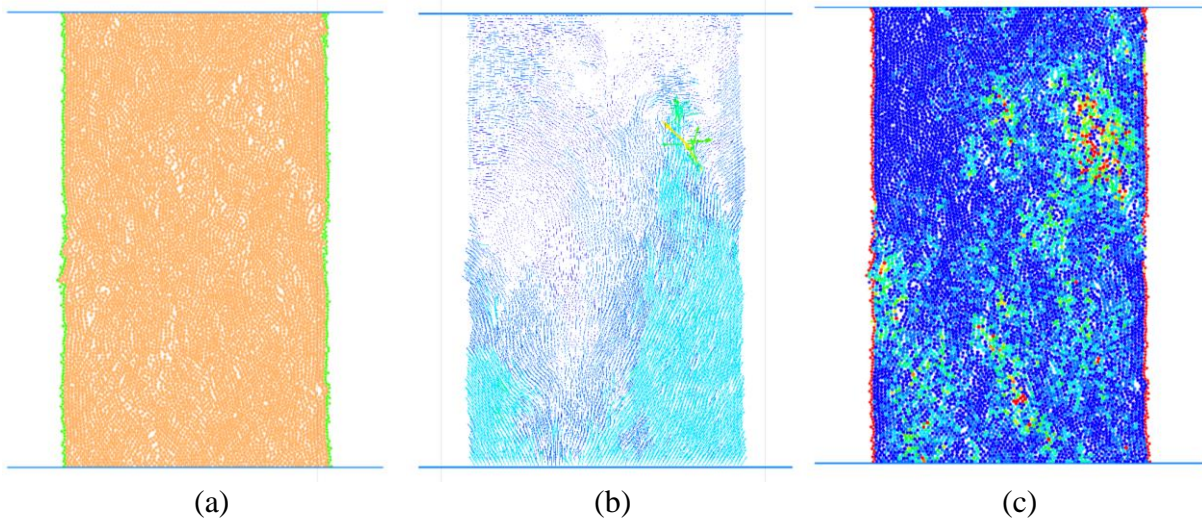


Figure 36. Sample deformation (a), velocity field (b), and accumulative contact force map (c) obtained from DEM simulation.

#### 4.7 Discussion

A DEM model for triaxial compression test is built in PFC2D to replicate the stress-strain behavior of laboratory sand. The model size is scaled up while its material properties remain the same to reduce computational effort while maintaining quasi-static condition. Gravitational effect is not included in the simulations. The preliminary result of this study contains sensitivity analysis on the effect of individual micro parameter to the overall mechanical response of the sample. Even though the 2D model experience significant softening behavior after peak stress, the slope of the stress-strain curve and the peak stress match up well with the experiment data. Four calibrated parameters will be used as initial inputs for the probabilistic calibration process which will be proceeded in the second phase of the study.

## CHAPTER V

### PARAMETRIC STUDY OF THE ASTEROID IMPACT AT CHICXULUB: INTEGRATING GEOLOGICAL FIELD OBSERVATIONS AND DEM MODELING

#### 5.1 Introduction

Studies of planetary asteroid impacts have been popular in the past few decades including examining existing craters on the Earth or on other nearby planets like the moon or mars, formulating possible types of crater formation, developing analytical models for crater formation, and learning about the effects of those massive impacts that relate to current conditions of tectonic plates, geo-environmental, and climate on Earth [61-70, 81]. Among these asteroid craters, the Chicxulub crater, located in the northwestern sector of the Yucatan carbonate peninsula and southern of the Gulf of Mexico, draws most interests due to its association to the worldwide distribution of the Iridium-rich clay layer which naturally marked the Cretaceous/Paleogene (K/Pg) boundary and imposed global environmental and climate change by blockage of solar radiation as well as possible cause for the mass extinction of the dinosaurs on Earth [61]. This study aims to implement the geophysical data collected from the crater site to provide quantification of different impact conditions for better understanding of the crater formation process. Unlike previous numerical models of asteroid impact developed on hydrocode which follows continuum mechanics, this study provides a different approach on modeling impact by following discrete mechanics. The impact model is built on Particle Flow Code (PFC) program in two dimensions. The results of this study can verification the capability of PFC2D in simulating large dynamic problems as well as cross validation with previous numerical estimations performed on iSALE hydrocode program [69-79]. The preliminary results of the DEM model contribute only

to the dry mechanistic effects of the impact, fluid and thermal coupling aspects will be included in the future.

## 5.2 Background on the Chicxulub crater

Since discovered in the 1950s as part of the oil exploration program, the Chicxulub crater, located in the Yucatan carbonate platform southern to the Gulf of Mexico, it has undergone numerous geophysical studies and drilling programs to obtain possible information for studies on cratering formation process, climatic and environmental effects of the impact, the global distribution of Iridium-rich clay layer which marked the K/Pg boundary, and the link between Chicxulub impact to the mass extinction of the dinosaurs [61]. The Chicxulub crater is classified as complex crater that consists of three multi-ring crater with a central peak ring of about 40 km, two lower rings at about 70 km and 120 km as the inner and outer limits of the transient crater wall, and a basin outer rim of about 200 km in diameter [61]. Figure 37 presents the illustration of the Chicxulub complex multi-rings impact crater. The estimated size of the asteroid is about  $10 \pm 4$  km in diameter with a velocity of about 15-22 km/s [61]. The crater formation process consists of several stages. According to French's study [65], the first stage is called the compression stage where the projectile hits the planet surface creating shock waves by conversion of kinetic energy. A part of the shock waves transmitting to the round is reflected back into the asteroid as tensional waves or rarefaction that decomposes, melts and vaporizes the subject. The following stage called the excavation stage which develops the asteroid melt lining in the expanding transient cavity and creates outward ejecta curtain from the opening crater. After that, the modification stage steps in as the over-steepened walls of transient crater or ejecta falling back into the cavity to form a deposit of mixed breccia. The final simple crater type forms a bowl-shaped depression made of mixed

breccia and impact melt bodies. Complex craters are formed due to complex interactions between shock wave effects, gravity, the strength and structure of the target rocks that result in formation of a central uplift and one or more depressed rings toward the crater ring [62]. Figure 38 illustrates the complex crater formation process. Different drilling programs have been conducted at the crater site to obtain the information of the subsurface stratigraphy, structure and material of the underlying sediments for further studies of shock effects, lithologies and deep layer components, including the International Ocean Discovery Program (IODP), the Petroleos Mexicanos (PEMEX) program, the National University of Mexico (UNAM) drilling program, the Chicxulub Scientific Drilling Project (CSDP) and the UNAM drilling program in collaboration with the Federal Commission of Electricity (CFE) [61]. Locations of all previous geophysical explorations and drilling studies are presented in Figure 39 followed the IODP Expedition 364 report [79]. Drilling cores were collected at the boreholes and subjected to different tests and scanning to classify the materials and obtain their physical properties. Figure 40 presents sample of the stratigraphic columns collected at different borehole locations. Based on the information acquired from the core samples, the corresponding Chicxulub crater structure was drawn with respect to drilling locations (Figure 11).

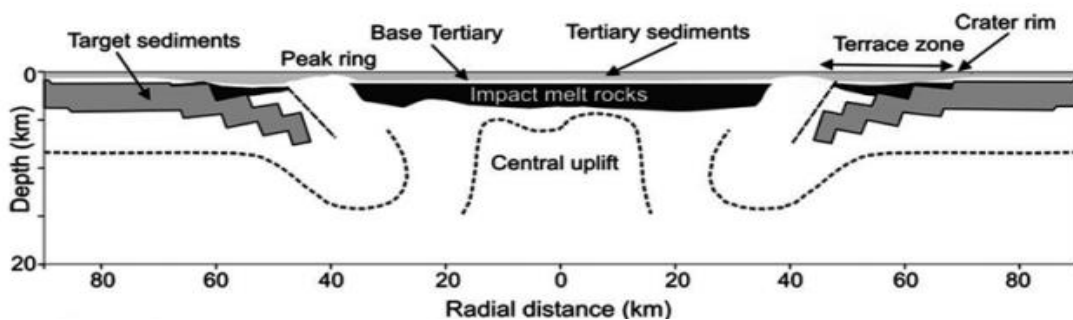


Figure 37. Schematic drawing of the Chicxulub crater. Reprint from [61].

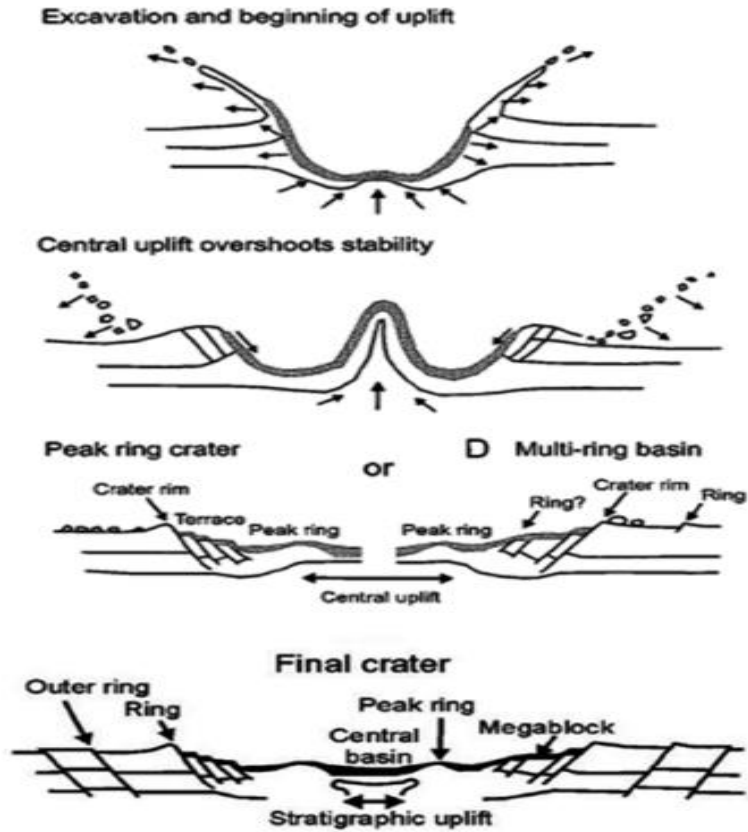


Figure 38. Complex crater formation process. Reprint from [62].

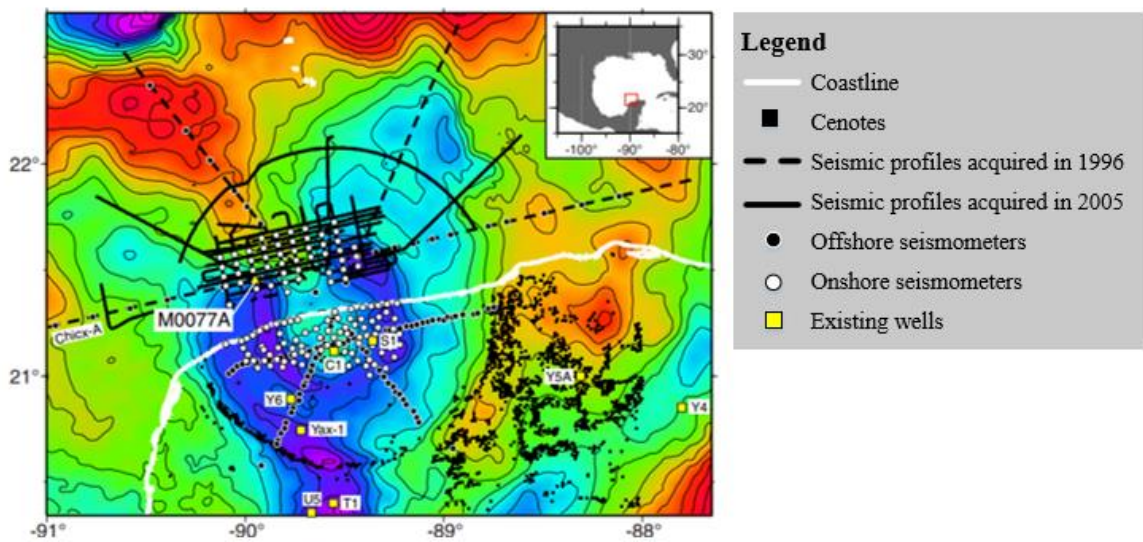


Figure 39. Locations of geophysical and drilling explorations performed at the site. Reprint from [79].

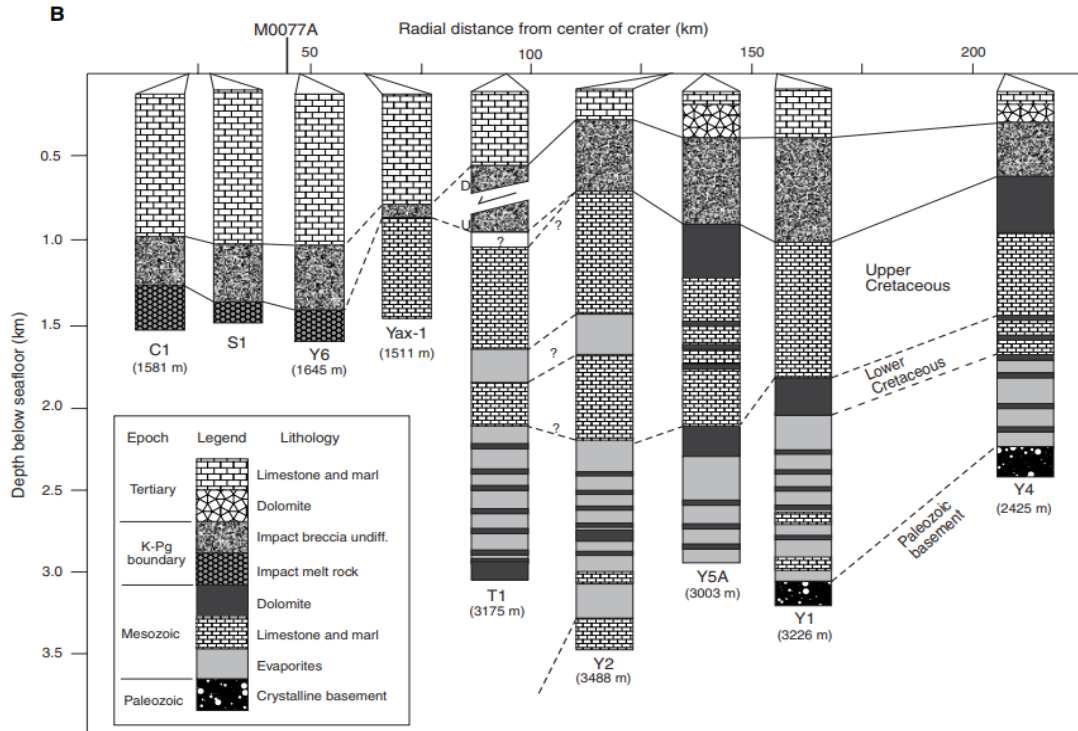


Figure 40. Lithostratigraphic correlation of boreholes from previous drilling programs. Reprint from [61].

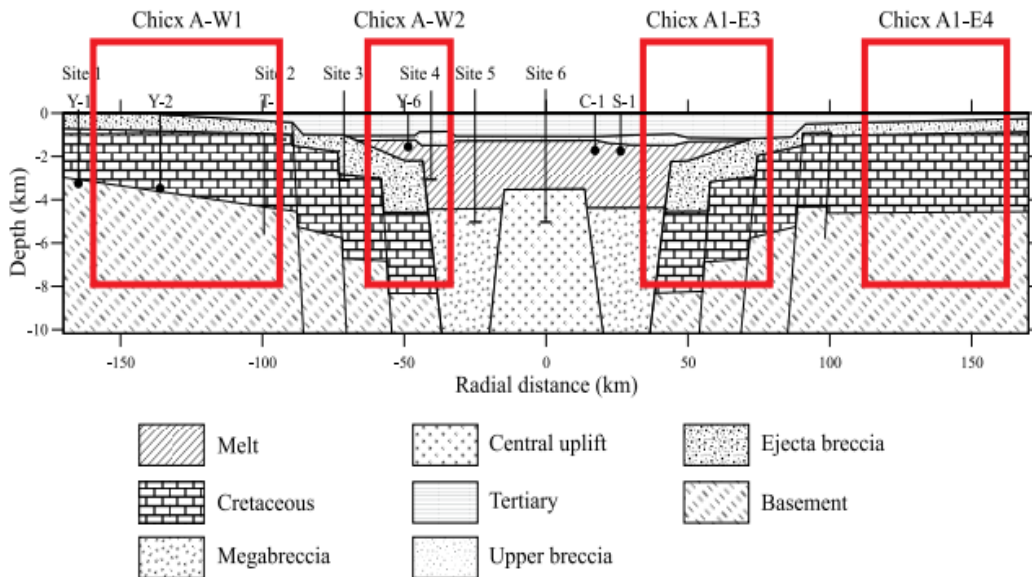


Figure 41. Schematic of Chicxulub crater with corresponding drilling locations. Reprint from [62].

### 5.3 Problem definition

The aim is to estimate the crater formation processes and the following geophysical effects, but most importantly, its likely variations, to better understand the after the impact effects. Previously, numerical models of crater formation were developed using different continuum dynamics hydrocode programs to quantify different aspects of the impact process with the assumption that the materials would behave like fluid at the time of impact. T. Takata first attempted to replicate the Chicxulub impact using the Smooth Particle Hydrodynamics (SPH) method [69]. B. Ivanov studied the degassing of sedimentary rocks due to Chicxulub impact using the Simplified Arbitrary Lagrangian Eulerian (SALE) code in 2D examining different asteroid sizes and velocities [70]. Elisabetta Pierazzo later simulated the impact event using 3D CHT hydrocode with varying impact angles [71]. Gareth Collins extensively modified the original SALE code to incorporate both viscoelastic and viscous rheologies to incorporate rock strength properties that was used by succeeding studies [72]. B. Ivanov presented comprehensive numerical simulation on largest craters found on Earth using updated 2D SALE hydrocode that showed good agreement with previous geological models [73]. Abramov and Kring presented the hydrothermal aspects of the Chicxulub impact addressing on the melting and cooling of the materials. Recent studies by Gareth Collins investigated on factors that contribute to the formation of terrace zone [74], peak ring formation [75], and the relationship between impact angle and structural crater asymmetries in iSALE3D [76]. Figure 42 to Figure 44 present numerical simulations of asteroid impact using the hydrocode from previous studies.

This work hypothesizes that the asteroid impact can be simplified and replicated using Particle Flow Code (PFC2D) program in two dimensions that follows discrete element method (DEM). In

particulate DEM model, particles are allowed to displace and rotate independently to each other and their interactions are controlled by assigning contact model [80]. A simplified DEM model of the asteroid impact is developed to resemble the Chicxulub impact conditions using geophysical data. The initial model only produces the impact mechanical responses for better computational efficiency.

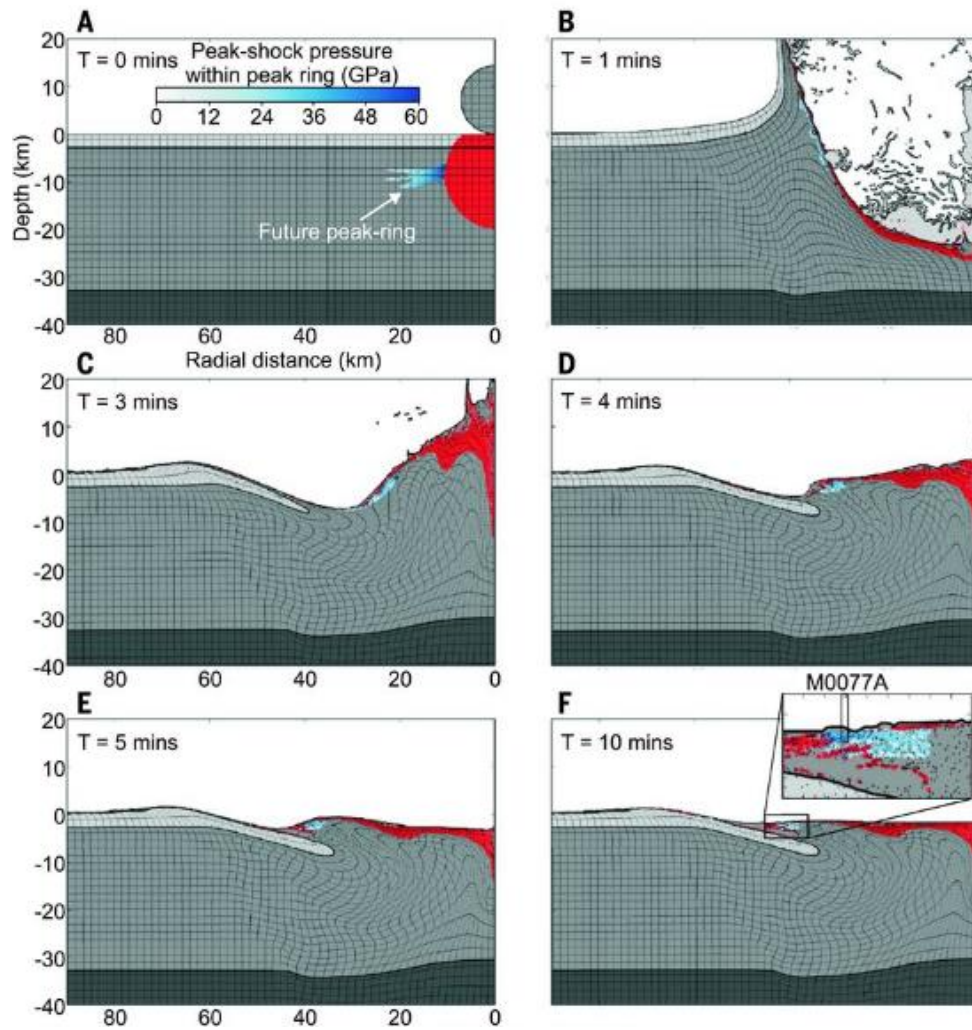


Figure 42. Numerical simulation of Chicxulub impact at different time instants with recorded of induced peak-shock pressure. Reprint from [81].

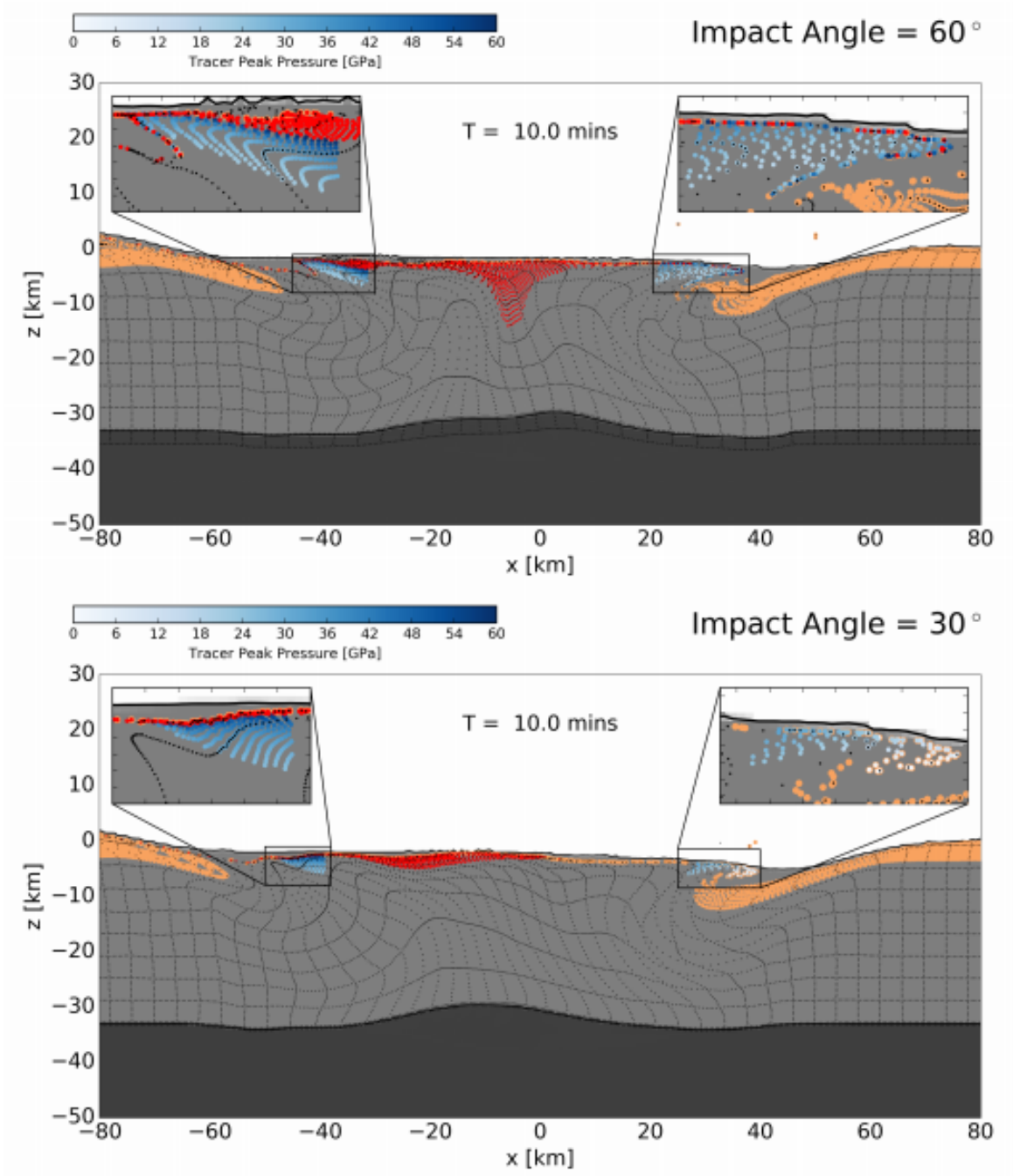


Figure 43. Final crater configuration for impact angle of 60 and 30 with impactor initial position on the top right. Reprint from [76].

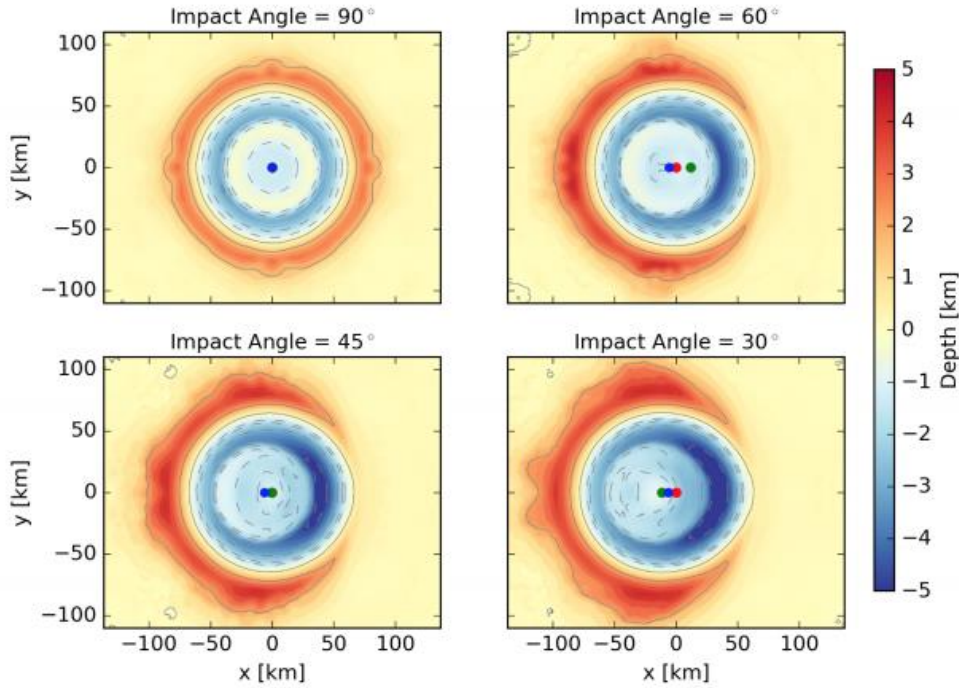


Figure 44. Surface topography produced by 3D iSALE hydrocode for impact direction from right to left. Reprint from [76].

#### 5.4 Methodology

Numerical simulations of the asteroid impact were performed based on the proposed experimental design. The scaling ratio of the whole system size is 1/100 to reduce computational cost in numerical simulations. To maintain energetic consistency in the scaling, the velocity of the asteroid is reduced 10 times to keep the kinetic energy reduction of 100 times. The experimental design chart for asteroid simulations is present in Figure 45. The model consists of three categories, asteroid conditions, surface conditions and boundary conditions. Asteroid conditions include the asteroid size, asteroid material properties, asteroid drop height, impact angle and asteroid velocity. Surface conditions include site stratigraphy and material properties. Boundary conditions include container dimensions, container properties and gravity. For the purpose of this study of assessing the effects of different impact conditions to the crater formation process, only impact angle and

asteroid velocity are subject to change while keeping other variables constant. Asteroid velocity varies from 1500 m/s to 2250 m/s with increment of 250 m/s. The choice of asteroid velocity is based on the estimation of the estimated Chicxulub asteroid's velocity, 15-22 km/s, after subjected to scaling down of 1/10 ratio to maintain equal reduction ratio of 1/100 of the kinetic energy to the whole scaled down system. The impact angle also changes from 90<sup>0</sup> to 60<sup>0</sup>, 45<sup>0</sup>, and 30<sup>0</sup>. Detailed description of the model is presented in the next section.

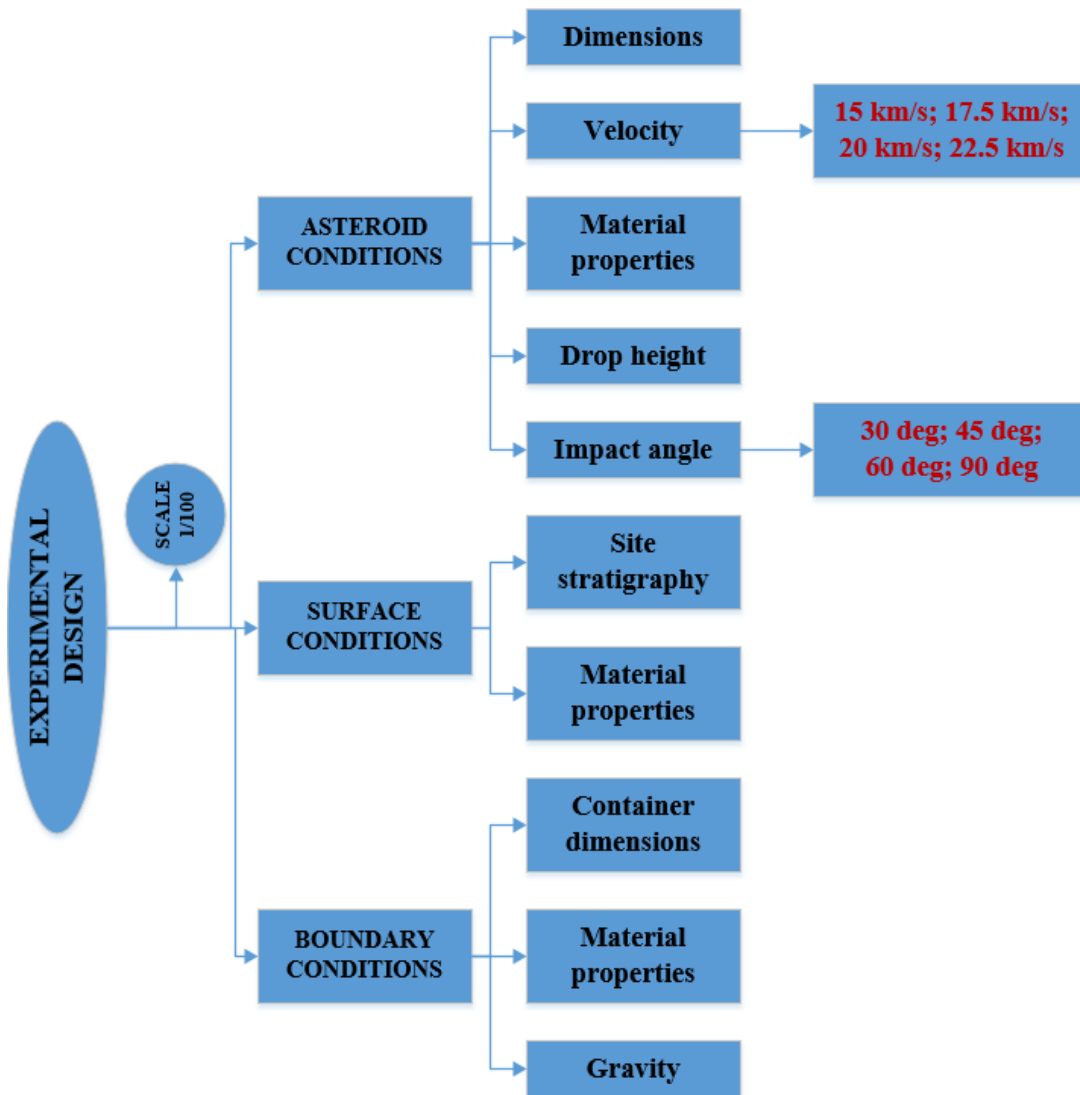


Figure 45. Schematic graph of the model experimental design.

## 5.5 DEM model of asteroid impact

The DEM model impact configuration is shown in Figure 46 with different impact velocities ( $v$ ) and impact angles ( $\beta$ ). The scaled down asteroid diameter is 100 m consisting of bonded particles of 10 m diameter. For all case studies, the vertical drop height of the asteroid remains constant of 500 m above the ground surface. The model is built with several assumptions. The first assumption is that material density is constant of  $3,000 \text{ kg/m}^3$  for both the ground and asteroid materials. Secondly, there are 9 different layers in the ground condition and the particle sizes increase from 5 m to 40 m in diameter from the surface to the container baseline corresponding to the ground layer. List of layer depth and its particle size is provided in Table 9. The increase in particle size is aim to reduce computational cost as well as to reflect the physical aspect of basement rocks and mantle layers. The first three layers have properties of weak sedimentary limestone while the rest will have properties of hard granite rocks. The layer configuration is obtained by sedimentary process under gravity. The asteroid will have similar properties with the sedimentary limestone. The container size is 4 km by 2 km after down scaling. The Earth's gravitational force of  $9.81 \text{ m/s}^2$  is applied throughout the simulation.

### 5.5.1 Contact model

Linear parallel bond contact model is used to resemble the rock mechanic behaviors. The use of the bonded-particle models in rock mechanics studies has been popular practice according to Potyondy's study [82]. According to the PFC manual [80], the parallel bond provides the mechanical behavior of a cement-like material gluing two particles of same material together. The bond component acts like a set of elastic springs with constant normal and shear stiffness evenly

distributing force and moment across the contact plane. As the stresses applying on the particles exceed the bond strength, the contact bond breaks and is removed from the model. The contact model then becomes the simple linear contact model [80]. Figure 47 shows the components of the linear parallel contact bond model. Full description of the linear parallel bond contact model can be found in the PFC user manual. The values of limestone parameters are adopted from Ledgerwood's study on high rock pressure conditions [83]. The model parameters used in this study are calibrated and the calibration results show agreement with the reference. The contact model parameters used in the simulations are listed in Table 10.

### 5.5.2 Boundary condition

Infinite boundary condition is set up in the model by assigning the wall component's normal and shear damping ratio of 1.0, which means all the energy of the particles is absorbed when they are in contact with the walls. To validate the absorbing aspect of the boundary, simple test is set up where one ball comes into contact with a chain of five balls placed at the corner of the chamber and the velocities of the first and the last ball of the chain are recorded and shown in Figure 48. The velocity of the ball at the corner quickly converts to zero after the impact. Thus, the energy-force reflection effect due to boundary is minimized.

### 5.5.3 Measurement spheres

Measurement spheres are located along the center line of the impact field and next to the chamber boundaries to obtain quantities such as horizontal and lateral stresses, porosity and coordinate number (average inter-particle contacts per particle). The radiuses of the measurement spheres

along the center line and the boundaries are 150 m and 20 m respectively. Figure 49 shows the locations of the measurement spheres.

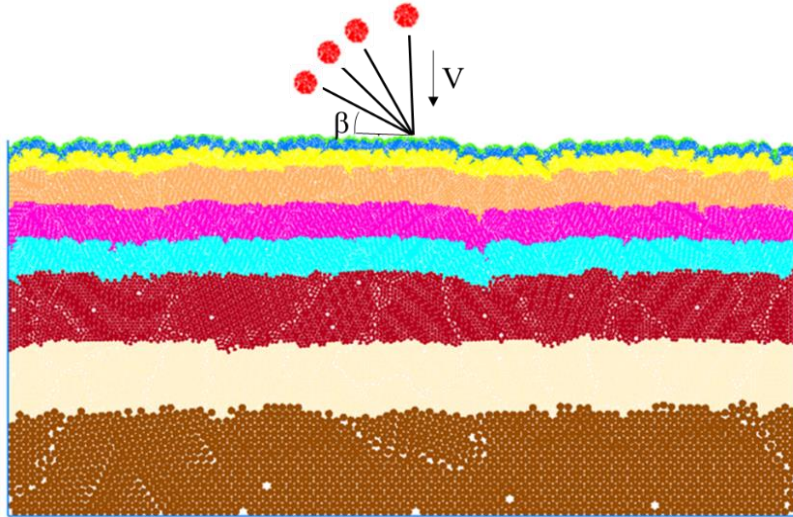


Figure 46. Asteroid impact model configuration.

Table 9. Layer configuration and its particles dimension used in the impact model.

Layer	Material	Layer depth	Particle radius
		(m)	(m)
1	Sedimentary limestone	10	5
2		30	5
3	Rock basement	90	5
4		180	10
5		180	10
6		180	10
7		360	20
8		360	20
9		610	40

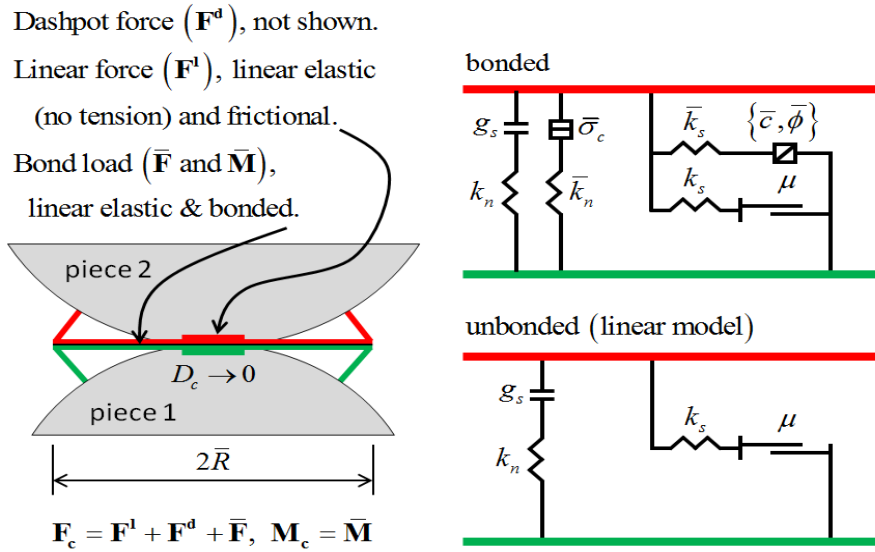


Figure 47. Components of linear parallel contact bond model. Reprint from [80].

Table 10. Contact model properties used in DEM impact simulations.

Name	Contact type	Particle normal stiffness	Particle shear stiffness	Friction coefficient	Bond normal stiffness	Bond shear stiffness	Bond tension (N)	Bond cohesion (N)
		(Pa)	(Pa)		(Pa)	(Pa)		
Asteroid	Linear parallel bond	4.0e9	1.6e9	0.3	4.0e9	1.6e9	4.0e6	4.0e6
Sedimentary limestone	Linear parallel bond	4.0e9	1.6e9	0.3	4.0e9	1.6e9	4.0e6	4.0e6
Rock basement	Linear parallel bond	40.0e9	16.0e9	0.3	40.0e9	16.0e9	40.0e6	40.0e6
Walls	Linear contact	5.0e10	5.0e10	0	-	-	-	-

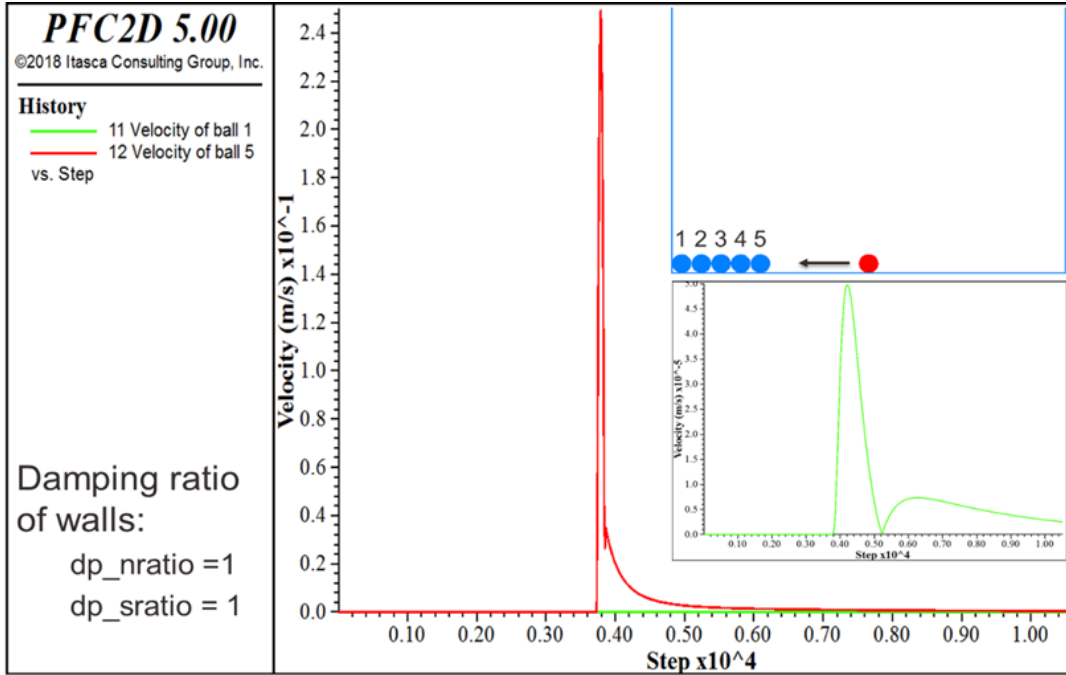


Figure 48. Verification of infinite boundary condition.

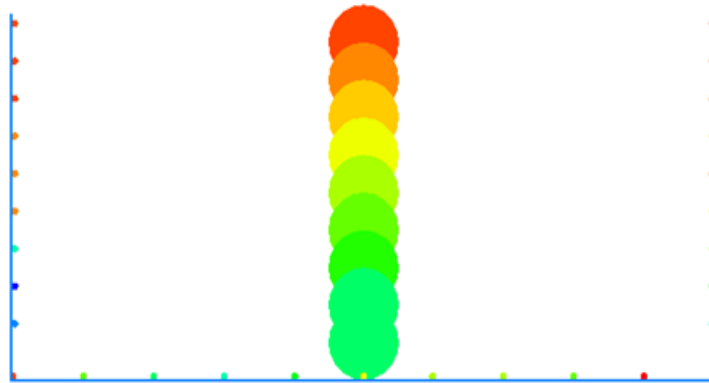


Figure 49. Measurement spheres locations.

## 5.6 Simulation results

Numerical simulations of asteroid impact are performed based on the proposed experimental design with varying impact angle and asteroid velocity. Each simulation is run until the surface

particles' velocity is less than 1 m/s or completing 2 million calculation cycles. Preliminary results of asteroid impact simulations are analyzed and presented below.

### 5.6.1 Final crater and surface topography

Final crater configuration for each impact conditions is presented in Figure 50-53. It is observed that the asteroid velocity plays essential roles on the formation of the crater. The uplifting effect is more visible as the asteroid velocity increases. The shearing effect in the rock layers due to different impact angles also depends on asteroid velocity. The terrace zone and crater rim effects are also observed from the finale crater configuration. The distribution of deeper rock particles (pink layer) flying out after impact concentrates on the surface layer on the same side with the asteroid's initial locations. This effect is more noticeable for the case of smaller impact angles with high impact velocities. Surface topography of each impact case is compared with the real Chicxulub crater surface topography based on the geophysics and drilling explorations presented in Salguero-Hernandez's study [62]. Figure 54 to 57 shows the surface configurations of the model for each impact angle comparing with the real surface configuration. The crater diameter for small impact angle of  $30^{\circ}$  significantly increase relatively with the asteroid velocity. The rise of crater rims is also higher for non-vertical impacts. In term of surface matching with the actual crater dimensions, the simulations of impact angle of  $90^{\circ}$  yield better outcomes than other impact angles. The DEM results suggest that the oblique impacts provide more uplift in the transient crater rim in the uprange direction (same side with the asteroid position) than in the downrange direction which pose the opposite result to the previous study by G. Collin [77]. The contradiction might be caused by the difference in modeling method between DEM and hydrocode. Further investigation on the DEM and hydrocode simulation differences should be carried out in future study.

### 5.6.2 Velocity fields

The velocity fields are obtained throughout the impact and crater formation. However, the main interest is to see how the impact induced velocity travels through the surface instantly after impact. Figure 58 to Figure 65 show the velocity of particles in the ground captured at 5,000; 10,000; 15,000; 20,000; 40,000; and 80,000 calculation cycles; which is equivalent to 1 second; 2 seconds; 3 seconds; 4 seconds; 8 seconds; and 16 seconds after impact by taking the average timestep of  $2.0 \times 10^{-4}$  s/calculation cycle.

### 5.6.3 Horizontal and vertical stresses

The stresses in both horizontal and vertical directions are recorded at different depths along the centerline of the field and around the boundary walls using measurement spheres (Figure 49). Sequences of stress variation during the simulation are shown in Figure 66 to Figure 75. Since peak stresses are the main concern in this study, the largest horizontal and vertical stresses correspond to each measurement sphere's vertical location are collected for each impact condition. Figure 12 to Figure 13 compare the maximum stress experienced for the cases of different asteroid velocities and similar impact angle. It is observed that the vertical stresses are always larger than the horizontal stresses. The highest stresses are mostly seen at the depth of 40 km below the ground surface, varying around 30 GPa for vertical direction and around 20 GPa for horizontal direction. The effect of changing impact velocity is noticeable for  $90^\circ$  impacts while there is hardly any difference in maximum vertical stresses for smaller angular impacts. In horizontal direction, the variation in velocity shows better difference in maximum stress, especially after 60 km depth. For the first 40 km depth, there is no clear effect of velocity to the recorded stresses. On the other way,

Figure 76 to Figure 83 compare the maximum stress experienced for the cases of different impact angles and similar asteroid velocity. In general, maximum stresses decrease as the impact angle decreases. This might be due to the locations of the measurement spheres being at the centerline whereas the center of impact might shift to the right for impact angles less than  $90^{\circ}$ . When comparing with the maximum pressure of approximately 60 GPa generated by hydrocode simulations, the DEM simulation results seem underestimating the impact effects. However, this DEM model purely provides mechanistic responses without coupling with fluid and thermal aspects which might contribute to the remaining induced energy/pressure at impact.

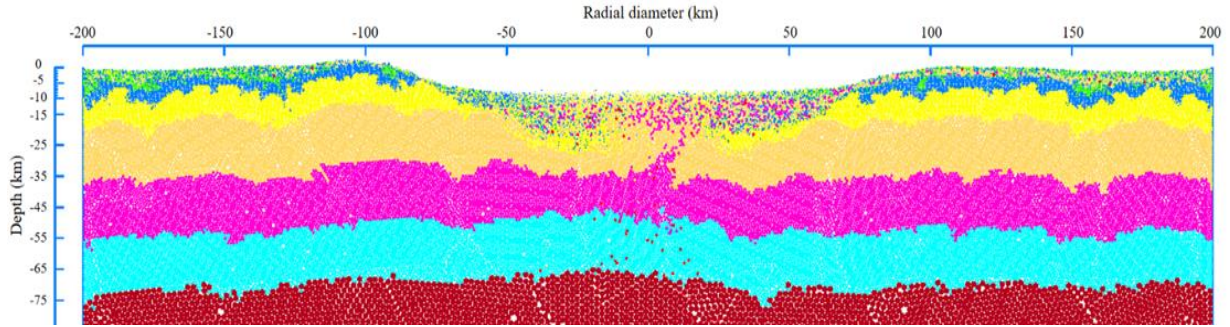
#### 5.6.4 Contact force chains

The map of contact force chains are obtained for both linear contact model and linear parallel bond contact model. Figure 84 shows the changes in the force chains before and after the impact for the case of  $90^{\circ}$  impact angle with asteroid velocity of 15 km/s. It is seen that after the blast, the particles reconnect and create series vertical contact chains which can be interpreted as the formation of vertical rock bedding within the terrace zones. However, this effect is hardly observed in cases of other impact angles.

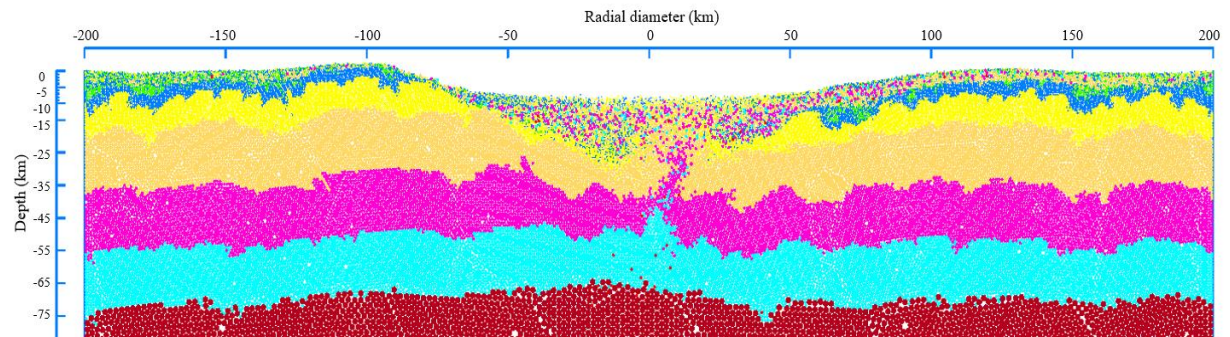
#### 5.7 Discussion

This study provides quantitative numerical assessment of asteroid impact using PFC2D. Different impact scenarios are generated by varying asteroid velocity and impact angles. The simulation results are analyzed and compared in term of final crater configuration, surface topography, velocity field, maximum stresses experienced, and contact force chains. It is showed that the uplifting effect is governed by the impact velocity while the shearing effect is caused by impact

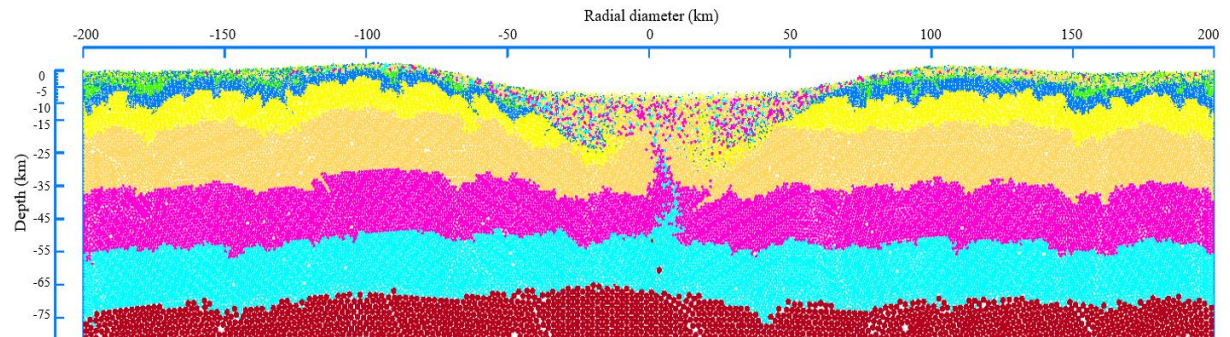
angles. Also, the final crater configuration suggests that the oblique impacts produce more uplift effects at the crater rims on the uprange direction and more excavation on the downrange direction. Although only mechanistic response is obtained from the preliminary model, the results provide adequate estimation of the stresses generated at the impact as well as replicating the crater formation process. Further development of the model, including fluid and thermal couplings, is expected to yield more accurate result of impact simulations.



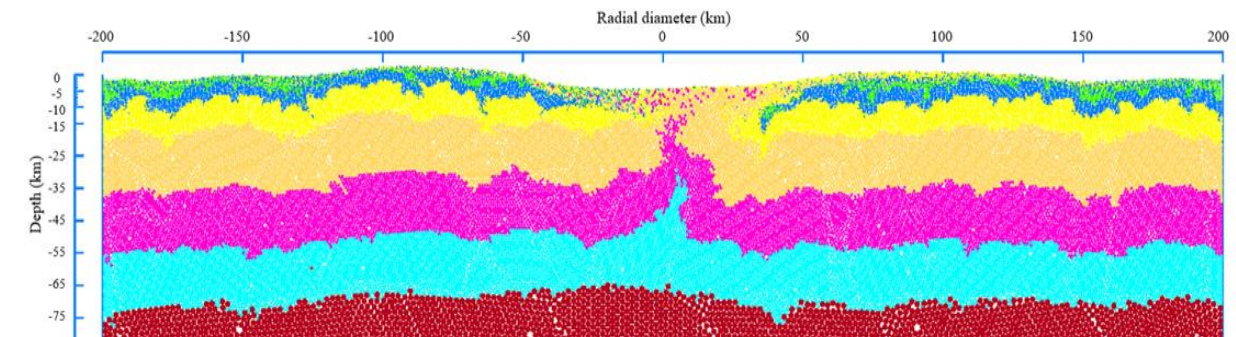
(a) Asteroid velocity 15 km/s, impact angle  $90^0$



(b) Asteroid velocity 17.5 km/s, impact angle  $90^0$

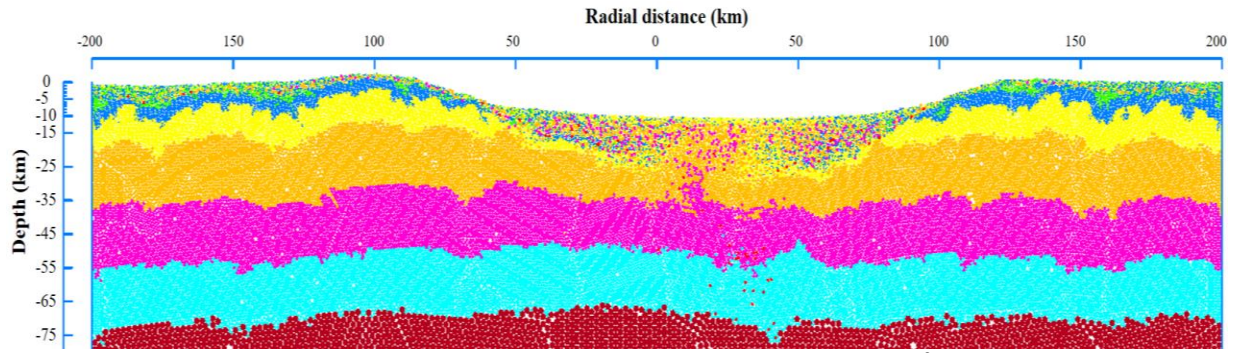


(c) Asteroid velocity 20 km/s, impact angle  $90^0$

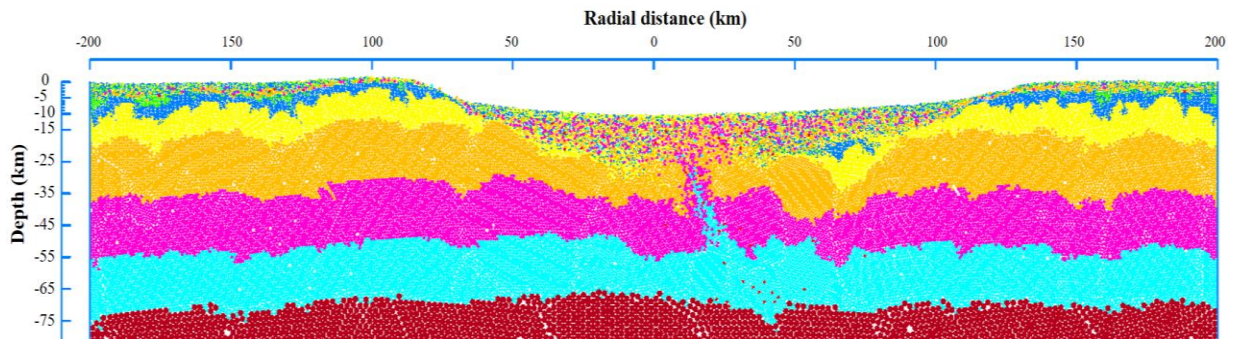


(d) Asteroid velocity 22.5 km/s, impact angle  $90^0$

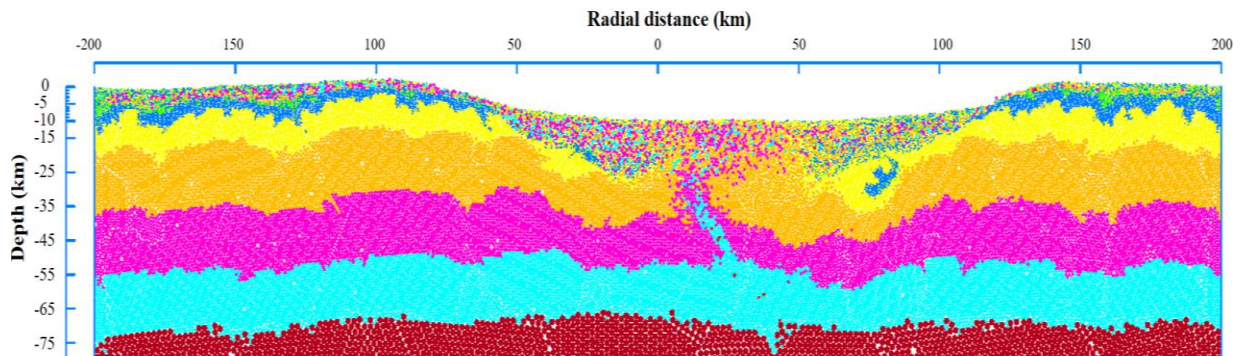
Figure 50. Final craters corresponding to different asteroid velocity with  $90^0$  impact angle.



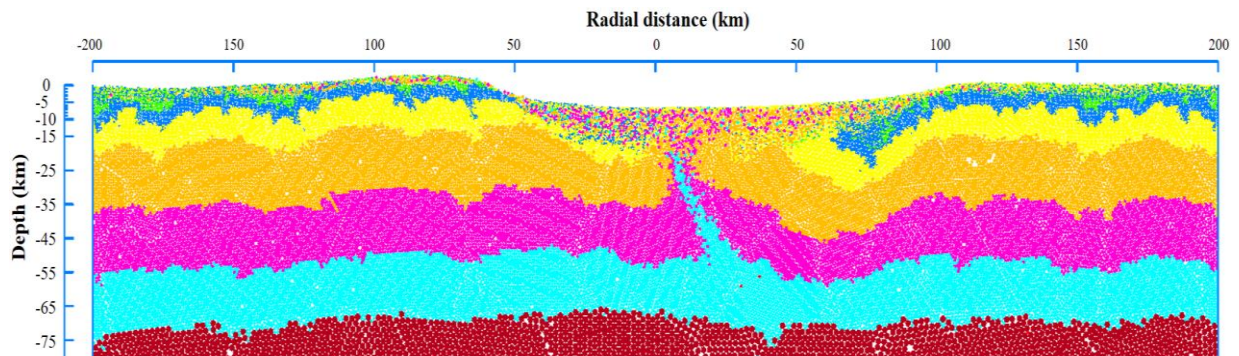
(a) Asteroid velocity 15 km/s, impact angle  $60^{\circ}$



(b) Asteroid velocity 17.5 km/s, impact angle  $60^{\circ}$

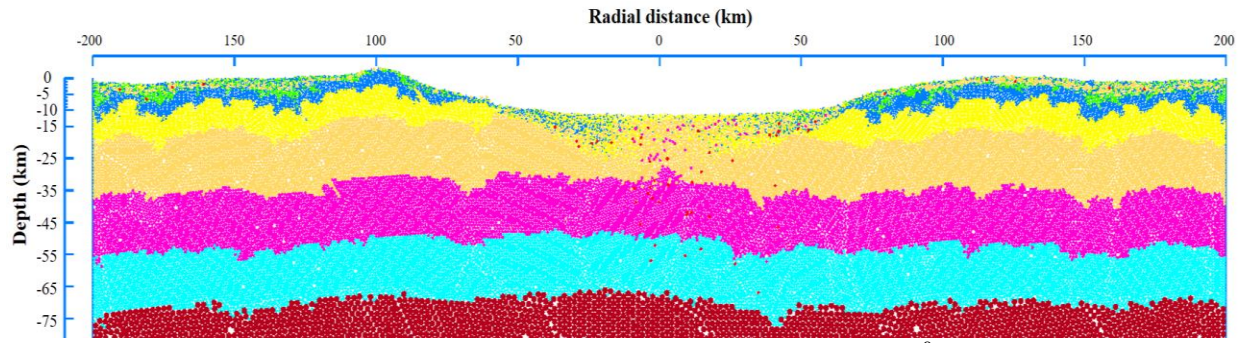


(c) Asteroid velocity 20 km/s, impact angle  $60^{\circ}$

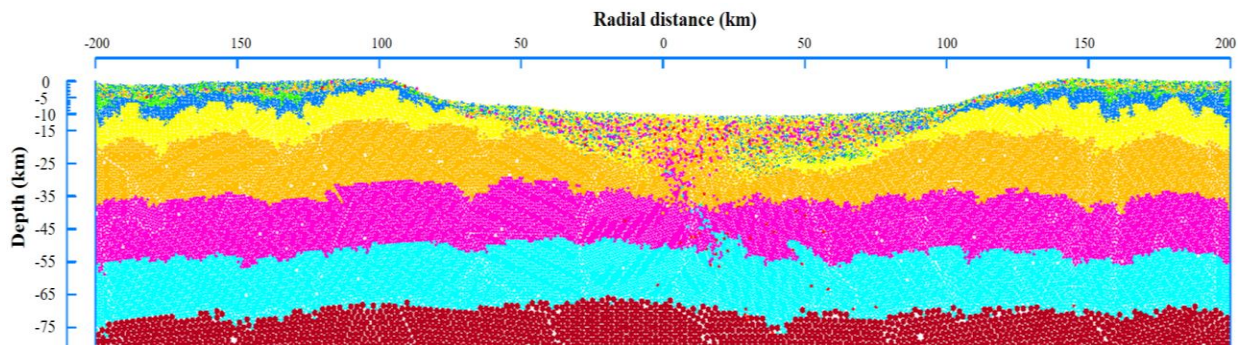


(d) Asteroid velocity 22.5 km/s, impact angle  $60^{\circ}$

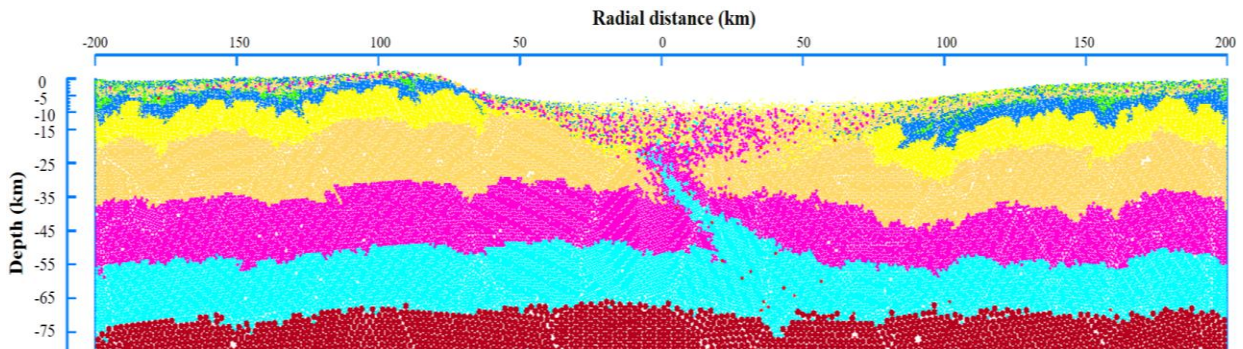
Figure 51. Final craters corresponding to different asteroid velocity with  $60^{\circ}$  impact angle.



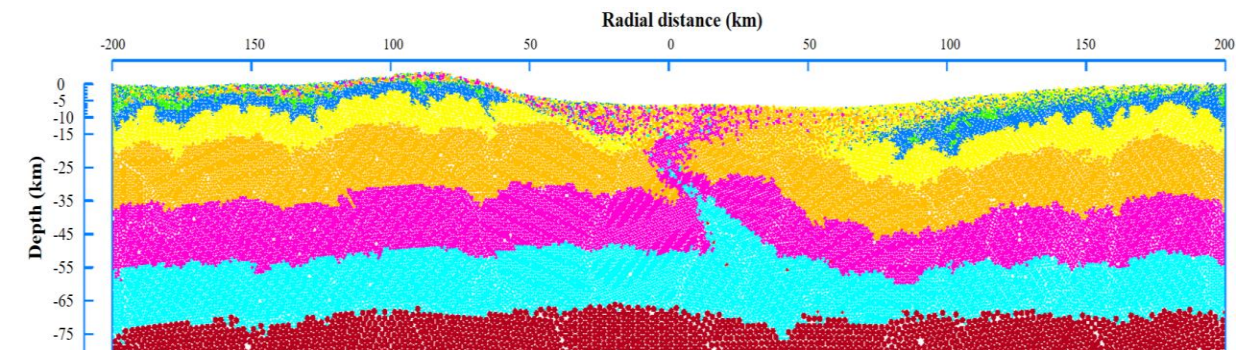
(a) Asteroid velocity 15 km/s, impact angle  $45^{\circ}$



(b) Asteroid velocity 17.5 km/s, impact angle  $45^{\circ}$

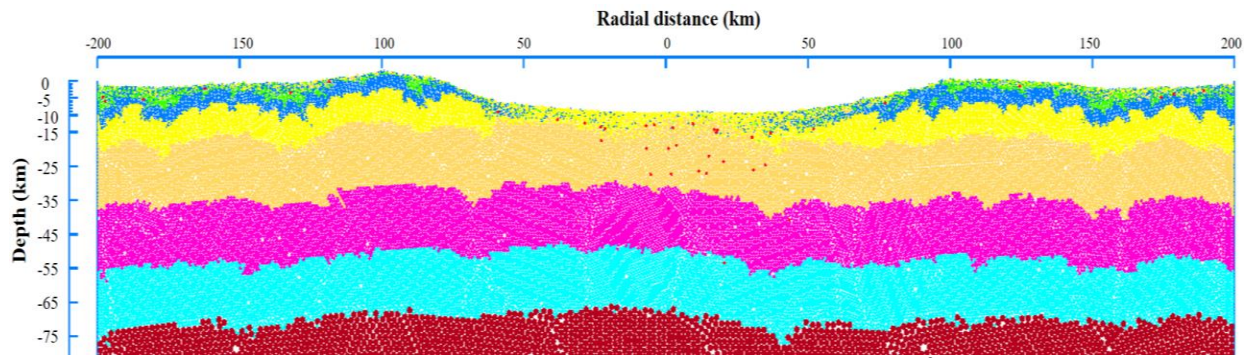


(c) Asteroid velocity 20 km/s, impact angle  $45^{\circ}$

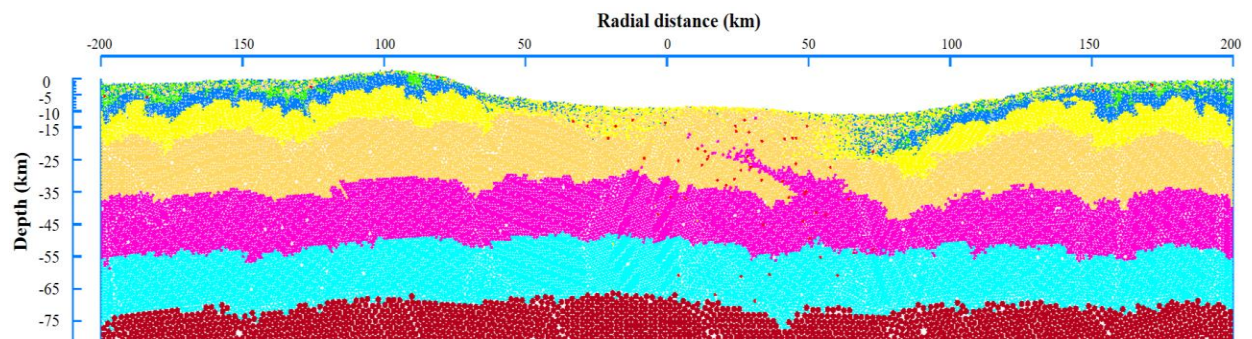


(d) Asteroid velocity 22.5 km/s, impact angle  $45^{\circ}$

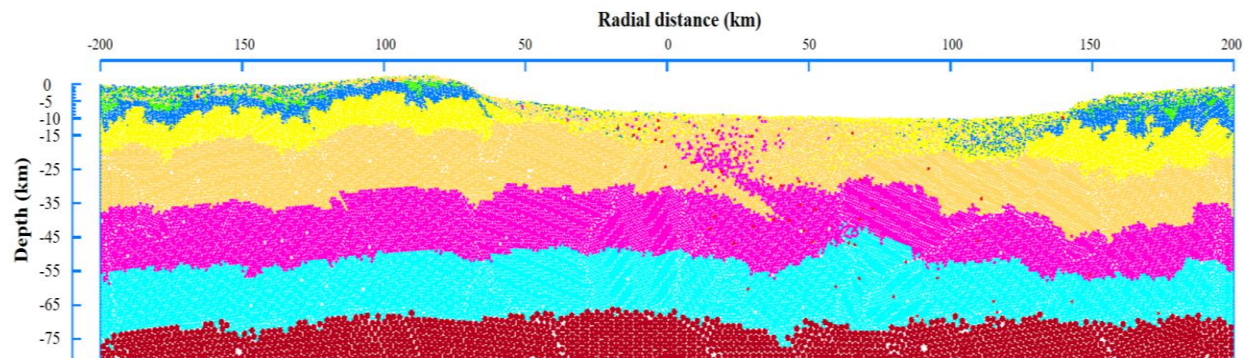
Figure 52. Final craters corresponding to different asteroid velocity with  $45^{\circ}$  impact angle.



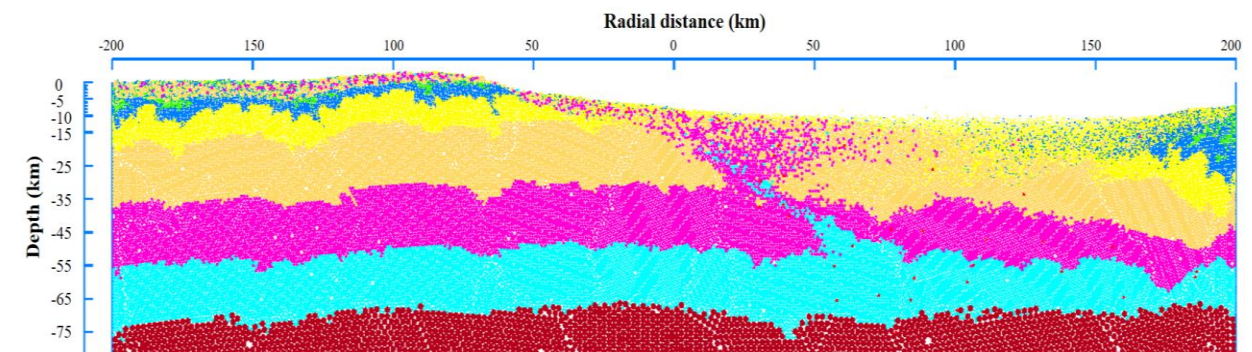
(a) Asteroid velocity 15 km/s, impact angle  $30^{\circ}$



(b) Asteroid velocity 17.5 km/s, impact angle  $30^{\circ}$



(c) Asteroid velocity 20 km/s, impact angle  $30^{\circ}$



(d) Asteroid velocity 22.5 km/s, impact angle  $30^{\circ}$

Figure 53. Final craters corresponding to different asteroid velocity with  $30^{\circ}$  impact angle.

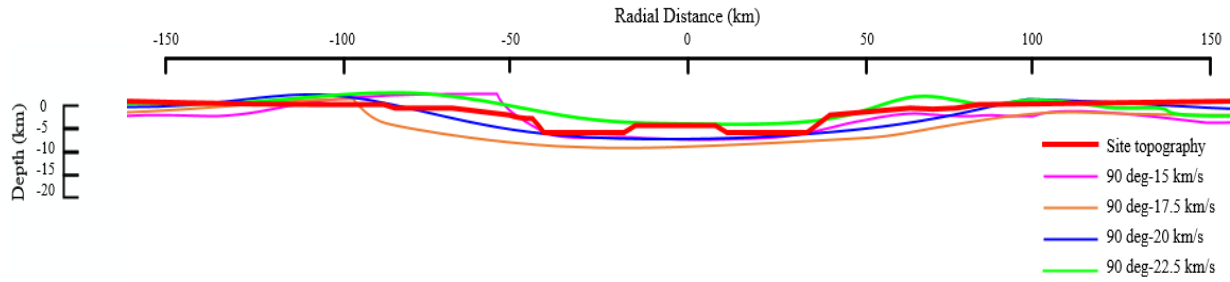


Figure 54. Crater topographies for 90<sup>0</sup> impact angle.

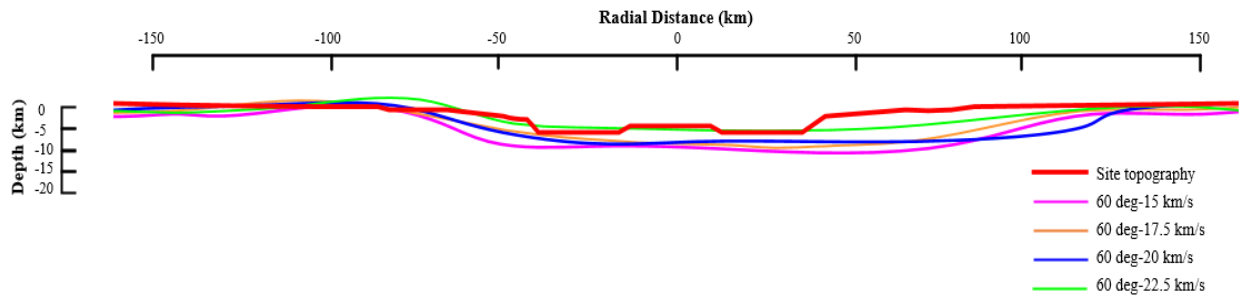


Figure 55. Crater topographies for 60<sup>0</sup> impact angle.

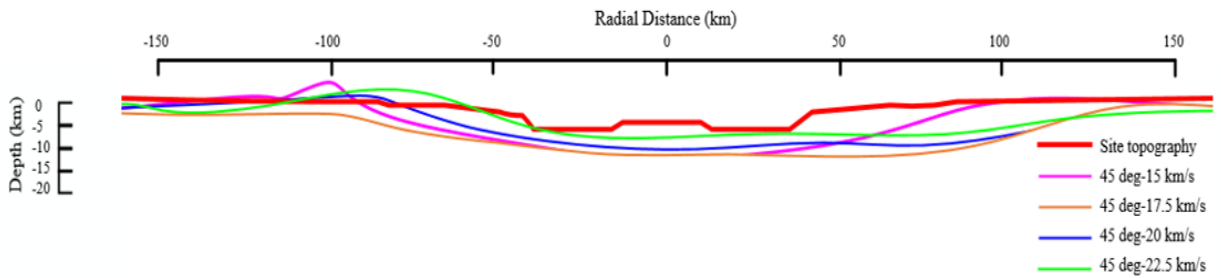


Figure 56. Crater topographies for 45<sup>0</sup> impact angle.

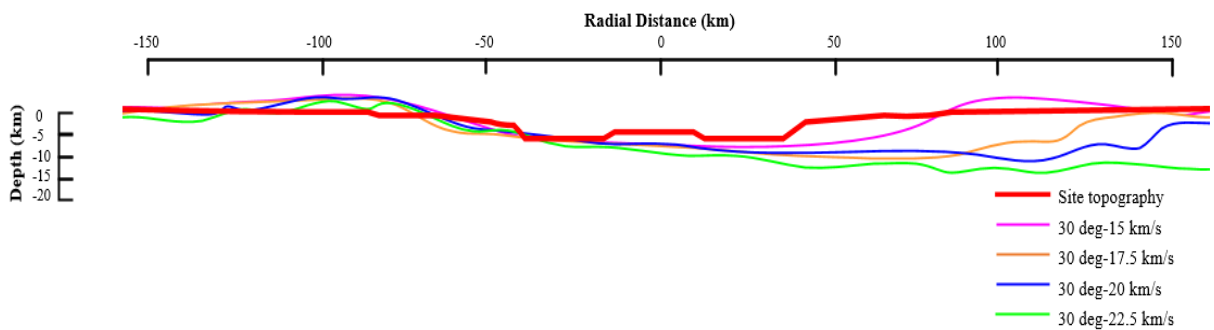
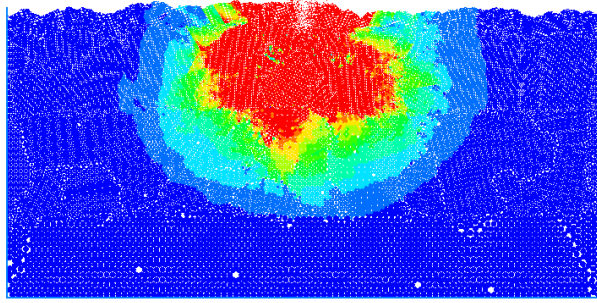
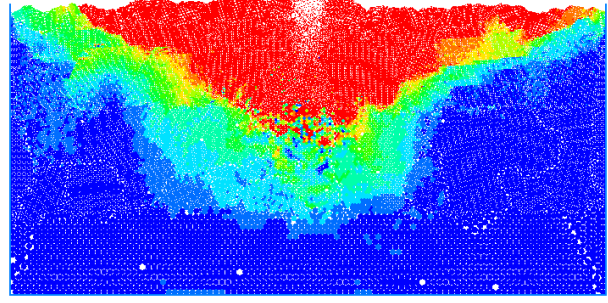


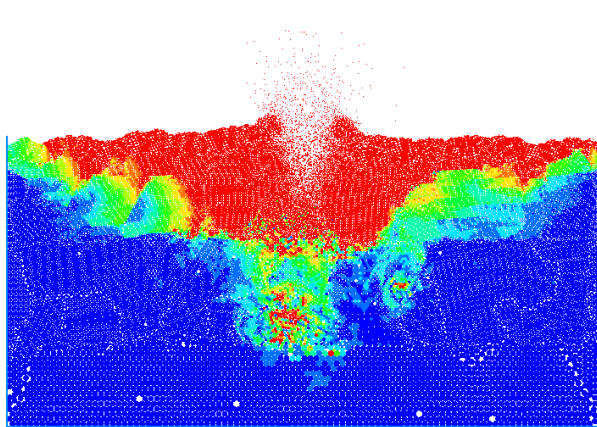
Figure 57. Crater topographies for 30<sup>0</sup> impact angle.



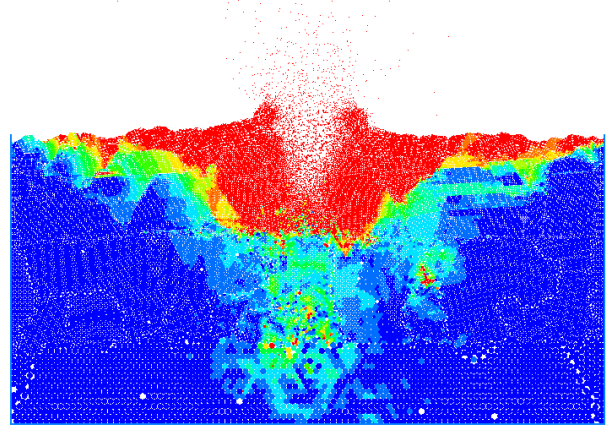
(a) 5,000 calculation cycles



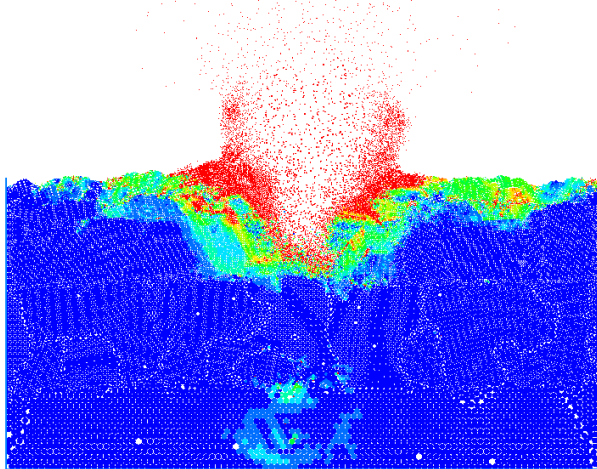
(b) 10,000 calculation cycles



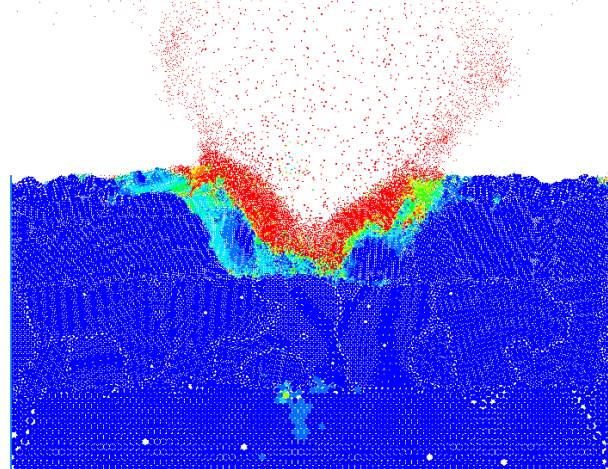
(c) 15,000 calculation cycles



(d) 20,000 calculation cycles



(e) 40,000 calculation cycles



(f) 80,000 calculation cycles

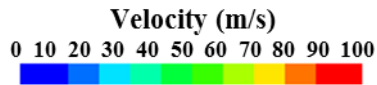
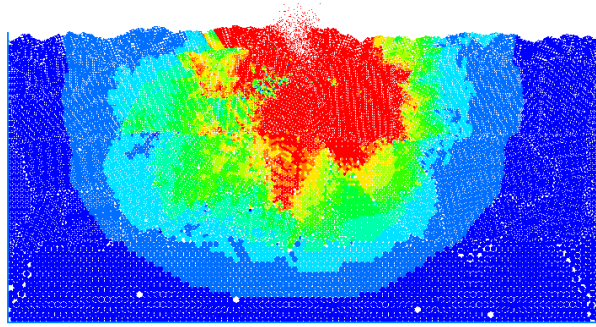
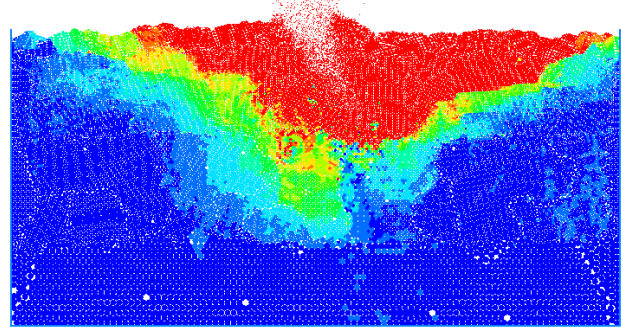


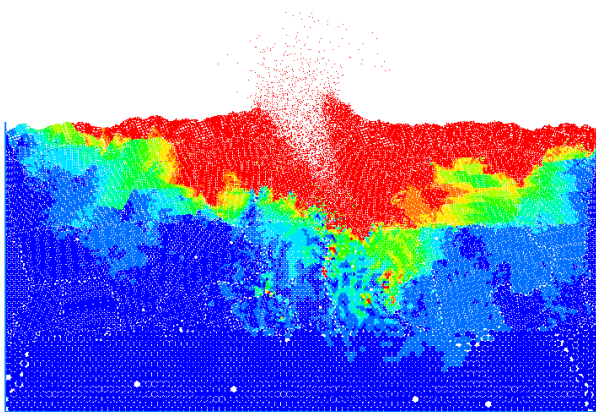
Figure 58. Velocity field variation right after impact at  $90^\circ$  and asteroid velocity of 15 km/s.



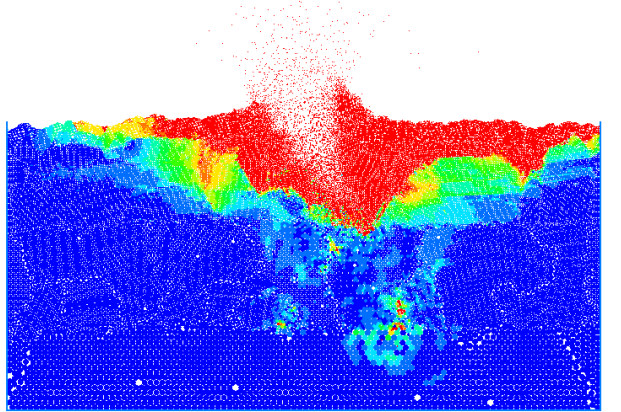
(a) 5,000 calculation cycles



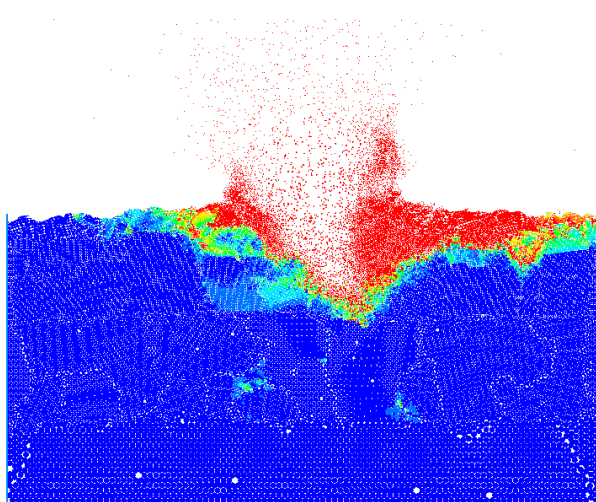
(b) 10,000 calculation cycles



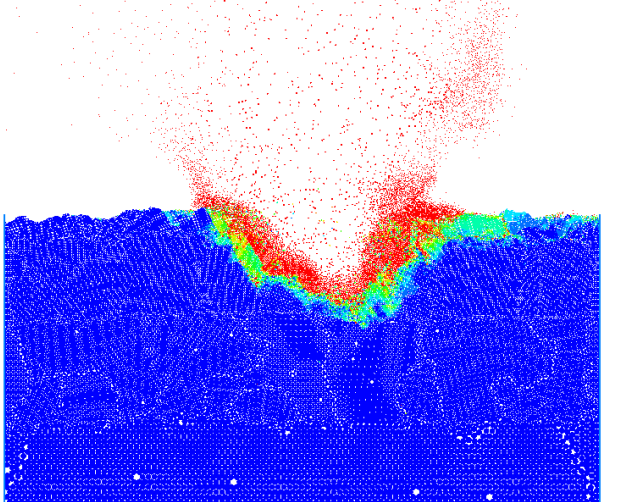
(c) 15,000 calculation cycles



(d) 20,000 calculation cycles



(e) 40,000 calculation cycles



(f) 80,000 calculation cycles

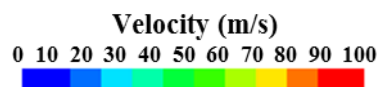
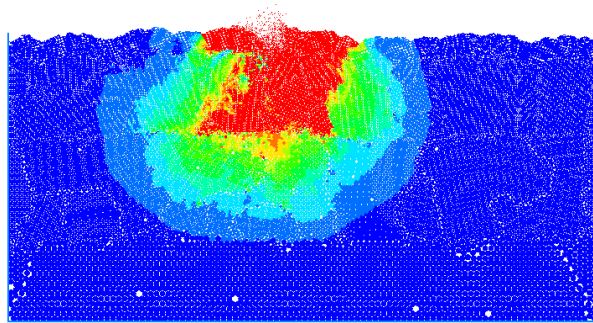
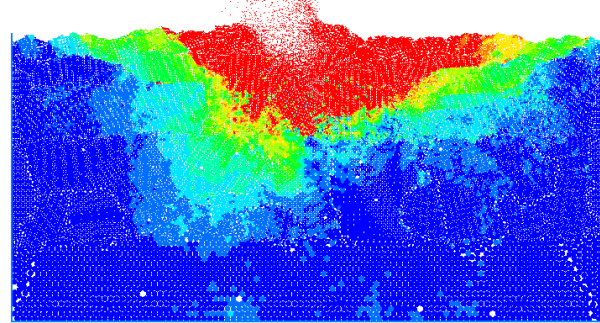


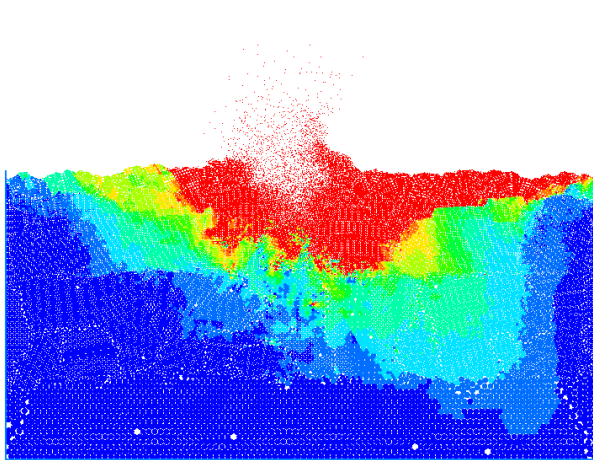
Figure 59. Velocity field variation right after impact at  $60^\circ$  and asteroid velocity of 15 km/s.



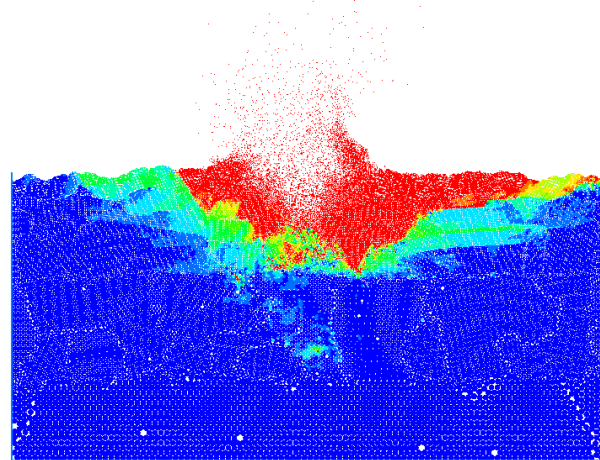
(a) 5,000 calculation cycles



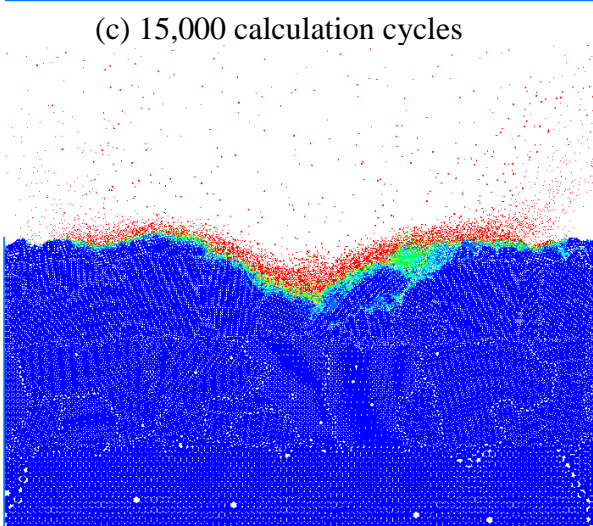
(b) 10,000 calculation cycles



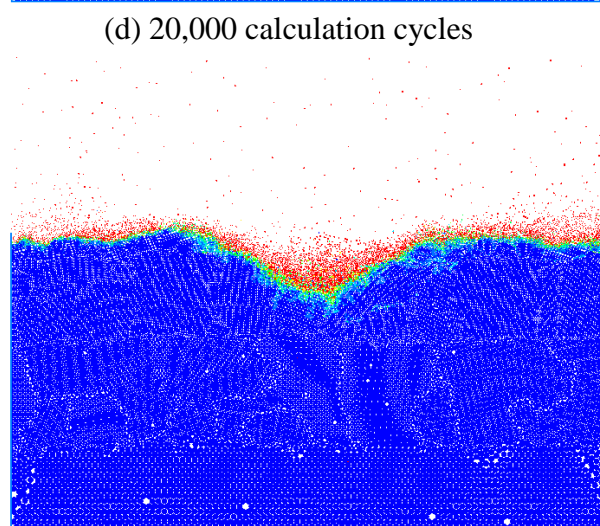
(c) 15,000 calculation cycles



(d) 20,000 calculation cycles



(e) 40,000 calculation cycles



(f) 80,000 calculation cycles

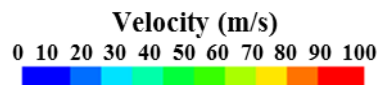
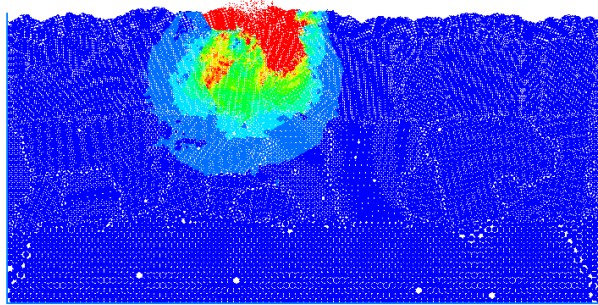
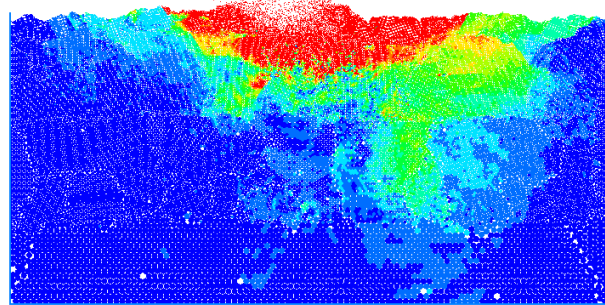


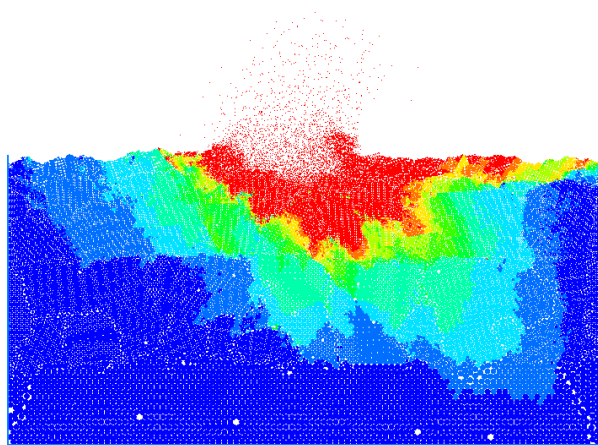
Figure 60. Velocity field variation right after impact at  $45^\circ$  and asteroid velocity of 15 km/s.



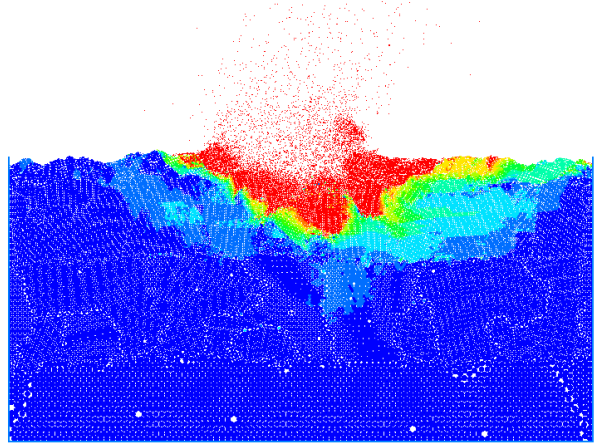
(a) 5,000 calculation cycles



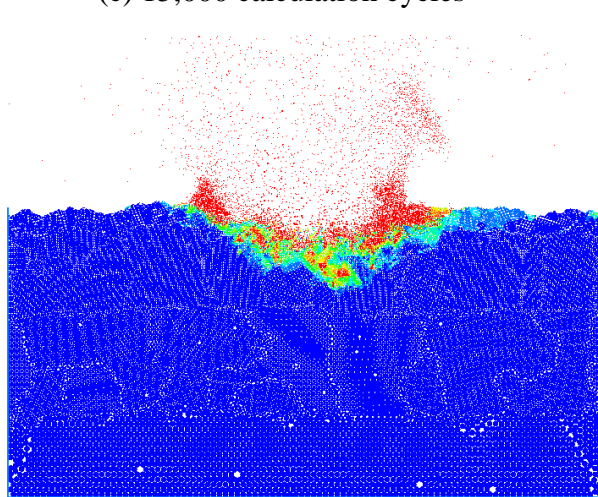
(b) 10,000 calculation cycles



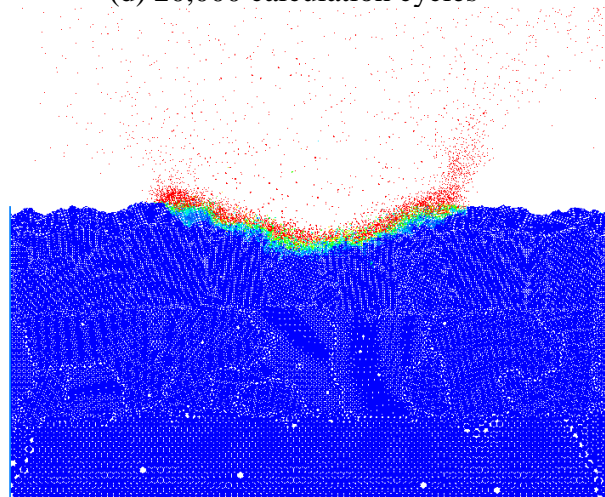
(c) 15,000 calculation cycles



(d) 20,000 calculation cycles



(e) 40,000 calculation cycles



(f) 80,000 calculation cycles

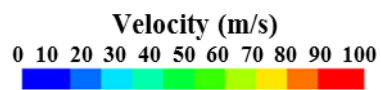


Figure 61. Velocity field variation right after impact at  $30^\circ$  and asteroid velocity of 15 km/s.

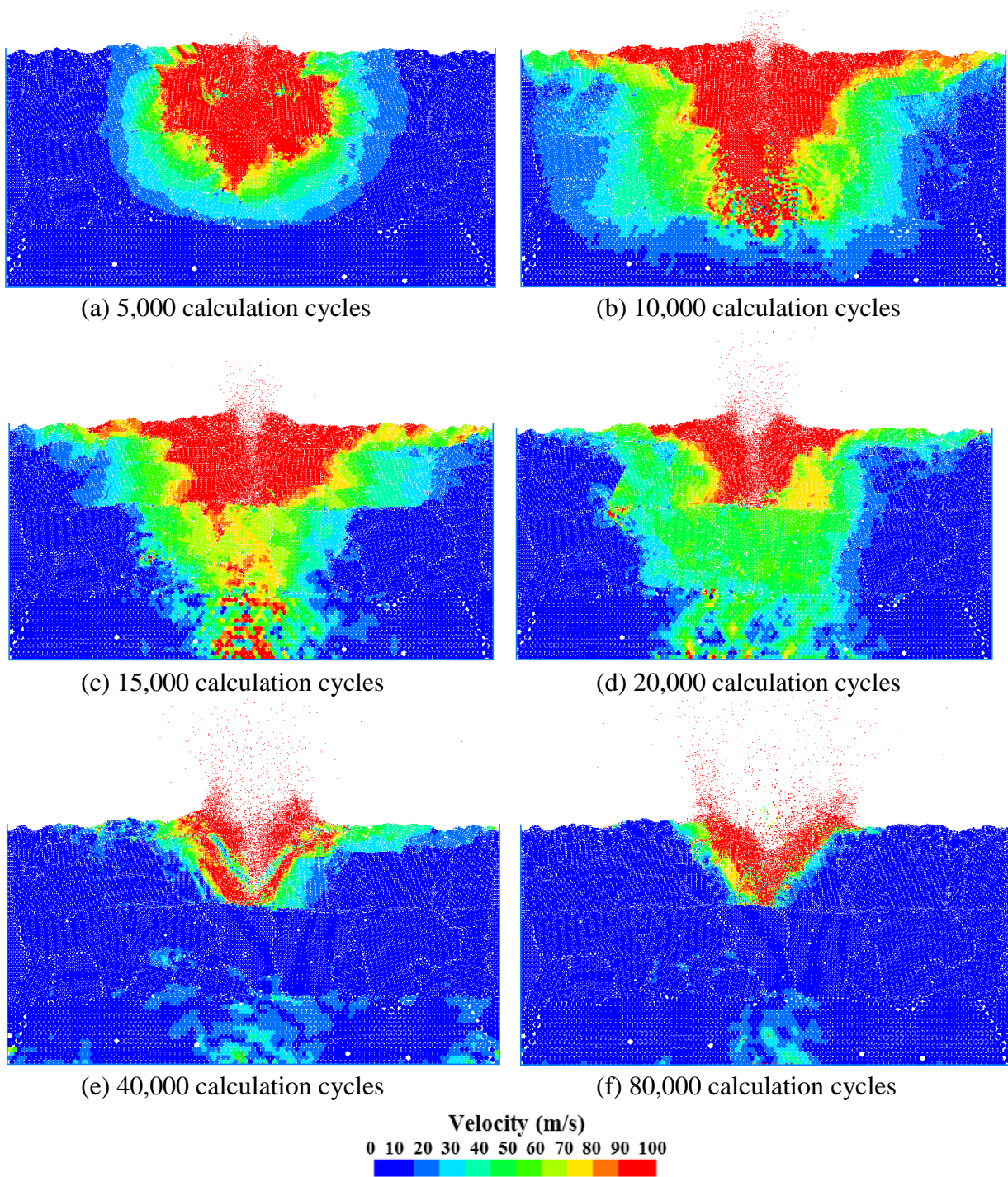
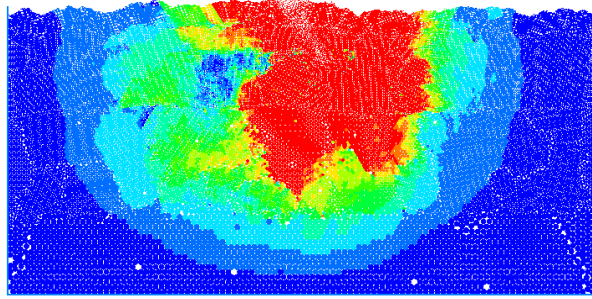
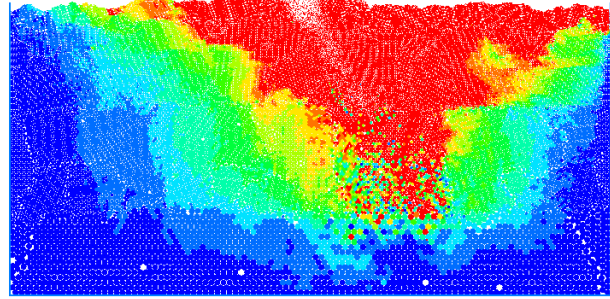


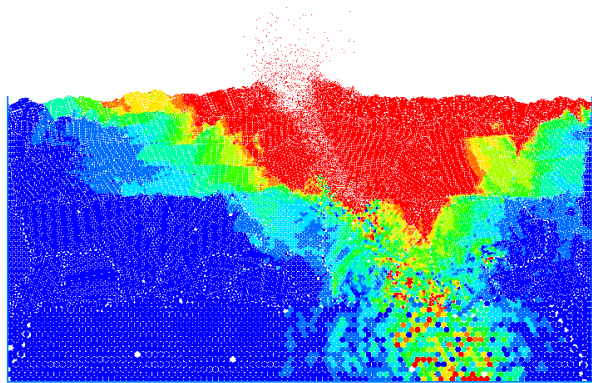
Figure 62. Velocity field variation right after impact at  $90^\circ$  and asteroid velocity of 22.5 km/s.



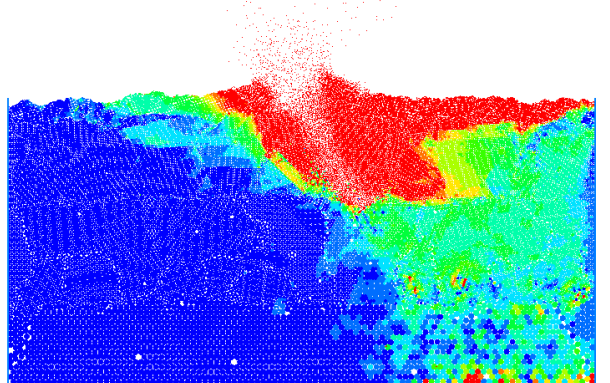
(a) 5,000 calculation cycles



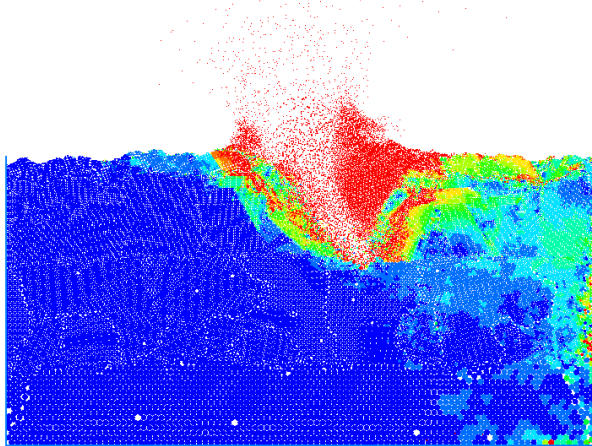
(b) 10,000 calculation cycles



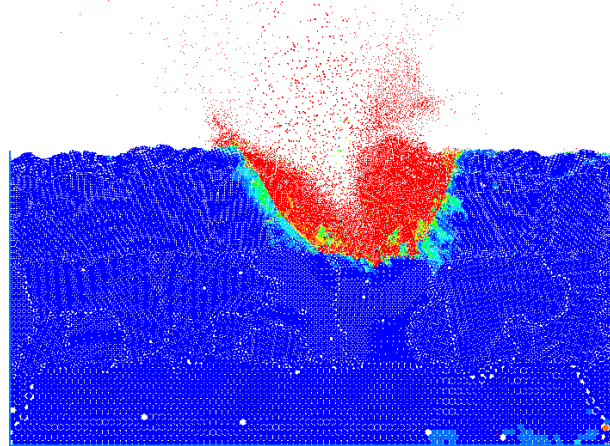
(c) 15,000 calculation cycles



(d) 20,000 calculation cycles



(e) 40,000 calculation cycles



(f) 80,000 calculation cycles

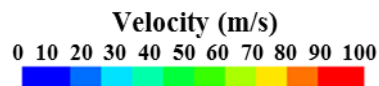
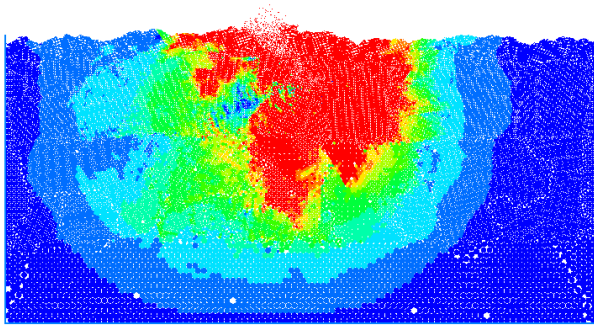
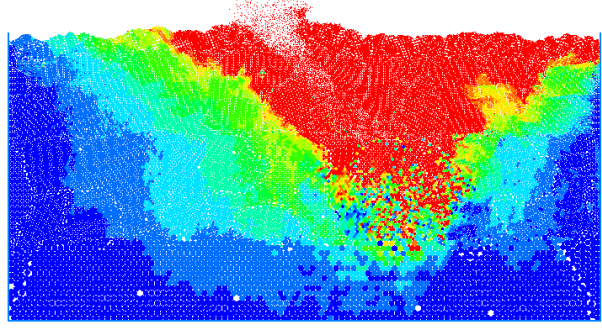


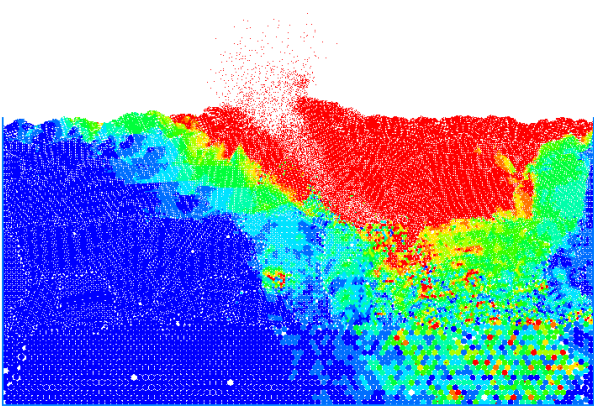
Figure 63. Velocity field variation right after impact at  $60^\circ$  and asteroid velocity of 22.5 km/s.



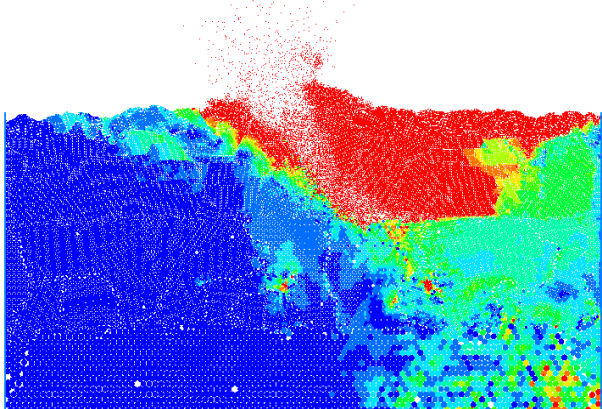
(a) 5,000 calculation cycles



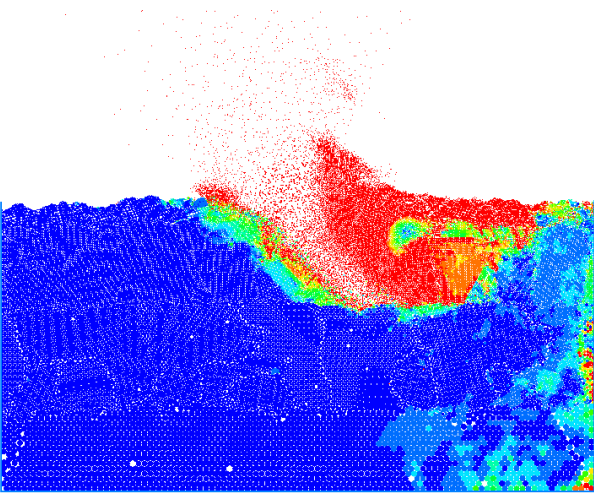
(b) 10,000 calculation cycles



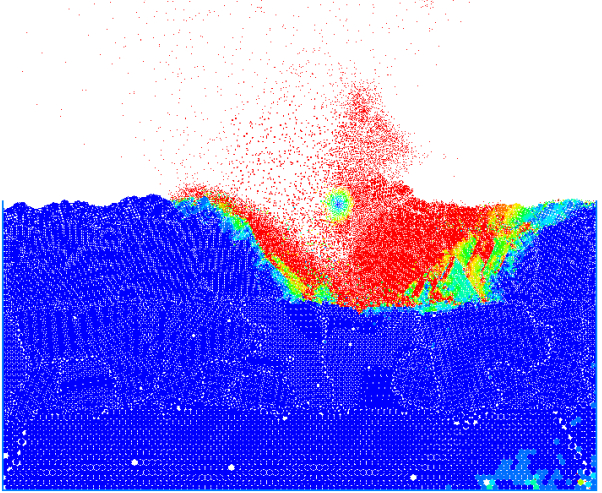
(c) 15,000 calculation cycles



(d) 20,000 calculation cycles



(e) 40,000 calculation cycles



(f) 80,000 calculation cycles

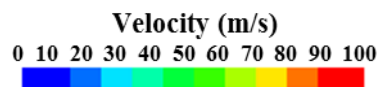


Figure 64. Velocity field variation right after impact at  $45^\circ$  and asteroid velocity of 22.5 km/s.

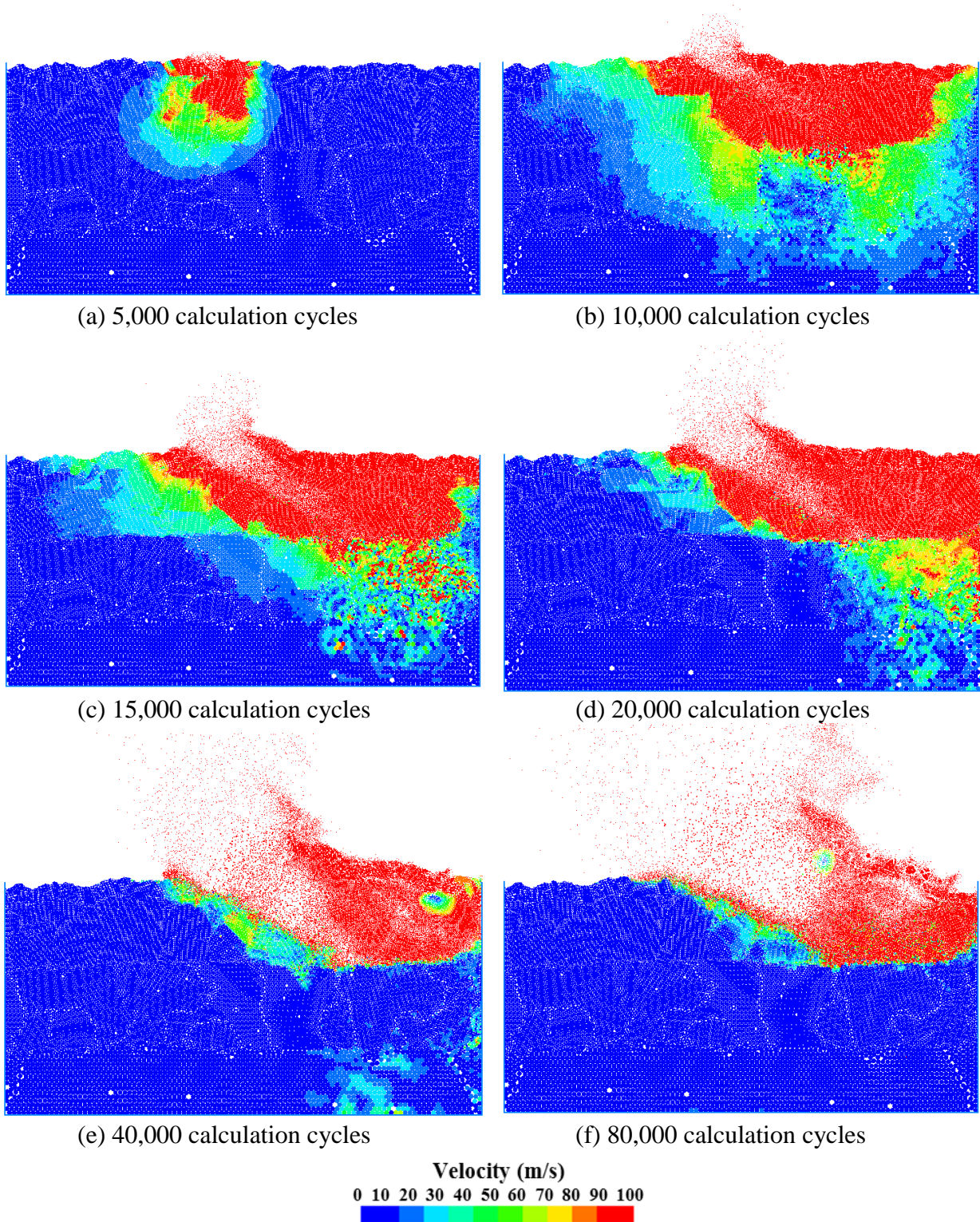


Figure 65. Velocity field variation right after impact at  $30^\circ$  and asteroid velocity of 22.5 km/s.

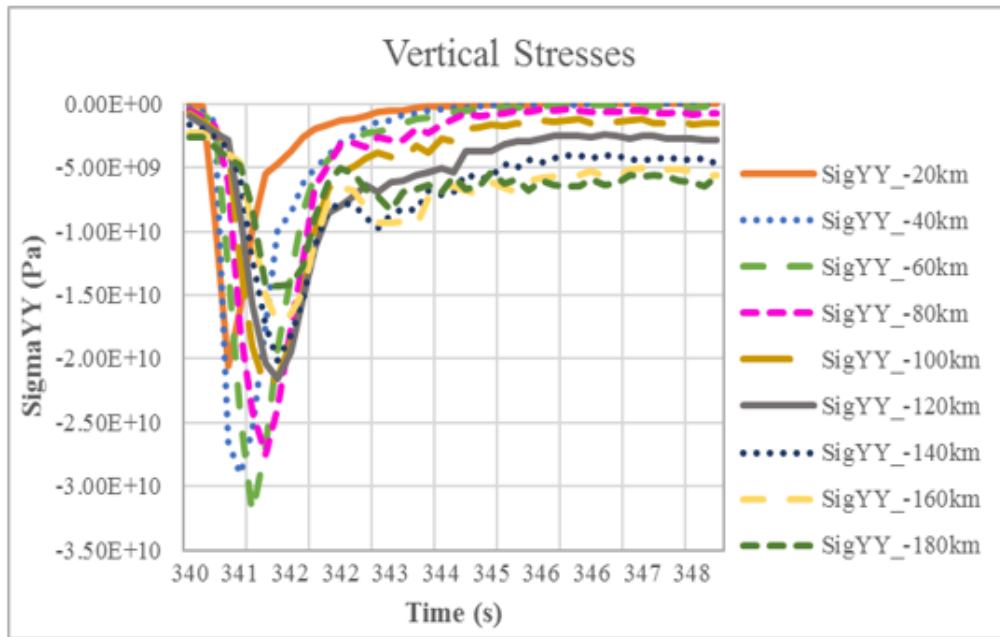


Figure 66. Vertical stress histories for asteroid impact of 15 km/s at 90°.

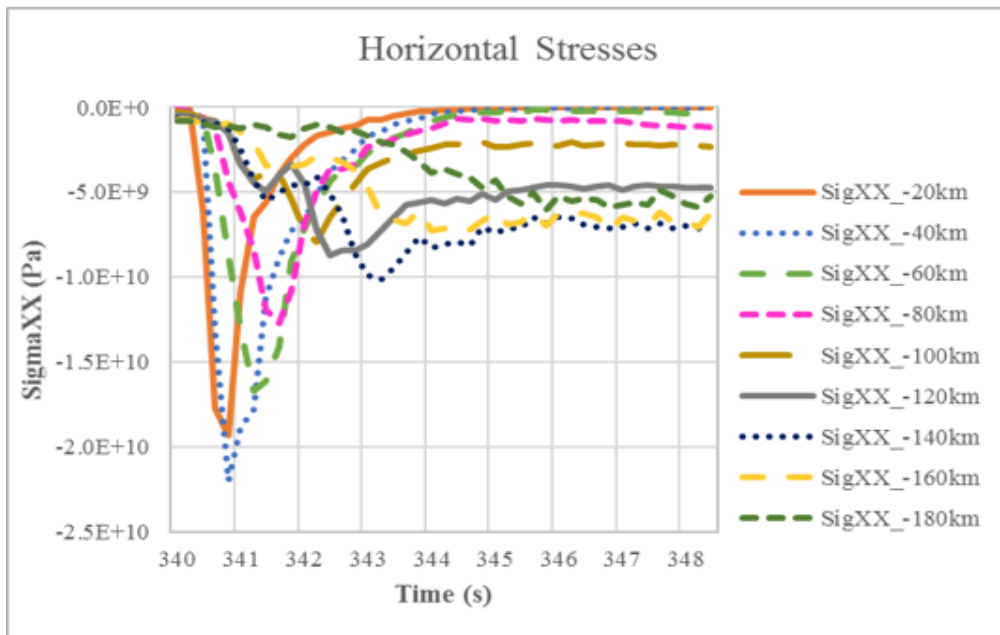


Figure 67. Horizontal stress histories for asteroid impact of 15 km/s at 90°.

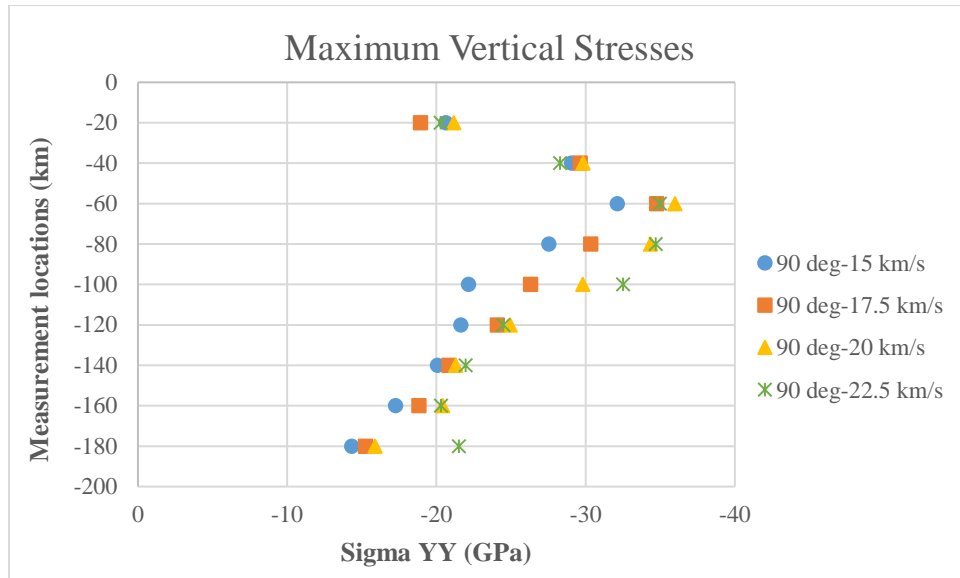


Figure 68. Maximum vertical stresses for asteroid impacts at 90°.

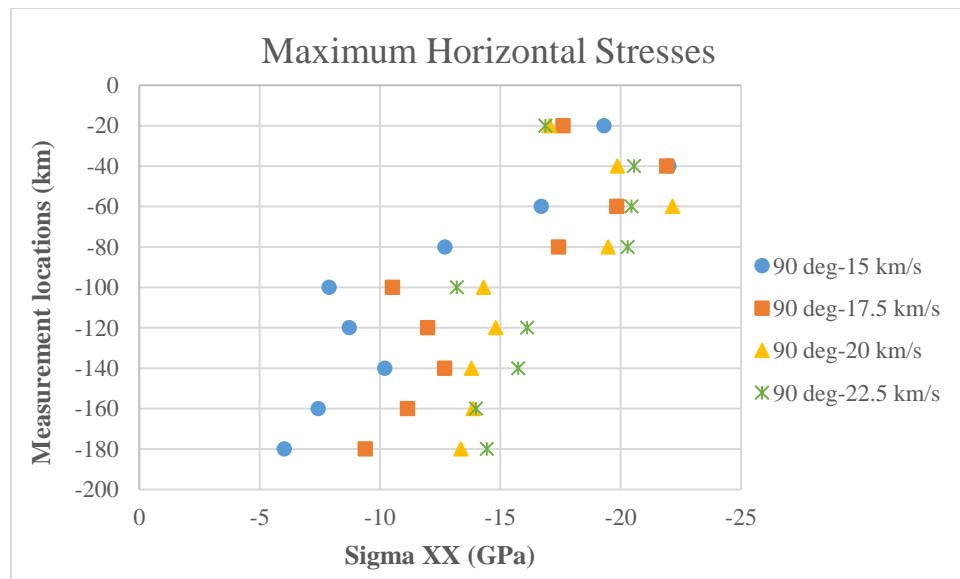


Figure 69. Maximum horizontal stresses for asteroid impacts at 90°.

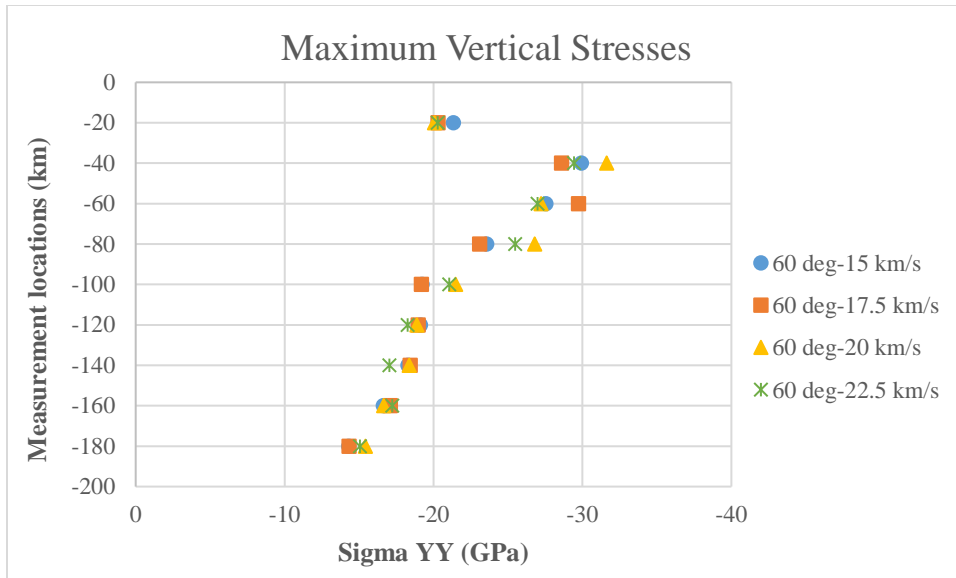


Figure 70. Maximum vertical stresses for asteroid impacts at 60°.

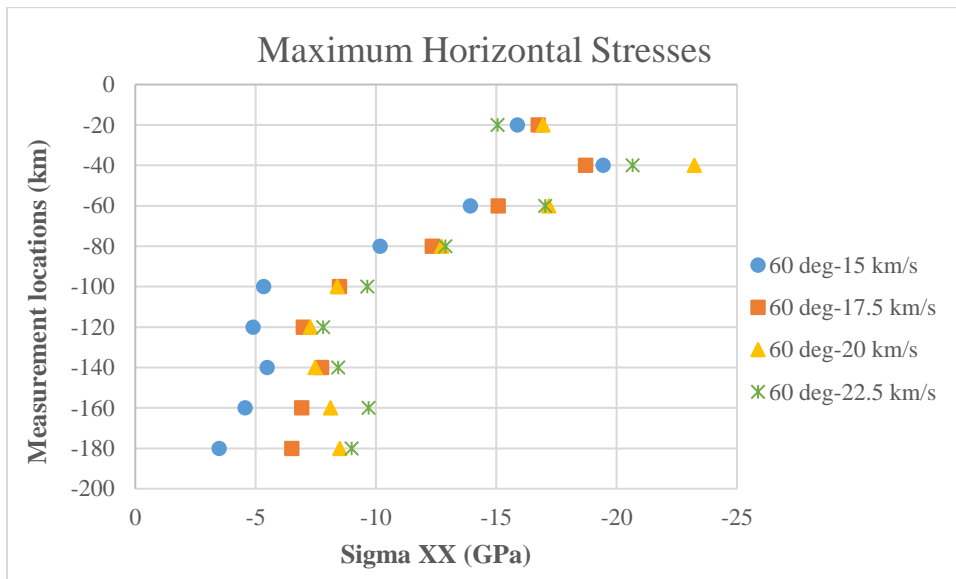


Figure 71. Maximum horizontal stresses for asteroid impacts at 60°.

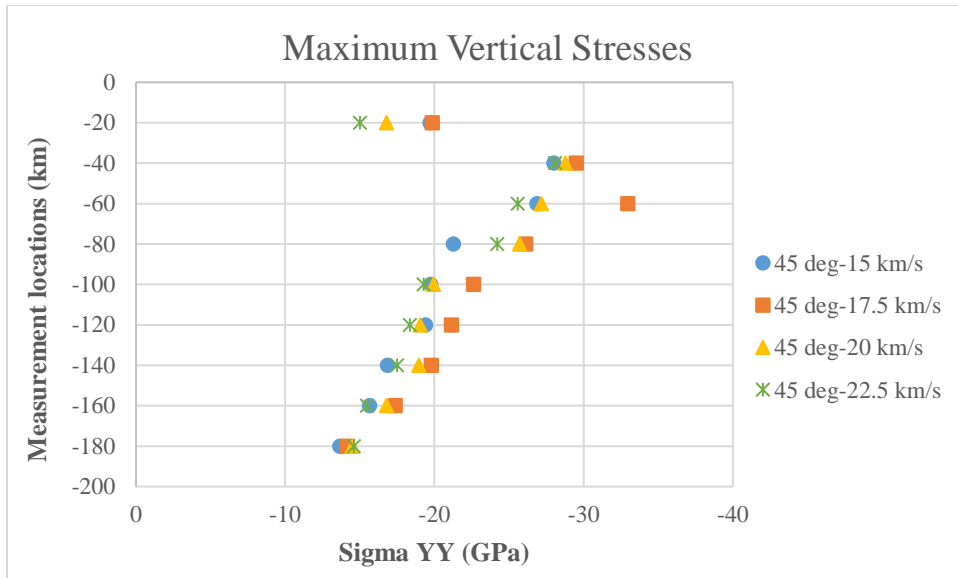


Figure 72. Maximum vertical stresses for asteroid impacts at 45°.

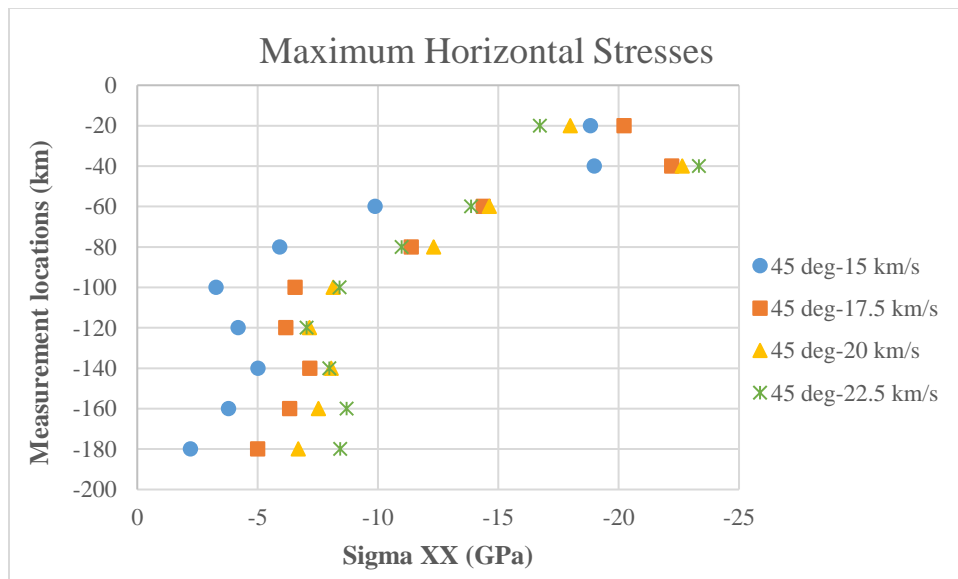


Figure 73. Maximum horizontal stresses for asteroid impacts at 45°.

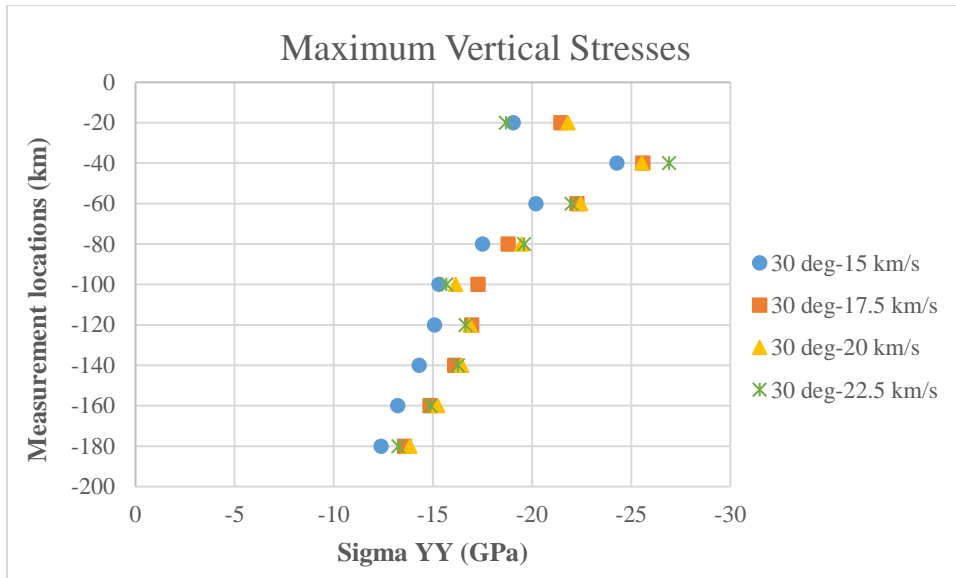


Figure 74. Maximum vertical stresses for asteroid impacts at 30°.

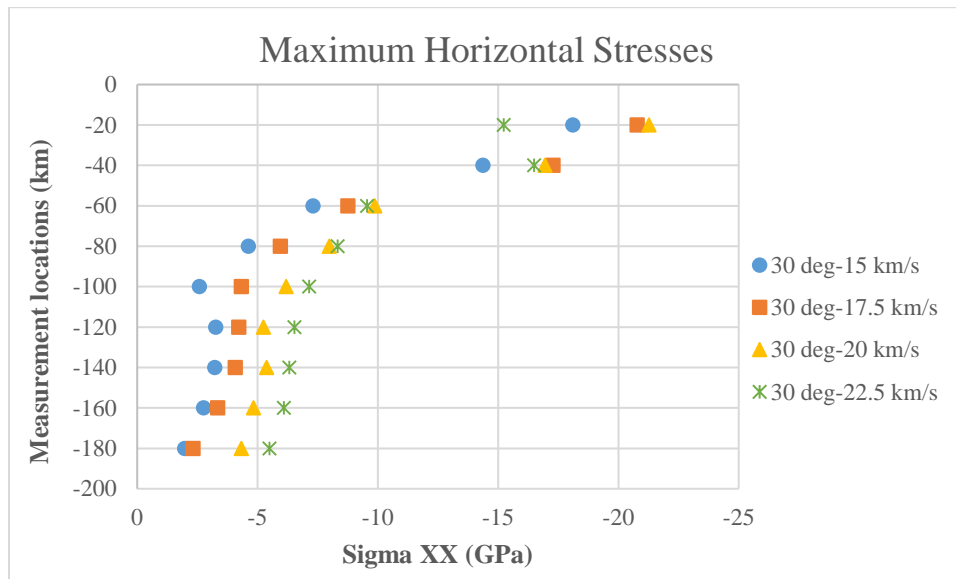


Figure 75. Maximum horizontal stresses for asteroid impacts at 30°.

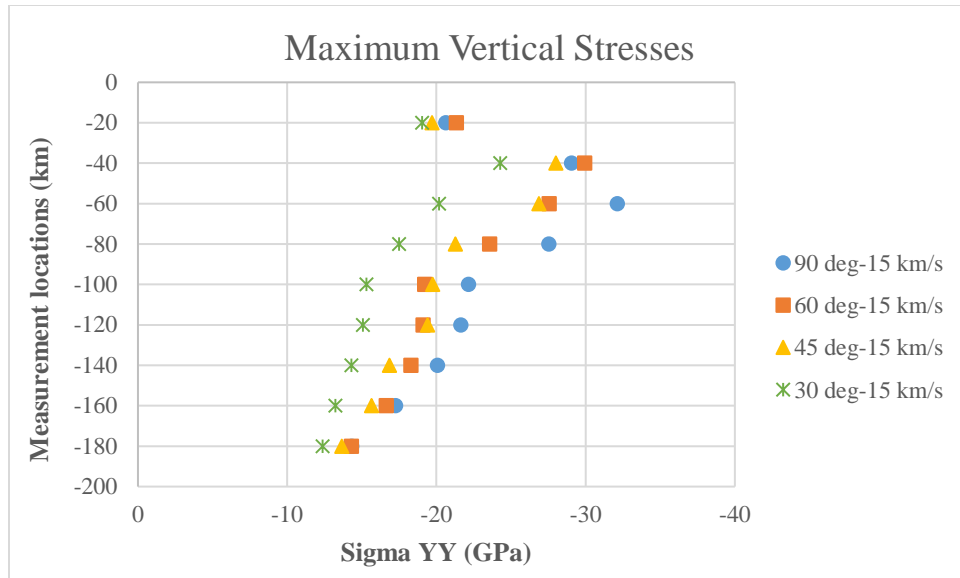


Figure 76. Maximum vertical stresses for asteroid impacts at velocity of 15 km/s.

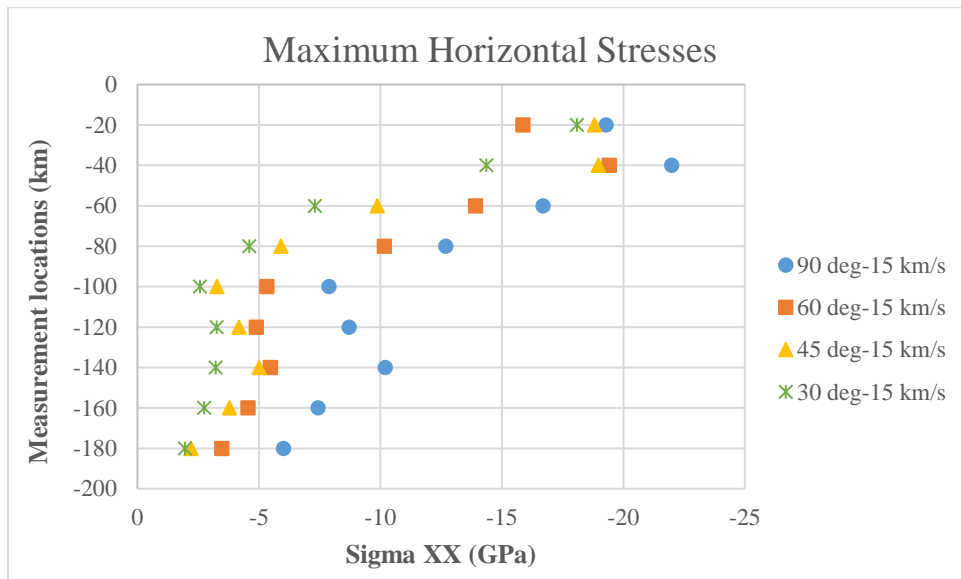


Figure 77. Maximum horizontal stresses for asteroid impacts at velocity of 15 km/s.

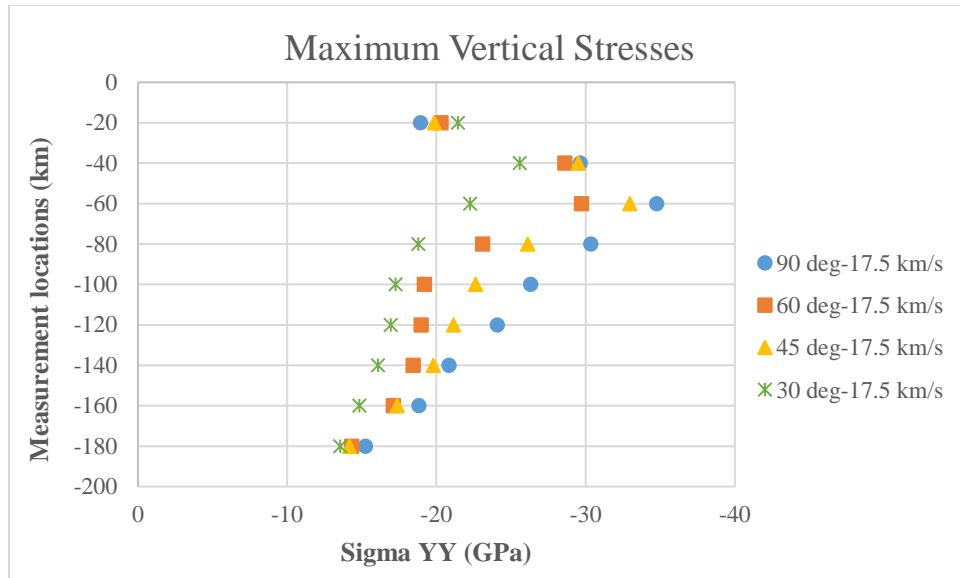


Figure 78. Maximum vertical stresses for asteroid impacts at velocity of 17.5 km/s.

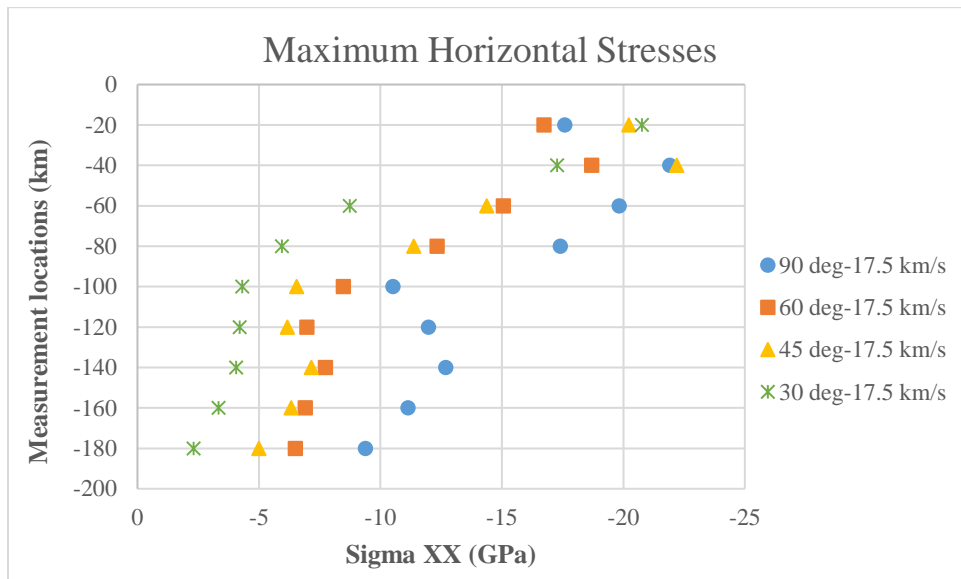


Figure 79. Maximum horizontal stresses for asteroid impacts at velocity of 17.5 km/s.

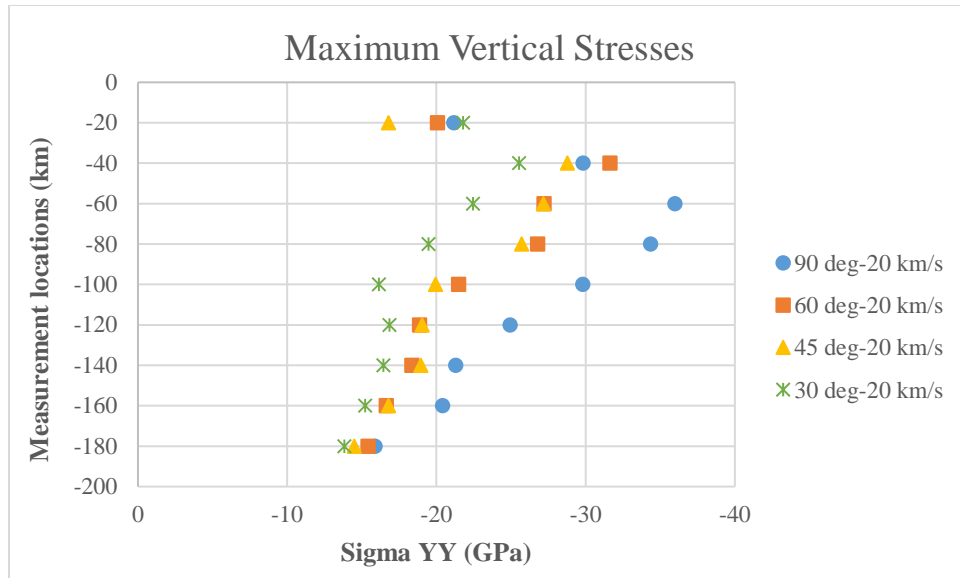


Figure 80. Maximum vertical stresses for asteroid impacts at velocity of 20 km/s.

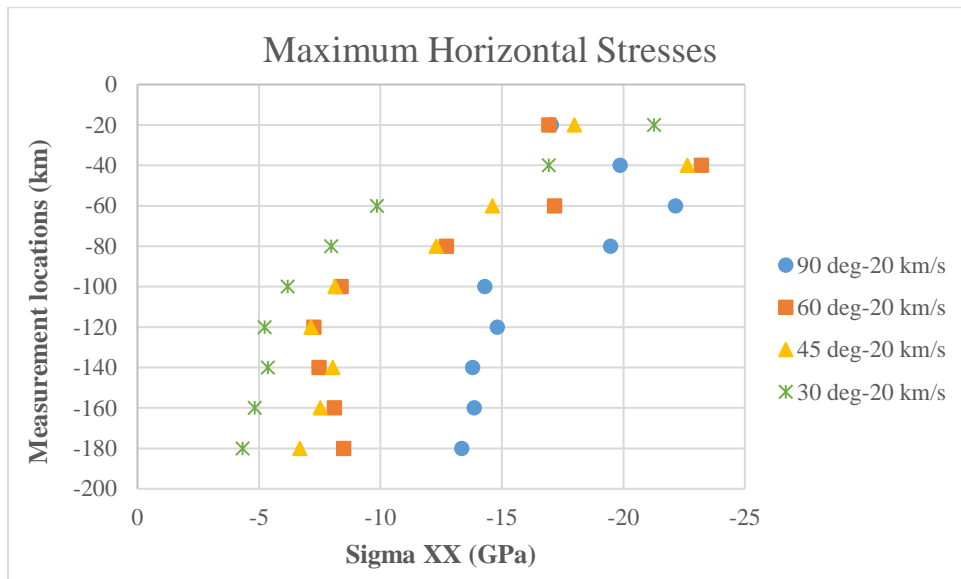


Figure 81. Maximum horizontal stresses for asteroid impacts at velocity of 20 km/s.

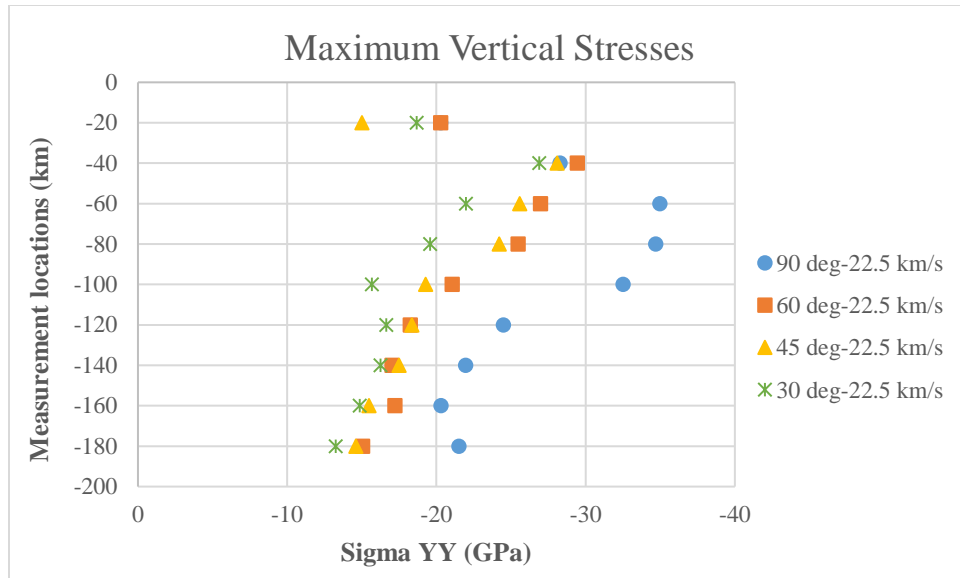


Figure 82. Maximum vertical stresses for asteroid impacts at velocity of 22.5 km/s.

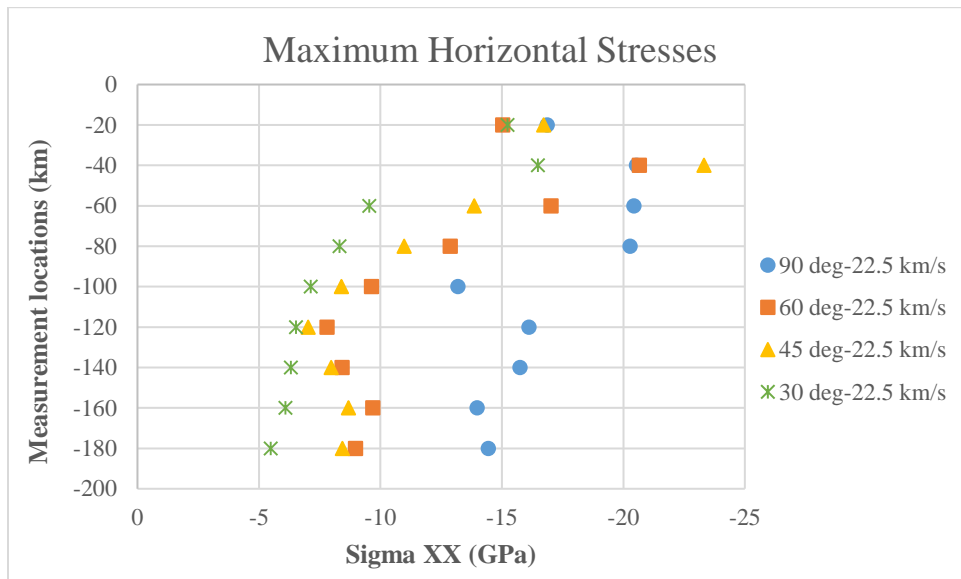


Figure 83. Maximum horizontal stresses for asteroid impacts at velocity of 22.5 km/s.

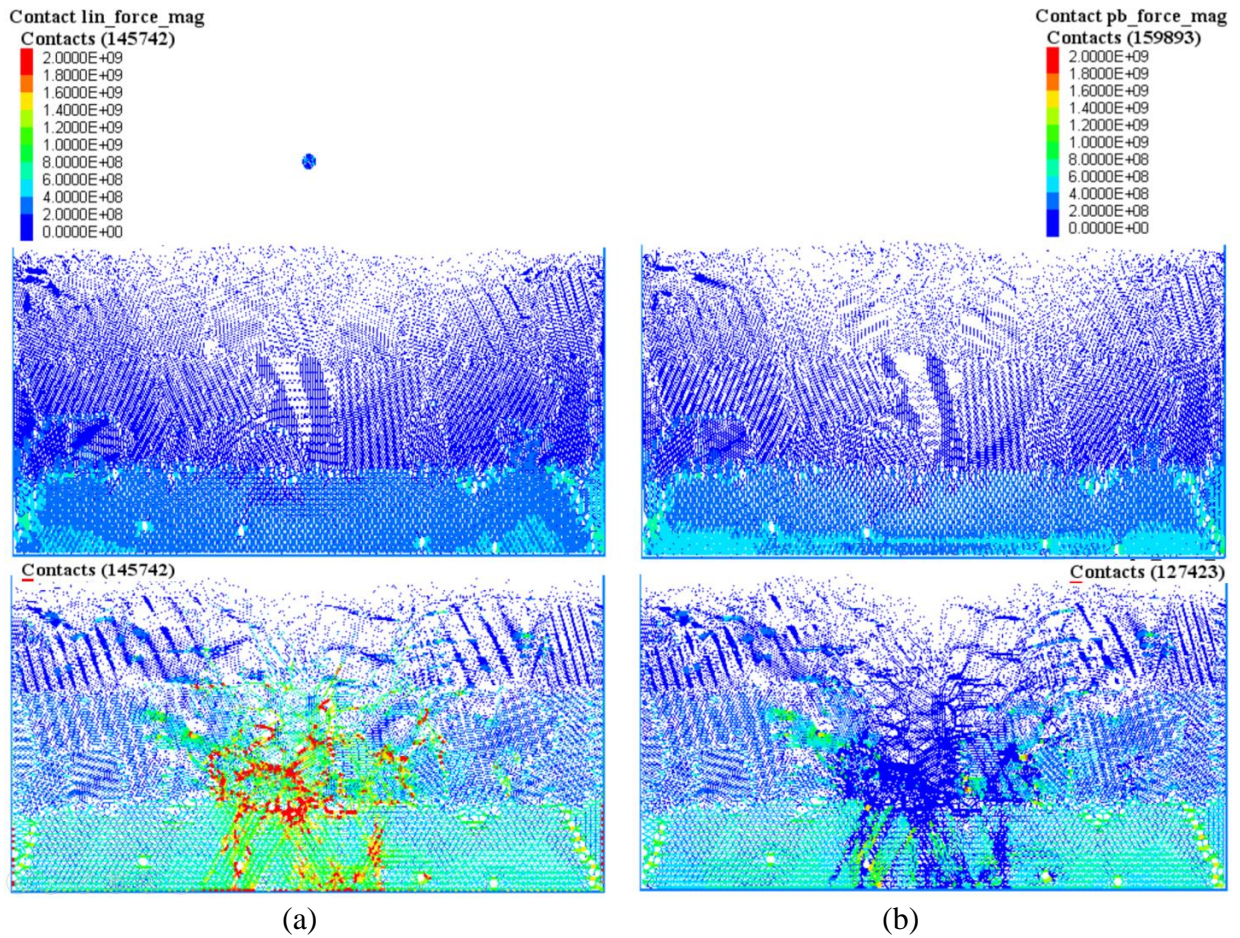


Figure 84. Maps of contact force chains (linear contacts (a) and linear parallel bond contacts (b)) before and after asteroid impact of 15 km/s at  $90^\circ$ .

## CHAPTER VI

### CONCLUSIONS AND FUTURE WORKS

#### 6.1 Conclusions

The preliminary results obtained from the four studies show the promising trend. The plots of void ratio variation of samples prepared by air pluviation and radius expansion methods are compared with the global experimental void ratio. The DEM model replicating the air pluviation method yields more accurate void ratio. In the second study, a 2D DEM model of triaxial test with flexible membrane is created capturing the slope and peak stress behavior of the material. However, the model has greater softening effect comparing to the experimental result due to the difference between 2D model and 3D experimental result. It is noticed that there are significant fluctuation in the model stress-strain curve due to the crystalline effect of using mono size particles in the model. The material elastic modulus needs to be reduced significantly to  $1e8$  Pa in order to match with the experimental response. The local deformation and formation of shear band can be observed in the model. The calibration of model micro parameters using probabilistic framework is established in the third study to replicate the behavior of sand under triaxial compression. Initial sensitivity analysis confirms that the 2D model response can capture the sample modulus of elasticity and the peak stress. Softening effect is still experienced in the model behavior. The fourth study produces a numerical assessment for the effects of asteroid impact at various impact conditions (impact angle and impact velocity). The resulted craters have complex craters aspects similarly to the Chicxulub crater. The topographies of simulated craters are then compared with the actual crater topography obtained from site investigation and show similar trend for simulations of  $90^0$  impact angle. Velocity fields are presented at the moments right after the impact blast to

capture the transmission in impact shockwave through the bedrock. Horizontal and vertical stresses are also recorded throughout the impact duration along the vertical centerline of the simulated field. It is observed that the greatest stresses experienced at the depth of 40 km below the surface level. The magnitude of the maximum stresses is within 30 GPa which seems reasonable when comparing with other previous numerical simulations since the simulations only represent mechanical response to the impact. The distribution of the impact bedrock debris is more visible on the same side with the asteroid location (uprange direction). This finding contradicts with the previous numerical study by G. Collins and needs to be further investigated.

## 6.2 Future works

There are several steps to be done to further improve the study results. Firstly, the development of 3D triaxial DEM model with flexible boundary condition will provide more accurate response for both second and third studies. Then, the optimization process of the numerical model is performed to capture the likelihood and distribution of the selected parameters and followed the probabilistic process using the result from sensitivity analysis. For the asteroid impact study, 3D model is considered to investigate on the impact debris distribution for better understanding on the coming direction of the asteroid. Thermal and hydro couplings with the original model shall be developed to provide better assessment of the impact influence. The result from this study offers an alternative solution to model large impact problems besides the traditional hydrocode program.

## REFERENCES

- [1] Hill JM and Selvadurai APS. Mathematics and Mechanics of Granular Materials. *Journal of Engineering Mathematics* 2005; 52: 1-9.
- [2] Cundall PA, and Strack ODL. A Discrete Numerical Model for Granular Assemblies. *Geotechnique* 1979; 29: 47-65.
- [3] Zhu HP, Zhou ZY, Yang RY, and Yu AB. Discrete Particle Simulation of Particulate Systems: Theoretical Developments. *Chemical Engineering Science* 2007; 62(13): 3378-3396.
- [4] Zhu HP, Zhou ZY, Yang RY, and Yu AB. Discrete Particle Simulation of Particulate Systems: A Review of Major Applications and Findings. *Chemical Engineering Science* 2008; 63(23): 5728-5770.
- [5] C O'Sullivan. Particle-Based Discrete Element Modeling: Geomechanics Perspective. *International Journal of Geomechanics* 2011; 11(6): 449-464.
- [6] Arthur JRF, Menzies BK (1972) Inherent Anisotropy in A Sand. *Geotechnique* 22:115-128
- [7] ASTM Standard D4767 (2011) Standard Test Method for Consolidated Undrained Triaxial Compression Test for Cohesive Soil. ASTM International, West Conshohocken, PA.
- [8] Brown D (2013) Tracker-video analysis and modeling tool. Open Source Physics. <http://www.cabrillo.edu/~dbrown/tracker/>. Accessed 10 Oct 2015.
- [9] Cundall PA, Strack ODL (1979) A Discrete Numerical Model for Granular Assemblies. *Geotechnique* 29:47-65
- [10] Duong T (2015). Experimental and Numerical Assessment of Sample Heterogeneity on Triaxial Failure Mechanism Using Chrome Steel Spherical Particles. M.S. Thesis, Texas A&M University.
- [11] Ladd RS (1974) Specimen Preparation Method and Liquefaction of Sands. *J Geotech Eng Div* 100:1180-1184
- [12] Morgenstern, NR (2013) Performance in Geotechnical Practice. *HKIE Transactions* 7:2-15
- [13] Mulilis JP, Seed HB, Chan CK, Mitchell JK, Arulanandan K (1977) Effects of Sample Preparation on Sand Liquefaction. *J Geotech Eng Div* 103:91-108
- [14] Nakai T (1997) Dilatancy Characteristics of Geomaterials. In: *Proceedings of deformation and progressive failure in geomechanics (IS-Nagoya)*. Japan, pp. 889-906
- [15] National Instruments (2012) LabView. <http://www.ni.com/labview>. Accessed 13 Aug 2012.

- [16] Nemat-Nasser S (1980). One Bbehaviour of Granular Soils in Simple Shear. *Soils and Foundations* 20:59-73
- [17] Noble PA (2012) Uncertainty Quantification of the Homogeneity of Granular Materials through Discrete Element Modeling and X-rays Computed Tomography. M.S. Thesis, Texas A&M University
- [18] Oda M (1972) Initial Fabrics and their Relations to Mechanical Properties of Granular Material. *Soils and Foundations* 12:17-35
- [19] Potyondy D (2015) Material-Modeling Support in PFC. Technical Memorandum ICG7766-L. Itasca Consulting Group. Minneapolis, MN
- [20] Pradhan TBS, Tatsuoka F, Sato Y (1989) Experimental Stress Dilatancy Relations of Sand Subjected to Cyclic Loading. *Soils and Foundations* 29:45-64
- [21] Precision Ball Product Catalog, Thomson, 2010. Available: [http://www.thomsonprecisionball.com/images/pdfs/PrecisionBalls-9-26-08\\_loRes.pdf](http://www.thomsonprecisionball.com/images/pdfs/PrecisionBalls-9-26-08_loRes.pdf)
- [22] Sadrekarimi A, Olson SM (2012) Effect of Sample-Preparation Method on Critical-State Behavior of Sands. *Geotech Test J* 35: 1-15. doi: 10.1520/GTJ104317
- [23] Sullivan CO (2009) Micromechanics of Granular Materials Response During Load Reversal: Combined DEM and Experimental Study. *Power Technol* 193:289-302
- [24] Thomson PR, Wong RCK (2008) Specimen Nonuniformities in Water-Pluviated and Moist-Tamped Sands Under Undrained Triaxial Compression and Extension. *Can Geotech J* 45:939-956
- [25] Viad YP, Sivathayalan S, Stedman D (1999) Influence of Specimen-Reconstituting Method on The Undrained Response of Sand. *Geotech Test J* 22:187-195
- [26] Wan RG, Gou PJ (2001) Effect of Microstructure on Undrained Behavior of Sands. *Can Geotech J* 38: 16-28. doi: 10.1139/cgj-38-1-16
- [27] Yammamuro JA, Wood FM, Lade PV (2008) Effect of Depositional Method on The Microstructure of Silty Sand. *Can Geotech J* 45:1538-1555
- [28] M.J. Jiang, S. Leroueil, J.M. Konrad, Insight into Shear Strength Functions of Unsaturated Granulates by DEM Analyses. *Computers and Geotechnics*. Volume 31, Issue 6, 2004, Pages 473-489, ISSN 0266-352X, <https://doi.org/10.1016/j.compgeo.2004.07.001>
- [29] Evans, T. Matthew (2005). Microscale Physical and Numerical Investigations of Shear Banding in Granular Soils. PhD Dissertation. Georgia Institute of Technology, Atlanta GA
- [30] Evans T, Frost J. (2008). Membrane Effects on Microstructure Evolution in 2D DEM Experiments. *GeoCongress.*; 958-965. [https://doi.org/ 10.1061/40972\(311\)120](https://doi.org/10.1061/40972(311)120)

- [31] Cho et al., N. Cho, C.D. Martin, D.C. Segol, (2007). A Clumped Particle Model for Rock. *International Journal of Rock Mechanics and Mining Sciences*, 44(7) pp. 997-1010
- [32] Li, Xia and Yu, Hai-Sui (2009) Influence of Loading Direction on The Behavior of Anisotropic Granular Materials, *International Journal of Engineering Science*, Volume 47, Issues 11–12, Pages 1284-1296, ISSN 0020-7225, <https://doi.org/10.1016/j.ijengsci.2009.03.001>
- [33] Kuhn MR. A Flexible Boundary for Three-Dimensional DEM Particle Assemblies. *Eng Comput.* 1995;12(2):175- 183. <https://doi.org/10.1108/02644409510799541>
- [34] Cui L, O'Sullivan C, O'Neill S. An Analysis of The Triaxial Apparatus Using a Mixed Boundary Three-Dimensional Discrete Element Model. *Geotechnique.* 2007;57(10):831-844. <https://doi.org/10.1680/geot.2007.57.10.831>
- [35] Cheung, G. and O'Sullivan, C. (2008). Effective Simulation of Flexible Lateral Boundaries in Two and Three Dimensional DEM Simulations. *Particuology*, Vol: 6, Pages: 483 – 500.
- [36] Wang Y, Tonon F. (2009) Modeling Triaxial Test on Intact Rock Using Discrete Element Method with Membrane Boundary. *J Eng Mech.*;135(9):1029-1037. <https://doi.org/10.1061/ASCEEM.1943-7889.0000017>
- [37] de Bono J, McDowell G, Wanatowski D. (2012) Discrete Element Modelling of a Flexible Membrane for Triaxial Testing of Granular Material at High Pressures. *Geotechnique Lett.* 2(4):199-203. <https://doi.org/10.1680/geolett.12.00040>
- [38] de Bono JP, McDowell GR. (2014) Discrete Element Modelling of One-Dimensional Compression of Cemented Sand. *Granul Matter.*16(1):79-90. <https://doi.org/10.1007/s10035-013-0466-0>
- [39] Omar T, Sadrekarimi A. Specimen Size Effects on Behavior of Loose Sand In Triaxial Compression Tests. *Can Geotech J.* 2015;52(6):732-746. <https://doi.org/10.1139/cgj-2014-0234>
- [40] Itasca. PFC3D 5.0 Manual. *Particles Flow Code in Three Dimensions-PFC3D.* 2014. Available: <http://www.itascacg.com/pfc3d>
- [41] F. da Cruz, S. Emam, M. Prochnow, J.N.Roux, F. Chevoir. Rheophysics of Dense Granular Materials: Discrete Simulation of Plane Shear Flows. *Phys. Rev. E*, 72 (2005), p. 021309
- [42] Pöschel, T., Salueña, C., Schwager, T., 2001. Scaling Properties of Granular Materials. *Phys. Rev. E* 64, 1–4. doi:10.1103/PhysRevE.64.011308
- [43] Feng, Y., Han, K., Owen, D., Loughran, J., 2007. Upscaling of Discrete Element Models for Particle Systems. In: *Proceedings of the 4 Th Int. Conf. on Discrete Element Methods.* pp. 27–29.

- [44] Thakur, S.C., Ooi, J.Y., and Ahmadian, H. (2015). Scaling of Discrete Element Model Parameters for Cohesionless and Cohesive Solid. *Powder Technology*.
- [45] Bernhardt, ML, Biscontin, G., O’Sullivan, C. (2016). Experimental Validation Study of 3D Direct Simple Shear DEM Simulations. *Soils and Foundations* 56(3) J, Pages 336–347
- [46] Kuhn MR. A Flexible Boundary for Three-Dimensional DEM Particle Assemblies. *Eng Comput.* 1995;12(2):175- 183. <https://doi.org/10.1108/02644409510799541>
- [47] Wang YH, Leung SC. A Particulate-Scale Investigation of Cemented Sand Behavior. *Can Geotech J.* 2008;45(1):29- 44. <https://doi.org/10.1139/T07-070>
- [48] de Bono J, McDowell G, Wanatowski D. Discrete element modelling of a flexible membrane for triaxial testing of granular material at high pressures. *Geotechnique Lett.* 2012;2(4):199- 203. <https://doi.org/10.1680/geolett.12.00040>.
- [49] M. J. Jiang, H. S. Yu and D. Harris, "Discrete element modelling of deep penetration in granular soils," *International Journal for Numerical and Analytical Methods in Geomechanics*, 2006.
- [50] H. Kinloch and C. O’Sullivan, "A micro-mechanical study of the influence of penetrometer geometry on failure mechanisms in granular soils," 2007.
- [51] R. D. a. B. Cambou, "Discrete Numerical Modelling of Rockfill Dams.," *International Journal for Numerical and Analytical Methods in Geomechanics*, vol. 30, pp. 1075-1096, 2006.
- [52] J. Butlanska, M. Arroyo, A. Gens and C. O’Sullivan, "Multi-scale analysis of cone penetration test (CPT) in a virtual calibration chamber," *Canadian Geotechnical Journal*, 2014.
- [53] D. L. P. M. M. M. Jamiolkowski, "Evaluation of Relative Density and Shear Strength of Sands from CPT and DMT" *Geotechnical Special Publication*, pp. 201-238, 2003.
- [54] O. Falagush, G. R. McDowell, H. S. Yu and J. P. de Bono. (2015). Discrete Element Modelling and Cavity Expansion Analysis of Cone Penetration Testing. *Granular Matter*.
- [55] Medina-Cetina Z, and Khoa HDV, Probabilistic Calibration of Discrete Particle Models for Geomaterials. ISSMFE conference, Egypt. 2009.
- [56] Zhang Yanbei. Probabilistic Calibration of a Discrete Particle Model. [M.S. Thesis]. College Station (TX): Texas A&M University; 2010.
- [57] Medina-Cetina Z. Probabilistic Calibration of Soil Constitutive Models. [Ph.D. Dissertation]. Baltimore (MD): The Johns Hopkins University; 2007.

- [58] Ahmed, S.N.U. A Study of the Influence of Confining Pressure on the Behavior of Sands. [M.S. Thesis]. Montreal (PQ): McGill University, 1972.
- [59] Itasca. PFC3D 5.0 Manual. Particles Flow Code in three dimensions-PFC3D. 2014. Available: <http://www.itascacg.com/pfc3d>.
- [60] Evans, T. Matthew (2005). Microscale Physical and Numerical Investigations of Shear Banding in Granular Soils. PhD Dissertation. Georgia Institute of Technology, Atlanta GA.
- [61] Urrutia-Fucugauchi, Jaime and Perez-Cruz, Ligia (2016). “Chicxulub Asteroid Impact: An Extreme Event at the Cretaceous/Paleogene Boundary.” American Geophysical Union. Geophysical Monograph Series 214. Extreme Events: Observations, Modeling, and Economics.
- [62] Salguero-Hernandez, E., Urrutia-Fucugauchi, J. and Ramirez-Cruz, L. (2011). “Fracturing and Deformation in the Chicxulub Crater – Complex Trace Analysis of Instantaneous Seismic Attributes.” *Revista Mexicana de Ciencias Geologicas*. Vol. 27 (1): 175-184.
- [63] Urrutia-Fucugauchi, Jaime et. al. (2011). “The Chicxulub Multi-Ring Impact Crater, Yucatan Carbonate Platform, Gulf of Mexico.” *Geofisca International*. Vol. 50 (1): 99-127.
- [64] Urrutia Fucugauchi, J., Camargo Zanoguera, A. and Pérez Cruz, L. (2011). “Discovery and focused study of the Chicxulub impact crater.” *EOS (Trans. AGU)*, Vol. 92 (25): 209-210.
- [65] French, Bevan M. *Traces of Catastrophe: A Handbook of Shock-metamorphic Effects in Terrestrial Meteorite Impact Structures*. Houston, TX: Lunar and Planetary Institute, 1998. Print.
- [66] Holsapple, K.A. and Schmidt, R.M. (1980). “On the Scaling of Crater Dimensions: 1. Explosive Processes.” *Journal of Geophysical Research*. Vol. 85 (B12): 7247-7256.
- [67] Holsapple, K.A. and Schmidt, R.M. (1982). “On the Scaling of Crater Dimensions: 2. Impact Processes.” *Journal of Geophysical Research*. Vol. 87 (B3): 1849-1870.
- [68] Austin, Michael G. et. al. (1981). “Z-Model Analysis of Impact Cratering: An Overview.” *Multi-ring Basins: Formation and Evolution. Proceedings of the Lunar and Planetary Science Conference, Houston, TX, November 10-12, 1980.*
- [69] Takata, T. and Ahren (1994). *Numerical Simulation of Impact Cratering at Chicxulub and the Possible Causes of KT Catastrophe*. Lunar and Planetary Institute. 1994, p.125. 1994LPICo.825..125T
- [70] Ivanov, B.A., Badukov, D.D., Yakovlev, O.I., et al., *Degassing of Sedimentary Rocks Due to Chicxulub Impact: Hydrocode and Physical Simulations*, *Geol. Soc. Spec. Pap.*, 1996, vol. 307, pp. 125–139.

- [71] Pierazzo, E., and Melosh, H.J., 1999, Hydrocode modeling of Chicxulub as an oblique impact event: *Earth and Planetary Science Letters*, v. 165, p. 163–176.
- [72] Collins, Gareth S., Melosh, H. Jay, and Marcus, Robert A. (2005). “Earth Impact Effect Program: A Web-based computer program for calculating the regional environmental consequences of a meteoroid impact on Earth.” *Meteoritics & Planetary Science*. Vol. 40 (6): 817-840.
- [73] Ivanov, B.A., Large Impact Crater Modeling: Chicxulub, Third International Conference on Large Meteorite Impacts, Nordlingen, Germany, 2003, Houston: Lunar Planet. Inst., 2003
- [74] Collins GS, et al. (2008). Dynamic modeling suggests terrace zone asymmetry in the Chicxulub crater is caused by target heterogeneity. *EPSL*, 270: 221–230.
- [75] Collins, G. S., Wünnemann, K. Artemieva, N. and Pierazzo, E. (2012). Numerical Modelling of Impact Processes. In *Impact Cratering* (eds G. R. Osinski and E. Pierazzo). doi:10.1002/9781118447307.ch17
- [76] Collins GS, et al (2017). Numerical Simulations of Chicxulub Crater Formation by Oblique Impact. Lunar and Planetary Science Conference, Houston, TX.
- [77] Amsden AA & Ruppel HM (1981). SALE-3D: a simplified SALE computer program for calculating three-dimensional fluid flow. LANL Report LA8905. Los Alamos, New Mexico, 151 p.
- [78] Gisler, Galen et. al. (2003). “Two- and Three-Dimensional Simulations of Asteroid Ocean Impacts.” *Science of Tsunami Hazard*. Vol. 21(2): 119-134.
- [79] Elbeshausen D, et al. (2009). Scaling of oblique impacts in frictional targets: implications for crater size and formation mechanisms. *Icarus*, 204:716–731.
- [80] Itasca. PFC3D 5.0 Manual. Particles Flow Code in three dimensions-PFC3D. 2014. Available: <http://www.itascacg.com/pfc3d>.
- [81] Morgan JV, et al. (2016). The formation of peak rings in large impact craters. *Science*, 354(6314): 878-882.
- [82] Potyondy D (2015) Material-modeling support in PFC. Technical Memorandum ICG7766-L. Itasca Consulting Group. Minneapolis, MN
- [83] Ledgerwood, L. W. (2007). “PFC Modeling of Rock Cutting Under High Pressure Conditions.” American Rock Mechanics Association.